Modeling of Cross Correlation Flow Measurement Systems

Alexander Gurevich

Faculty of Technology
De Montfort University

A dissertation submitted in partial fulfilment for the degree of
Doctor of Philosophy at De Montfort University

July 2013

Abstract

In the work presented in this thesis, an original mathematical model of cross correlation flow measurement was developed, based on rigorous analysis of space-time development of a velocity field and vorticity field in turbulent flow. This model describes the effect of flow conditions on ultrasonic cross correlation flow meter output. Laboratory testing was conducted to validate the model. Results of numerical simulations based on the model were in good agreement with laboratory test results. Maximum deviation between results predicted by the model and experimental results was 3.2%, and average deviation was 1.1%. This model provides a basis for uncertainty analysis of cross correlation flow measurement, and its traceability to accepted industry standards, by describing the effect of various flow parameters and meter design parameters on flow measurement. Some of the results of this work are being used in industry today.

Acknowledgements

The research project presented in this paper was conducted with support from many people. Especially, the author expresses his gratitude to Professors Mikhail Goman and Ibrahim Abdalla from De Montfort University, Professor Steven Tullis from McMaster University, Canada, and Dr. Armando Lopez and the scientists, engineers, and technicians from Advanced Measurement and Analysis Group Inc., Canada.

Contents

List of Figures

Introduction

Flow measurement technology is one of the first forms of instrumentation used in human history. In ancient Egypt, flow measurement instrumentation was used for agriculture. In ancient Rome, flow measurement instrumentation was used for city water supply systems. Today, 15-30% of all measurement instrumentation used in industry in the world is flow measurement instrumentation. A dramatic increase in applications for flow measurement devices started during the industrial revolution. Despite this, the types of flow measurement technologies used in industry has been very limited until recent decades. Mainly, these flow measurement technologies have been *pressure differential* flow meters, *orifice plate* flow meters, and *turbine* flow meters. As a result of the increased rate of technological advances after the Second World War, many new types of flow measurement technologies have been developed. Today, pressure differential flow meter are probably still the most common flow meters in use, although new technologies, such as ultrasonic flow meters, Coriolis flow meters, electromagnetic flow meters, and turbine flow meters, also have a significant presence in industry [1].

Industry requirements for accuracy, and traceability of flow measurements to accepted standards, is growing, and flow measurement technologies in general are behind industry standards in this regard. One example of high requirements for flow measurement accuracy, and traceability to internationally accepted standards, is *custody transfer* applications. These are situations where a fluid substance changes custody while being transferred from one owner to another, such as oil or natural gas being pumped through pipelines between countries. Consider an oil pipeline system, such as the Trans Alaska Pipeline System carrying approximately 500,000 barrels of crude oil per day,

and a typical oil price of approximately 100 USD per barrel [2]. Such a system delivers approximately 50,000,000 USD worth of oil per day. A flow measurement error of 0.1% results in a loss (or gain) of 50,000 USD per day, or 18,000,000 UDS per year.

Another example where accurate and traceable flow measurement is required, are the *power generation* and *materials processing* industries. Consider a typical nuclear power plant, with power output 1000 MW. Safe operation of a nuclear reactor is based on safety analysis conducted at a certain power level [3,4]. As a result of this analysis, a limit is placed on permitted reactor power, P. To be sure that this limit is not exceeded, the plant is operated such that reactor power does not exceed $P - \Delta P$, where ΔP is the possible error in determining reactor power. This error is mainly defined by the measurement error of reactor coolant flow. Typically, if using pressure differential flow meters, ΔP is of order 2%. If ΔP could be reduced to 0.5%, the reactor power could be increased by 1.5%. Therefore, equipping 67 reactors with improved flow measurement instrumentation, is equivalent to building a new reactor without the associated financial and ecological costs.

In these examples, the claimed flow measurement error bound must be accepted by all parties involved: the buyer and seller in the first example, and the plant operator and plant safety regulator in the second example. This mutual acceptance is achieved through the existence of internationally accepted standards for the validation of the applied flow measurement instrument, such as ISO standards, ASME codes, and others. The critical component of validating the instrument is demonstrating traceability of real measurements to a mutually accepted reference measurement.

Any measurement is a comparison of an unknown value and a known value. For example, measuring a rope's length is a comparison of the unknown length of the rope and the known length of a ruler. Traceability is the process of ensuring a fair comparison with the known value. This process involves a number of critical steps. One step, called calibration, is assurance that the ruler is traceable, through a chain of comparisons, to a national

or international standard of length, such as a rod in the International Bureau of Weights and Measures. Another step is to assure that conditions of calibration are the same as the conditions of measurement. For example, if calibration and measurement were conducted at different temperatures, an additional measurement error could result, unless thermal expansion of the ruler is taken into account. Also, the tension of the rope must be specified, because differences in the tension of the rope could result in different length measurements.

In flow measurement, traceability is difficult to accomplish, because it is difficult to ensure that the environmental conditions and flow parameters at the flow meter location are similar during field measurement and during laboratory calibration. These parameters include flow velocity distribution, turbulent spectrum, presence of air bubbles or solid particles, and others. Ensuring the similarity of all flow conditions is impossible, because a real industrial piping system can not be perfectly reproduced in a laboratory with all pumps, valves, vibrations, and changing parameters present in real industrial environments. Therefore, a subset of the flow parameters is required to remain similar to achieve traceability, and those flow parameters which must remain similar depend on the flow measurement technology used. A very thorough quantitative understanding of the physical principals affecting the flow meter must exist, in order to correctly select these flow parameters. Hence, even older flow measurement technologies, like the venturi, require a deeper level of understanding than what was acceptable in the past.

There are different types of flow measurement technologies available, based on different principles, and suitable for different applications. *Ultrasonic* flow meters have been gaining popularity in recent decades. Ultrasonic flow meters are based on non-intrusively transmitting ultrasonic beams through a pipe, and detecting the beams on the other end. Flow rate is determined by analyzing the ultrasonic signal after it is received by a detector. Some ultrasonic meters are clamp-on, meaning the ultrasonic devices are attached to the exterior of the pipe wall, and ultrasonic beams are transmitted through the pipe wall. The three more common forms of ultrasonic

flow measurement are *Transit Time*, *Doppler*, and *Cross Correlation*, where transit time flow measurement is currently the most popular of the three. Details on the operating principals of these flow measurement technologies, and others, are given in the first chapter of this thesis.

Ultrasonic Cross correlation flow measurement technology has advantages over other types of flow measurement methods. Cross correlation flow measurement is based on measuring the transport velocity of turbulent structures within the flow. Ultrasonic cross correlation flow meters are clamped onto the outside of a pipe, and measure flow by transmitting ultrasonic beams perpendicular to the pipe axis, through pipe walls and the fluid within the pipe. The transmitted beams are received by detectors on the other side of the pipe. Such flow meters are non-intrusive because they can easily be clamped onto a pipe and begin measurement without disturbing the pipe flow. Also, cross correlation flow measurement can be conducted in conditions of extreme temperatures and rapidly changing temperatures. Calculation of speed of sound is not necessary for cross correlation flow measurement, and changes in speed of sound do not affect measurement. Measured results can be obtained within seconds of activating the meter, and changes in flow are detected by the meter within seconds. Also, a single installation of a cross correlation flow meter can measure flow in both directions, which is not the case for many flow meters. Clamp-on transit time flow meters, by comparison, often operate poorly in conditions of changing temperatures, may require calculation of speed of sound, and require a time sampling rate much higher than that required by the cross correlation flow meter. As a result, clamp-on cross correlation flow meters have a significant advantage over clamp-on transit time flow meters.

The advantages of cross correlation flow measurement technology, allow for easy flow measurement for all piping application, and are especially useful in conditions where contact between the flow meter and the flow could damage the meter, or where it is hazardous to expose the fluid or the inside of the pipe to the medium outside the pipe walls. An example of such hazardous conditions is a nuclear power plant.

Since cross correlation flow measurement is based on measuring the transport velocity of turbulent structures, achieving traceability of cross correlation flow measurement requires a thorough understanding of turbulent pipe flow and turbulent flow in general. Some works have been done on this subject, but there is a significant gap between what has been done and what is needed to meet growing industry standards. The purpose of the work presented in this thesis is to close this gap.

The work presented in this thesis consisted of three main aspects:

1. The development of a new mathematical model of ultrasonic cross correlation flow measurement, based on rigorous analysis of space-time development of a velocity field and vorticity field in turbulent flow.

2. Developing a new computational flow simulation method, based on the model, to describe the behavior of the meter.

3. Conducting laboratory testing to validate the model.

Original Contributions In This Work

An original mathematical model of cross correlation flow measurement was developed, based on rigorous analysis of space-time development of a velocity field and vorticity field in turbulent flow. This model describes the effect of flow conditions on cross correlation flow meter output.

An original equation describing an angular-averaged turbulent velocity field, as a function of time and radial position at one pipe cross section, was developed. A number of free parameters in this equation allow for the generation of a turbulent velocity field with desired statistical characteristic. These characteristics include spacial and temporal turbulent scales, spacial distribution of the turbulence power spectrum, and space and time correlation of turbulent velocity.

A computer algorithm was developed to calculate integral characteristics of the turbulent velocity field along a pipe, based on the original results described above. This algorithm can be used to simulate cross correlation flow measurement for different flow conditions.

Through laboratory testing designed and conducted by the author, new experimental data was obtained on the sensitivity of cross correlation flow measurement output to spacing between ultrasonic beams, under different flow conditions.

Thesis Structure

The remainder of this thesis consists of Chapters 1-5, and a conclusion.

Chapter 1 describes the state of the art of various flow measurement technology used in industry. Since the cross correlation flow meter is based on the dynamics and transport of turbulent structures, a review of the state of the art of turbulent flow modeling is also given.

Chapter 2 consists of theoretical analysis which provides the basis of the mathematical model of cross correlation flow measurement developed in this work.

Chapter 3 describes the method of implementing the theoretical results, described in chapter 2, into a mathematical model of cross correlation flow measurement. This chapter includes an original equation describing an angular-averaged turbulent velocity field, as a function of time and radial position at one pipe cross section. It also includes a computer algorithm, developed as part of this work, to calculate integral characteristics of the turbulent velocity field along a pipe, to simulate cross correlation flow measurement for different flow conditions.

Chapter 4 describes laboratory testing conducted to validate the model. Details are given about test set-up, test conditions, and data analysis.

Chapter 5 presents a comparison, and discussion, of laboratory test results and simulated results based on the mathematical model.

A summary of the results of this work is presented in the Conclusion section, followed by a description of Future Work.

Nomenclature

Below is a list of some terms and symbols often used in this work. These terms and symbols have the following meanings, unless otherwise specified in the text.

L , *Transducer Spacing* - Distance between upstream and downstream ultrasonic beams of a cross correlation flow meter. NOTE: In section 2.1.2, L represents a length scale.

τ_m , *Time Delay* - Time taken by the turbulent picture to travel from upstream ultrasonic beam to downstream ultrasonic beam

U_m - Single measured flow velocity

V_m - Average measured flow velocity

V_a - Cross section average axial flow velocity

C , *Hydraulic factor* - Ratio between cross section average flow velocity and average measured flow velocity

Re - Reynolds Number

Φ - Demodulated signal collected by the cross correlation flow meter

v - Radial turbulent velocity

$\vec{u}$ - Flow velocity

$\vec{\omega}$, ω - Flow vorticity. NOTE: In chapter 3, ω represents frequency. In section 2.1.2, ω represents a vorticity scale.

ρ - Density

p - Pressure. NOTE: p is also used as a control parameter when defining the function $\theta_j(y)$.

ν - Kinematic viscosity

RANS - Reynolds averaged Navier Stokes

LES - Large eddy simulation

DNS - Direct numerical simulation

$\backsimeq$ Of order magnitude

$\propto$ - Proportional to

(ζ, η, τ, ξ) - Coordinate system where observer is placed in frame of reference moving at average axial flow velocity $U(x, y)$, where $\zeta = x, \eta = y, \tau = z, \xi = \frac{x}{U(x,y)} - t$. NOTE: In section 2.2, ζ, η, and ξ are used to represent Cartesian coordinates.

$\hat{v}$ - Surrogate velocity field that develops through time and space according to the locally frozen turbulent approximation

$S(x, \omega)$, S_j - Power spectrum of demodulated signal. Here, ω represents frequency.

j - Time harmonic number

m - Maximum value j can take on

ω_j - Frequency corresponding to harmonic j

k_j - Multiplier ensuring simulated demodulated signal has desired power spectrum

$C_j(y)$, $C(y)$ - Function defining radial turbulent spectrum distribution for simulation

$\theta_j(y)$ - Phase correlation function

p - In the context of $\theta_j(y)$, p is a control parameter for correlation of velocity along pipe diameter.

N_y - Number of spacial cells along pipe diameter used in simulation

q_j - Random phase shift

R - Pipe radius

D - Pipe diameter

T - Time of single cross correlation measurement

U - Cross section average axial flow velocity used in simulation

n - Indication of smallest simulated eddy size, where $\frac{D}{n}$ is this size. NOTE: n is also used to represent a parameter defining the axial flow profile.

$P(y)$ - *Time and angular averaged axial flow profile*, sometimes referred to as *average axial flow profile*, *axial flow profile*, or *flow profile*

U_max - Maximum value of axial flow profile $P(Y)$

n - In the context of axial flow profile, n is a parameter indicating flatness of the flow profile.

SPU - Signal Processing Unit

SCU - Signal Conditioning Unit

X^c - Complex conjugate of X, where X is any function

$F(x)$ - Fourier transform of x, where x is any function

$x \star y$ - Cross correlation of x and y, where x and y are any two functions

Chapter 1

State of the Art of Flow Measurement Technology

Industry requirements for accuracy and traceability of flow measurements are growing, and flow measurement technologies are generally behind industry standard in this regard. Some critical flow measurement applications, such as safety and operation of nuclear power plants, and custody transfer, require rigorous quantitative analysis of all factors that could result in deviations of instrument readings, in order to satisfy growing industry standards. This analysis must be based on the a deep understanding of the underlying physics of flow measurement methods, adequate mathematical modeling, and laboratory testing.

The subject of the research presented in this thesis, is the development and validation of an adequate mathematical model for cross correlation flow measurement technology, a technology that has been used in important applications in the nuclear power industry.

This work deals with different areas of physics and engineering. In this chapter, flow measurement methods used in industry will be discussed. Special focus will be given to ultrasonic flow measurement, and especially cross correlation flow measurement. An important factor in flow measurement is the interaction between the flow meter and the flow. For this reason, fluid

dynamics theory, and computational flow simulation methods, will also be discussed below, with special attention given to turbulence modeling. Details of the new results obtained in this research are briefly summarized in the Introduction, and are described in greater detail in later chapters.

1.1 Flow Measurement Technology

As mentioned in the introduction to this paper, different types of flow measurement technologies exist, based on different operating principles, and different flow meters are best suited for different applications. The more common flow measurement technologies can be divided into four categories: *Mechanical* flow meters, *Pressure Differential* flow meter, *Electromagnetic* flow Meters and *Ultrasonic* flow meters [5-7].

1.1.1 Mechanical Flow Meters

Mechanical flow meters are based on the measured fluid displacing a piece of machinery [5,6]. The displacement is measured, and the measurement is related to a flow rate. The most basic type of mechanical flow meter is a *weight tank*, analogous to a bucket combined with a weighing scale and a stopwatch. Flow is temporarily diverted or delayed from its regular path, by flowing into a container for a measured period of time. The container is called a weight tank. The mass of the weight tank is calculated as the flow enters. After a given period of time, typically a couple of minutes, the weight tank releases the flow back into its regular path. With the increase in the weight tank's mass known, and the time taken for that increase in mass known, the average mass flow rate can be calculated. Weight tank meters are usually not suitable for industrial applications, but are widely used as a reference instrumentation in laboratory calibrations of other flow meters, and can achieve an uncertainty of order 0.01% - 0.1%. The unique advantage of these meters is that the flow reading does not depend on flow conditions, such as velocity distribution, and is directly derived from two basic units: mass and time.

A more complex mechanical flow meter is a turbine meter. A turbine is inserted into the flow, and the rate of rotation of the turbine is measured. Knowing various mechanical properties of the turbine, the rate of rotation can be an indicator of the flow rate of the fluid. The output of these meters depends on flow velocity distribution and other flow characteristics. Also, the rotating mechanism is directly exposed to the flow, and therefore requires frequent maintenance.

Another type of mechanical meter is the Coriolis Flow Meter. This measurement method consist of the flow passing through a curved piping section, which moves in the direction perpendicular to the plane of the flow path. Usually, the curved piping section consists of a u-shaped tube oscillating with a certain frequency. The force that would be required to induce such oscillation, called the Coriolis force, is directly proportional to the mass flow rate. The most significant advantage of these meters is that the output directly depends on the mass flow, and is not effected by flow conditions.

The greatest drawbacks of mechanical flow meters, are the presence of moving parts, and contact of the sensing elements with the fluid. To achieve and maintain high accuracy, frequent maintenance is required, which is often not possible, or is very expensive in industrial applications. Power plants are an example of an application where such flow meters are rarely used, due to high flow rates that could damage moving parts. Also, flow containing solid particles can damage moving mechanical parts if solid particles gather within sensitive areas of the mechanism, analogous to a propeller being damaged in a sand storm. All of these difficulties are greatly increased with the increase in size of the flow meter, which is necessary for many industrial applications.

1.1.2 Pressure Differential Flow Meters

Another type of flow measurement technology is *pressure differential* flow measurement [5,6]. This technology is based on measuring the fluid pressure at two nearby locations within a flow. The flow rate is derived from the pressure differential, using the Bernoulli Equation. *Venturi* flow meters and

orifice-plate flow meters are common pressure differential flow meters used in power production and material processing industries, where flow rates reach as high as hundreds liters per second. The Venturi flow meter consists of a section of pipe with decreasing diameter, inserted into the piping configuration where flow measurement is desired. Pressure is measured at the wider section of the inserted section of pipe, and the narrower section of the inserted section of pipe. The difference in pressure is translated into flow rate. The orifice-plate is a section of pipe consisting of a plate with an opening in it, inserted into a piping configuration where flow measurement is desired. Flow must then travel through the opening in the plate to continue through the piping configuration. Pressure is measured at a location upstream of the opening in the plate, and immediately downstream of the opening in the plate, similarly to a venturi. Just as with the venturi meter, the difference in pressure is translated into flow rate. Figure 1.1 shows the concepts of a venturi flow meter and an orifice place flow meter [8].

In order to obtain the flow rate from a known pressure difference, a coefficient called the *discharge coefficient* must be known. The discharge coefficient depends on flow condition and on the specific geometry of the meter. In order to achieve flow measurements with accuracy of 2% or better, the discharge coeficient is determined in laboratory calibration for each individual instrument. In order to reduce the effect of flow condition, the measurement instrument is placed downstream of a long stright pipe run which follows a flow strightener. This entire assembly (called *flow measurement section*) must be calibrated in the laboratory, and transported and installed in the field without being disassembled. For many industrial applications, such as power plants, the length of the flow measurement section can reach ten meters or more.

Pressure differential flow meters do not have moving parts. However their sensing elements are exposed to the flow. This often results in errors in instrument readings, due to flow intensified erosion. For example, in nuclear power plants, where pressure differential meters are commonly used, *venturi fouling* and *orifice plate degradation* are well known examples of biased flow

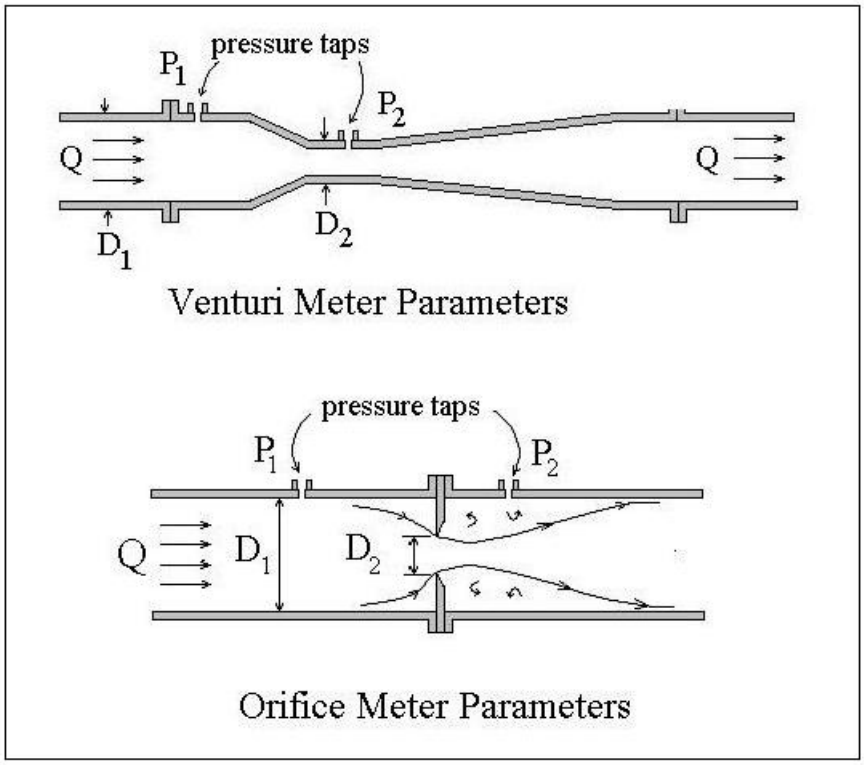

Figure 1.1: Flow pattern through orifice plate.

readings that can occur from pressure differential meters spending extended periods of time in the flow [9-15]. Venturi fouling occurs when particles in the flow gather in the thin small diameter region of a venturi flow meter, and orifice plate degradation occurs from abnormal changes on the edge of the opening in the orifice plate. Since these issues change the specific geometry of the meter, maintaining high measurement accuracy requires periodic laboratory calibrations. The size and weight of the flow measurement section, and the fact that it must not be disassembled, make this task difficult and expensive.

The requirement of inserting the flow meter into the flow, which is the case of venturi and orifice-plate meters, requires cutting pipes and is a difficulty and a hazard for some applications. For virtually all piping applications, flow has to be stopped in order to insert a flow meter. Not only is this disruptive to industry operations, but for more hazardous applications such as nuclear power plants, flow must also be drained, and the area cleaned of possible hazardous materials, prior to flow meter insertion.

1.2 Electromagnetic Flow Meters

Electromagnetic flow meters are the most commonly used flow meters after mechanical and pressure differential flow meters. They are based on the principle of electromagnetic induction. For a conducting fluid, the application of an external magnetic field induces a potential difference proportional to the velocity of the fluid, as shown in Figure 1.2. [16]. These meters require electrically insulated pipe surfaces, and are subject of drift due to sensitivity of the electrodes to small deposits. Also, the installation of electromagnetic flow meters requires cutting pipes.

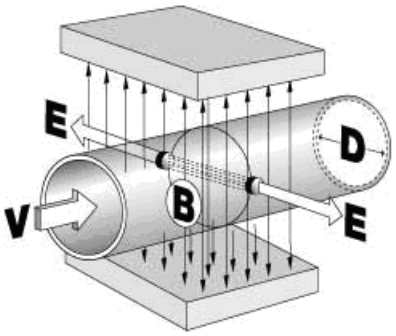

Figure 1.2: Electromagnetic flow meter concept.

1.3 Ultrasonic Flow Measurement

Due to the difficulties encountered with the flow meters described above, *Ultrasonic* flow meters have been gaining popularity in recent decades [17-48]. Ultrasonic flow meters are based on non intrusively transmitting ultrasonic beams through a pipe, and detecting the beams on the other end. Flow rate is determined by analyzing the ultrasonic beam after it is received by a detector. Some ultrasonic meters are clamp-on, meaning the ultrasonic devices are attached to the exterior of the pipe wall, and ultrasonic beams are transmitted through the pipe wall. Such a method does not require inserting anything into a pipe. The three more common forms of ultrasonic flow measurement are *Transit Time*, *Doppler*, and *Cross Correlation*.

1.3.1 Transit Time Flow Measurement

Transit time flow measurement is based on sending an ultrasonic beam diagonally through a pipe, such that the beam crosses the pipe in the radial direction, but also travels along or against the direction of the flow, that is, along the axial direction as well [17,19,20,22-31]. Figure 1.3 shows an example of a Transit Time meter, where a signal is sent along one direction of the flow, and against the direction of the flow.

The difference in travel time between the two diagonal paths can be used to derive the flow velocity. Knowing this difference in time, along with the

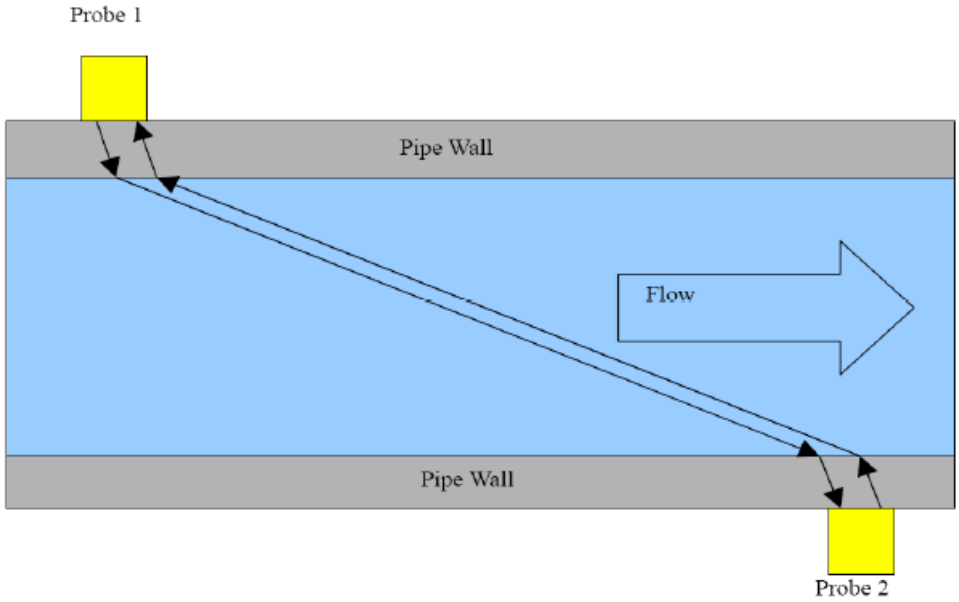

Figure 1.3: Transit Time flow meter concept.

speed of sound, a simple geometric exercise calculates the average flow velocity along the direction of the ultrasonic beam. If the velocity distribution in the pipe is known, the measured velocity can be corrected to obtain the cross-section area average velocity and correspondingly, the volumetric flow rate. Flow meters such as the one shown in Figure 1.1 require high time resolution of measurement, to measure the difference in travel time accurately. The following exercise demonstrates this:

For simplicity, the pipe walls will be neglected for this exercise. Let L be the distance between the probes, c be the speed of sound in the fluid, and v be the magnitude of the projection of the flow velocity onto the direction of the ultrasonic beam. Then, the time it takes an ultrasonic beam from Probe 1 to reach Probe 2 is $t_1 = L/(c+v)$, and the time it takes the returning beam from Probe 2 to reach Probe 1 is $t_2 = L/(c-v)$. The difference between the two time values is then $\Delta t = t_2 - t_1 = 2vL/(c^2 - v^2)$. Since v^2 is much smaller than c^2 , we may approximate that $\Delta t \approx 2vL/c^2$. For typical values of $L = 0.5m$, $v = 5m/s$, and the speed of sound in water as approximately

1500m/s, $\Delta t \approx 2.2 \times 10^{-6} s$. To measure values such as these, with an accuracy of 1%, the Transit Time meter must measure time with a resolution of 10^{-8} seconds. The Cross Correlation Flow Meter, for comparison, typically needs to measure time with a resolution of 10^{-3} seconds.

Transit Time meters can also be designed such that there is only one beam traveling in one direction relative to the flow. For such a design, the flow rate is derived from calculating the difference between the measured travel time of the beam, and the expected travel time of the beam in stationary fluid. Although the difference between the travel time of two beams is not calculated in such a design, the speed of sound and travel time of one beam still need to be calculated to high accuracy.

Also, the angle of the ultrasonic beams (see Figure 1.3) depend on the speed of sound in the pipe material and in the flow, which depend on the temperature. In an environment with changing temperature, the angle of the beams could change during measurement, and transmitted beams will no longer be aimed at the receiving probes. This would cause errors in measurement, the importance of which is amplified by the required accuracy of measurement explained above. As a result, a slight change in temperature can alter the measurement significantly. This issue is often dealt with by placing the probes inside the pipe, in which case installation of the meter requires stopping the flow and cutting the pipe, and measurement is no longer non-intrusive. Thus, its use becomes limited [23,29-31].

1.3.2 Doppler Flow Measurement

Doppler flow measurement is based on reflecting ultrasonic beams off of particles moving with the flow [17,19,21]. This method is limited in applicability and accuracy. Since particles moving within the flow do not necessarily move at the velocity of the cross section average flow velocity, accurate measurement using the Doppler method requires detailed knowledge of the relationship between particle velocity and average flow velocity, which is not always available. Also, conducting Doppler flow measurements may require insert-

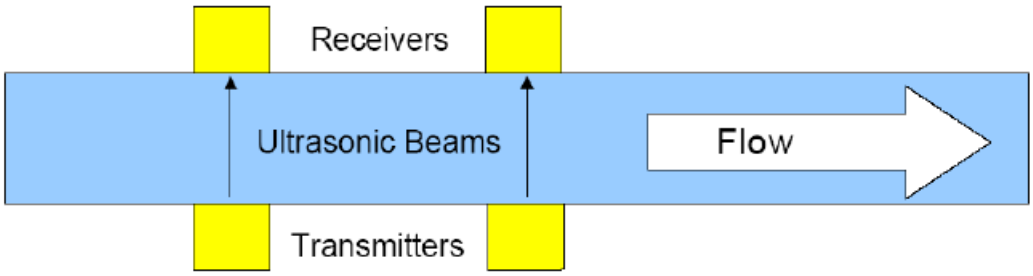

Figure 1.4: Cross Correlation Flow Meter concept.

ing the meter into the flow, making it no longer non-intrusive or clamp on, hence losing the benefits that promote the use of ultrasonic flow meters.

1.4 Cross Correlation Flow Measurement

Cross correlation flow meters are not as commonly used as Transit Time meters, but have several advantages, and are growing in popularity in recent years [18,32-49]. The operating principals of the cross correlation flow meter are as follows: Ultrasonic beams are continuously sent through two different cross-sections of a pipe, perpendicular to the pipe wall. The beams are continuously received on the other end of the pipe. The transmitters and receivers are set up outside of the pipe, allowing non-intrusive operation of the meter, and installation without cutting pipes. The distance between the upstream and downstream beams is called *Transducer Spacing*. Figure 1.4 shows a simplified diagram of a cross correlation flow meter setup.

As the ultrasonic signals pass through the pipe cross-section, they are altered by turbulent structures within the flow, called turbulent eddies. A simplified version of this effect is shown in Figure 1.5, where the beam frequency is altered by a single eddy. In reality, the transmitted signal is altered by a turbulent flow consisting of many eddies, referred to below as the turbulent picture.

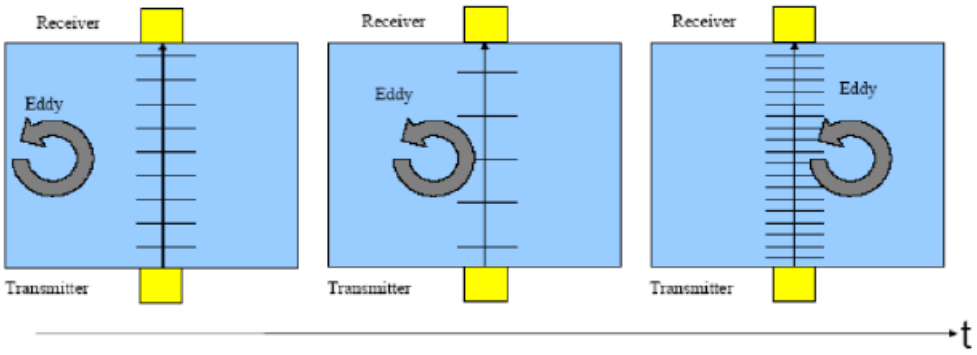

Figure 1.5: Eddy altering the frequency of an ultrasonic signal as it passing through the beam.

In order to measure laminar flow using the cross correlation flow measurement technique, a second substance must exist in the flow, such as air bubbles, in order to alter the transmitted ultrasonic signals in the absence of turbulent structures. This is practically never an issue in industry though, because the overwhelming majority of industrial flow is turbulent.

As an eddy passes through the downstream beam, it alters it in almost the same way as it altered the upstream beam. The reason the two beams are not altered identically is because turbulent structures can deform while between the beams. The received signals are demodulated, removing the effect of carrier frequencies, and leaving only the signatures of turbulent eddies. The result is two demodulated signals, as functions of time. The downstream demodulated signal is very similar to the upstream demodulated signal, if shifted in time by the amount of time it took the turbulent picture to move from one beam to the next. The value of this time shift, called *time delay*, and represented as τ_m, is determined by taking the cross correlation of the two demodulated signals. The cross correlation of two functions $x(t)$ and $y(t)$ is,

$$x(t) \star y(t) = \frac{1}{T} \int_0^T x(t)y(t+\tau)dt \tag{1.1}$$

where T is the time span of $x(t)$ and $y(t)$, which is the same for both functions. The cross correlation has an absolute maximum, hence forth referred to as *peak*, at $\tau = \tau_m$.

By knowing the time delay, and the transducer spacing L, one may determine the axial velocity of the turbulent structures through the pipe, with the formula,

$$U_m = \frac{L}{\tau_m} \tag{1.2}$$

Conducting a single cross correlation flow measurement, obtain a single U_m value, takes seconds. Cross correlation flow measurement is conducted by continuously measuring the flow through a pipe, obtaining a new U_m value every few seconds. Since the turbulent structures traveling through the pipe are different with every measurement, but have shared statistical properties, U_m will be different for different measurements, but the average value of U_m, represented as V_m, remains stable. V_m is close to the time averaged cross section average flow velocity, but not necessarily equal to it. The actual time averaged cross section average flow velocity, V_a, is calculated by a hydraulic factor C, where

$$C = \frac{V_a}{V_m} \tag{1.3}$$

The work presented in this thesis was conducted to develop a mathematical model for deriving the hydraulic factor C. Since C relates the transport velocity of turbulent structures to the cross section average flow velocity, a mathematical model for predicting C must be based on an adequate turbulence model.

1.4.1 History of Cross Correlation Flow Measurement

Originally, cross correlation flow measurement technology was developed in England for measuring multi-phase flow [18]. The first cross correlation flow meter for measuring single-phase flow was developed at Canadian General Electric by Ralph Flamons [33].

The volumetric flow rate Q in a pipe can be calculated as $Q = A \cdot V_a$, where A is the cross section area of the pipe, and V_a is the time averaged cross section average flow velocity, sometimes referred to as *cross section average flow velocity*, or just *average flow velocity*. The Cross Correlation Flow Meter measures the velocity of turbulent eddies, which is not necessary equal to the average flow velocity V_a. The relation between the velocity measured by the Cross Correlation Flow Meter, referred to as measured velocity V_m, and cross section average velocity V_a is a subject of major interest in the field of accurate flow measurement. Problems of this nature are common for flow measurement techniques, and are not unique to the Cross Correlation Flow Meter. What is unique to the Cross Correlation Flow Meter is that solving this problem requires a high level understanding of turbulence. For the cross correlation flow meter to be used, a method must exist that assigns the correct value for V_a given a value for V_m.

In the 1970s and 1980s, when the use of the cross correlation flow meters began to increase, the meter was completely empirical, and there was no understanding of how turbulent eddies affected the ultrasonic beam. The link between V_a and V_m was established experimentally in laboratory testing as follows [34]:

The flow meter would be taken to a laboratory where a piping system would be set up to mock flow conditions seen in a specific application. Then, the cross correlation flow meter, as well as another reference meter, would be used to measure flow. The most accurate reference flow measurement is

achieved by using the weight tank method. By this method, the cross correlation flow meter was calibrated in the laboratory before being used in the field. This method of calibration has drawbacks. First of all, industrial conditions involving extreme temperatures and high Reynolds Numbers (Re), such as those found in nuclear power plant feedwater systems, can not be recreated in ordinary laboratories existing today. Instead, similar piping systems that achieve low Re are used for such calibration, and extrapolation to high Re must be conducted. Also, the procedure of calibration in the laboratory is time consuming and expensive.

One such calibration was conducted in the 1990s by Ontario Hydro. In this project, a replica of the feedwater system of a CANDU nuclear power plant was built, and real feedwater flow conditions were achieved with a flow rate of approximately 300 l/s, a temperature of approximately 200 degrees Celsius, and Re of up to 11,000,000. This testing provided a basis for feedwater flow measurement in CANDU plants with accuracy better than 2% [34].

In 1994, a Canadian company called Advanced Measurement and Analysis Group Inc. (AMAG) received a government research grant for developing a basis for the improvement of the uncertainty of cross correlation flow measurement technology. In this study, it was shown that under certain common flow conditions, the phase shift in the received signal occurs due to a Doppler frequency shift of the ultrasonic wave, caused by turbulent velocity fluctuations. It was also shown that this shift may be defined by the following equation:

$$\Phi(x,t) = \frac{f}{c^2} \int_{-R}^{R} v(x,y,t)dy \tag{1.4}$$

Where ϕ is the demodulated received signal, f is carrier frequency, c is speed of sound, R is the pipe radius at the location and orientation of measurement, v is radial turbulent velocity, t is time, y is the radial direction, and

x is the axial direction [35]. Combining this equation with known experimental data on developed pipe flow, a relation between V_m and V_a, dependent on Re, was derived and validated in laboratory testing [35,40-42,44]. The weakness of this method is that for every installation of the cross correlation flow meter, additional studies must be conducted to determine if the approximations based on data from developed flow are applicable to the given flow.

A more accurate theoretical model was developed at Penn. State University. This model was based on using Equation (1.4) and on the Frozen Turbulence Approximation [45,46]. The weakness of this model is that realistic turbulence in pipe flow is not accurately described by the Frozen Turbulence Approximation.

Other attempts to develop a theoretical model of cross correlation flow measurement have been made, but those models were not based on a detailed analysis of fluid dynamics phenomena [38,39,43,48].

With the current level of cross correlation flow measurement technology, it is possible, under proper conditions, to measure flow with an uncertainty of 0.5% or better. It is not always clear though, when such proper conditions exist. Today, cross correlation flow meters are installed in a number of nuclear power plants . Their applications include correction of venturi meter and orifice-plate meter measurements [40,41,47].

A common problem in industrial flow measurement today, related to all flow measurement technologies, is traceability of field measurements to laboratory calibrations. The most difficult aspect in establishing traceability is the fact that flow conditions in the field are not identical to flow conditions in the laboratory [50]. Solving this problem requires extensive knowledge of how characteristics of the flow affect behavior of the specific flow measurement technology used, and how these flow characteristic in the field compare to those in the laboratory. Hence, a model of cross correlation flow measurement must be based on analysis of fluid dynamics phenomena, and how they affect cross correlation flow measurement. For this reason, a large portion of

the work presented in this thesis is on the subject of modeling of the behavior of turbulence .

1.4.2 Turbulence Modeling

As mentioned above, the cross correlation flow meter measures the transport velocity of turbulent structures. In order to obtain the cross section average flow velocity, or the average mass flow velocity, the relationship between the transport velocity of turbulent structures and the cross section average flow velocity must be established. This requires a deep understanding of the process of transport of turbulence structures in turbulent flow.

Theoretical and experimental investigation of turbulent flow is one of the fundamental problems in modern physics, and is the subject of a significant number of publications [50-85]. The numerous models developed to describe turbulent flow can be separated into two main categories: Models that focus on time-averaged flow characteristics [52,58-61,64,67,69,70,78,81,82], and models that consider time dependent turbulent structures [51-57,60-63,65,66,68,71-77,79,80,83-85]. Modeling cross correlation flow measurement requires using both types of approaches.

It can be shown, from work done by Andrey Kolmogorov [51], that turbulent eddies, although constantly deforming, remain recognizable as they travel with the flow of a fluid, for a path length greater than the length scale of the turbulence structures. For example, turbulent eddies with characteristic length comparable to the length of a pipe diameter, will be recognizable as they move through a pipe, for a distance greater than the length of the pipe diameter. Therefore, turbulent eddies can be used as a tracer, provided the domain of measurement is of a length comparable to the characteristic length of the eddies used as a *tracer*. A *tracer* is a recognizable feature or object within a flow, who's velocity can be measured in order to deduce the flow velocity [86]. In pipe flow, the largest eddies have characteristic length of order of the length of the pipe diameter. Hence, since cross corre-

lation flow measurement uses the signature of turbulent eddies as a tracer, cross correlation flow measurement should work, provided that the distance between upstream and downstream ultrasonic beams is comparable to the length of the pipe diameter. This estimation explains why cross correlation flow measurement works, but does not provide a relationship between the transport velocity of turbulent structures and the cross section average flow velocity. Describing such a relationship requires the modeling of the motion of turbulent structures for various flow conditions.

Turbulent Flow Models

Modeling of turbulent flow is a very difficult mathematical problem, that can not be solved directly for the majority of industrial application within practical time frames, even using the most powerful modern computers. Therefore, different types of approximate models are used.

For a non-compressible fluid, and no external forces, flow is governed by the Navier-Stokes equations.

$$\frac{d\vec{u}}{dt} + (\vec{u} \cdot \nabla)\vec{u} = -\frac{1}{\rho}\nabla p + \nu\nabla^2\vec{u} \tag{1.5}$$

$$\nabla \cdot \vec{u} = 0 \tag{1.6}$$

where $\vec{u} = \vec{u}(u, v, w)$ is the flow velocity vector with u, v, and w being the Cartesian components in the x, y, and z direction respectively, p is pressure, ρ is density, and ν is kinematic viscosity.

Most computational methods of modeling turbulent flows are time averaged, based on taking the time average of every term in the Navier-Stokes

equations, and modeling time dependent affects prior to solving the system of equations. Such simulation models are called Reynolds Averaged Navier-Stokes (RANS) simulations. Solving the time-averaged Navier-Stokes equations, called the Reynolds Equations, requires additional models to close the system. Since RANS simulations do not model turbulent structures, they are not capable of describing cross correlation flow measurement [52].

Computational fluid dynamics methods that do model turbulent structures, fall into three categories: Direct Numerical Simulation (DNS), Large Eddy Simulation (LES), and Synthetic Turbulence simulation.

DNS models solve the Navier-Stokes equations directly [52,53,61,75,79,80]. In order to reproduce turbulence, the space and time resolution of the numerical algorithm should be of order of magnitude smaller than the space and time scales of the turbulent motion in the flow. The higher the Reynolds Number, the smaller the turbulence scales. For typical industrial flow, Reynolds Numbers are quite high, of order of $10^6 - 10^7$. Direct numerical simulation of such flow requires an impractical amount of time and computer power. DNS is used to solve relatively simple problems set in small computational domains and small Reynolds Numbers.

LES is a combination of RANS and DNS [71-77,84]. LES separates turbulent structures into large and small scales, based on the Kolmogorov turbulence scales. LES models the temporal and spacial averaged affects of small scale turbulent structures, and calculates the behavior of larger scale turbulent structures. LES modeling can be conducted in much more reasonable time frames than DNS modeling, making it useful for more applications. LES could be a useful method for modeling cross correlation flow measurement, however, considering the fact that cross correlation flow measurement is applied to industrial flows with Reynolds Numbers up to tens and hundreds of millions, the required calculation time of LES becomes too long to conduct practical analysis.

Synthetic Turbulence simulation is a unique approach to turbulence mod-

eling, and can be conducted in very reasonable time frames [83-85]. Artificial turbulent structures, such as mathematical structures based on random sequences or sinusoidal function, are created, and their space time evolution is calculated based on a flow model. The flow model used can be DNS, LES, RANS, or something simpler such as a Frozen Turbulence Approximation. The artificial turbulence is created such that it has the statistical properties that real turbulence would have in the modeled flow condition. Therefore, although Artificial Turbulence modeling does not model the exact turbulent structures that would appear within a given flow, it does model how turbulent structures within a given flow would evolve. Synthetic turbulent simulations can be conducted in much shorter time frames than LES, even if using personal computers and simulating high Reynolds Number flows.

A common approximation used in turbulent flow modeling is the Taylor Hypothesis, often referred to as the Frozen Turbulence Approximation. This model approximates turbulent structures as non-deforming, and being transported along the flow with a time averaged flow velocity. The applicability of this model for different types of flow is examined in a number of papers [87-99]. One of the recent models of cross correlation flow measurement is based on this approximation [45,46]. The validity of the Frozen Turbulence Approximation is not thoroughly examined in those works though, hence the applicability of this approximation to pipe flow remains questionable.

Chapter 2

Theoretical Analysis of the Dynamics of Turbulent Structures in Application to Cross Correlation Flow Measurement

Operation of the cross correlation flow meter is based on the fact that certain characteristics of the turbulent velocity field remain invariant while transported along a pipe. Let us call their average velocity *measured velocity* V_m. Understanding how V_m is related to flow characteristics, such as time-average velocity components and turbulence, is a fundamental problem of cross correlation flow measurement technology, and was investigated by many authors [34-47]. It is intuitively clear, and can be shown mathematically, that if a velocity field consisted of frozen turbulent structures moving along a pipe with constant velocity U_0, the velocity U_0 will be measured by the cross-correlation flow meter. This approximation of turbulent motion, called the *Frozen Turbulence Approximation* is commonly used in analysis of the cross correlation flow measurement method [45,46]. In some studies, the *Locally Frozen Turbulence Approximation* is made [45,46], which assumes that turbulent velocity is transported along streamlines of the time-average flow.

This approximation provides reasonable agreement with experimental data, although the validity of this assumption was never considered in those studies.

Unlike previous approaches to develop a theoretical basis for cross correlation flow measurement, the analysis developed by the author and presented in this thesis does not assume isotropic homogeneous turbulence, or directly use the frozen turbulence approximation. Instead, the validity of the frozen turbulence approximation is examined, and the conditions of its applicability to cross correlation flow measurement are analyzed. Quantitative parameters, which define the validity of the locally frozen turbulence approximation, are obtained. One of the interesting results derived in this chapter, is that although the applicability of the locally frozen turbulent approximation to the turbulence velocity field is limited, in channel flow the approximation may still be used to describe the space-time development of certain integral characteristics of the velocity field, such as the radial and angular integral of radial turbulent velocity. This result is used in Chapter 3, in order to construct a numerical model of the development of a turbulent velocity field along a channel, which is then used to simulate cross correlation flow measurement.

The theoretical analysis presented in this chapter provides a new level of quantitative understanding of space-time development of turbulence in channel flow, and the basis of cross-correlation flow measurement technology.

2.1 Analysis of the Vortex Transport Equation for Pipe Flow

All flow is governed by the Navier-Stokes equations, given below (2.1), for a non-compressible fluid and no external forces, along with the equation for conservation of mass (2.2) [52]. These equations are given using Einstein summation notation.

$$\frac{\partial u_j}{\partial t} + u_i \frac{\partial u_j}{\partial x_i} = \frac{-1}{\rho} \frac{\partial p}{\partial x_j} + \nu \frac{\partial^2 u_j}{\partial x_i \partial x_i} \tag{2.1}$$

$$\frac{\partial u_i}{\partial x_i} = 0 \tag{2.2}$$

where u is a velocity component, ρ is the density, p is pressure, and ν is kinematic viscosity.

2.1.1 Vorticity Equations

The left side of the Navier-Stokes equations describe the transport of fluid velocity components through a fluid medium. As described in previous sections, the cross correlation flow meter measures the transport velocity of turbulent structures detected by the ultrasonic beam due to radial turbulent velocity affecting the ultrasonic signal. The pressure term on the right side of equation (2.1) complicates analysis of the transport of the fluid velocity components. By applying the curl operator to every term in equation (2.1), and taking into consideration the conservation of mass equation (2.2), one obtains the vorticity equations for a non-compressible fluid and no external body forces, given below. The vorticity equations describe the transport of vorticity through a fluid medium, and do not contain term with the pressure gradient. This form of the Navier-Stokes equations is often used when studying fluid dynamics[51-53]. Also, it is known that in turbulent channel flow, the effect of viscosity is significant in a small area near the wall and can be neglected for the major part the channel [102]. As a result, the following vorticity equation can be obtained:

$$\frac{\partial \omega_j}{\partial t} + u_i \frac{\partial \omega_j}{\partial x_i} + \omega_i \frac{\partial u_j}{\partial x_i} = 0 \tag{2.3}$$

where

$$\vec{\omega} = \nabla \times \vec{u} \tag{2.4}$$

The first two terms in Equation (2.3) describe the transport of vorticity by the flow velocity, and the last term is responsible or generation of vorticity along the flow [52].

2.1.2 Order of Magnitude Analysis of the Vorticity Equation for Channel Flow

Velocity in equation (2.3) may be redefined as follows,

$$u_j = u_{j0} + u'_j \tag{2.5}$$

where

$$u_{j0} >> u'_j \tag{2.6}$$

In equations (2.5) and (2.6), u_{j0} is the time averaged velocity, and u'_j is the turbulent fluctuation velocity. By substituting equation (2.5) into (2.3), one obtains the following equation.

$$\frac{\partial \omega_j}{\partial t} + u_{i0}\frac{\partial \omega_j}{\partial x_i} + \omega_i \frac{\partial u_{j0}}{\partial x_i} + u'_i \frac{\partial \omega_j}{\partial x_i} + \omega_i \frac{\partial u'_j}{\partial x_i} = 0 \tag{2.7}$$

For quantitative estimation of the terms in Equation (2.7), the following parameters describing the order of magnitude of velocities and spacial scales can be introduced, where the symbol $\tilde{}$ indicates order of magnitude:

$$\begin{aligned}
u_{i0} &\sim u_0 \\
u'_i &\sim u' \\
\omega_i &\sim \omega \\
\frac{\partial \omega_j}{\partial x_i} &\sim \frac{\omega}{l} \\
\frac{\partial u'_j}{\partial x_i} &\sim \frac{u'}{l} \\
\frac{\partial u_{j0}}{\partial x_i} &\sim \frac{u_0}{L} \\
u_0 &>> u' \\
L &>> l
\end{aligned} \tag{2.8}$$

In (2.8), u_0 and u' are the order of magnitude of the time averaged velocity and turbulent velocity components, respectively. Parameters L and l are spacial scales of the characteristic distance over which the time averaged

velocity and turbulent velocity, respectively, change by a significant quantity. It is assumed that the turbulent velocity components are much smaller than the average flow velocity, and the spacial scale of turbulent velocity changes is much smaller than the spacial scale of time averaged velocity changes. With these assumptions, the terms in Equation (2.7) can be estimated as follows:

$$u_{i0}\frac{\partial \omega_j}{\partial x_i} + \omega_i \frac{\partial u_{j0}}{\partial x_i} + u'_i \frac{\partial \omega_j}{\partial x_i} + \omega_i \frac{\partial u'_j}{\partial x_i} \sim u_0 \frac{\omega}{l} + \omega \frac{u_0}{L} + u' \frac{\omega}{l} + \omega \frac{u'}{l} \tag{2.9}$$

Dividing every term in (2.9) by the constant $u_0\omega/l$ gives the following:

$$\frac{l}{u_0\omega}(u_{i0}\frac{\partial \omega_j}{\partial x_i} + \omega_i \frac{\partial u_{j0}}{\partial x_i} + u'_i \frac{\partial \omega_j}{\partial x_i} + \omega_i \frac{\partial u'_j}{\partial x_i}) \sim 1 + \frac{l}{L} + \frac{u'}{u_0} + \frac{u'}{u_0} \tag{2.10}$$

Considering the fact that l/L « 1 and u'/u0 «1, the following inequality becomes clear:

$$\left| u_{i0}\frac{\partial \omega_j}{\partial x_i} \right| >> \left| \omega_i \frac{\partial u_{j0}}{\partial x_i} + \text{`}u'_i \frac{\partial \omega_j}{\partial x_i} + \omega_i \frac{\partial u'_j}{\partial x_i} \right| \tag{2.11}$$

Equation (2.3) may therefor be approximated as follows.

$$\frac{\partial \omega_j}{\partial t} + u_{i0}\frac{\partial \omega_j}{\partial x_i} = 0 \tag{2.12}$$

Equation (2.12) describes vorticity change along the stream-line, defined by the time-averaged velocity components. It is clear that the neglected

terms (including viscosity terms) will produce a significant change of vorticity over long distances along the stream-line. For distances of order of magnitude of L, though, the vorticity development is described by equation (2.12)

2.1.3 Change of Variables

In typical channel flow, the time averaged velocity component along the direction of the channel is much greater than the other two time-averaged velocity components. The length scale of the change of the time-averaged velocity component along the channel is also significantly higher than the length scales of time averaged velocity changes in the other two directions. Therefore, a simplified form of the partial differential equation (2.12) may be achieved by applying the following change of variables:

$$\begin{aligned} \zeta &= x \\ \eta &= y \\ \tau &= z \\ \xi &= \frac{x}{U} - t \end{aligned} \tag{2.13}$$

where U is the x-component of u_{j0}. For the case of pipe flow in the x-direction, and a section of the pipe of length of order magnitude of a pipe diameter, the x-component of u_{j0} is much greater than the other components, and U may be regarded as independent of x. From these approximations, the following relation can be obtained from equation (2.12).

$$U\frac{\partial \omega_j}{\partial \zeta} = 0 \tag{2.14}$$

Equation (2.14) demonstrates that vorticity, ω, is independent of location along the dominant direction of flow as it moves with velocity U, given that all other variables remain constant. More specifically, if an observer were to move along the x-direction with velocity $U(y, z)$ while maintaining his y-coordinate and z-coordinate constant, he would always observe the same value for vorticity. Equation (2.14) may appropriately be referred to as a locally frozen vorticity approximation. In the classical frozen turbulence approximation, regarding vorticity, U is a constant through all space and time, where as in equation (2.14) it is a constant through time and along the dominant direction of flow, but U is not a constant along the other two spacial directions. Hence, equation (2.14) demonstrates frozen vorticity along stream-lines defined by particular values of y and z, but does not demonstrate classical frozen vorticity over all space-time. The physical difference between the locally frozen vorticity approximation presented by equation (2.14) and the classical frozen turbulence approximation, is that in the frozen turbulence approximation, turbulent structures do not deform as they are transported, where as according to equation (2.14), turbulent structures deform as they are transported.

2.2 Relation Between Vorticity Transport and Cross Correlation Flow Meter Signal for the Two-Dimensional Case

It was discussed in Chapter 1 that in ultrasonic cross-correlation flow measurement, ultrasonic waves travels across a pipe and are modulated by the turbulent velocity field. The phase modulation of the wave is proportional to the instantaneous value of the integral of the turbulent velocity component along direction of the ultrasonic wave. Therefore, the demodulated signal obtained through cross correlation flow measurement may be represented as follows [35,45].

$$\phi(x,t) \propto \int_{-R}^{R} v(x,y,t)dy \tag{2.15}$$

Where v is the radial component of the velocity field, y is the radial direction, and x is the dominant direction of the flow and hence the axial direction of the pipe.

The remainder of this chapter will present analysis of how the signal described by equation (2.15) depends on x and t if the vorticity in the flow is described by equation (2.14). To better understand this relation, analysis is conducted for a simple case of two-dimensional flow where an analytical solution can be obtained.

Let us assumed that at a given time in infinite space, there is a turbulent velocity field with a corresponding vorticity field.

When particular criteria are met, it is possible to determine a velocity field from a given vorticity field, at a given instance of time, by the following formula [100].

$$\vec{u} = \int\int\int \frac{\vec{\omega} \times (x-\xi, y-\eta, z-\zeta)}{((x-\xi)^2 + (y-\eta)^2 + (z-\zeta)^2)^{3/2}} d\xi d\eta d\zeta \tag{2.16}$$

Formula (2.16) gives the velocity as a function of coordinates x, y, and z. ω is a function of spacial coordinates ξ, η, and ζ, not related to the ξ, η, and ζ used in the change of variables in the previous section. Integration is performed over these coordinates, summing the influence of the vorticity at every location.

A two dimensional approximation would set

$$\vec{\omega} = (0, 0, \omega_\zeta) \tag{2.17}$$

By substituting (2.17) into (2.16), and considering only the y-component of the velocity, since that is the component the demodulated signal is dependent on, and integrating over ζ, one obtains the formula for determining the y-component of a velocity field v, corresponding to the vorticity field ω_ζ.

$$v = 2 \int \int \frac{\omega_\zeta (x - \xi)}{(x - \xi)^2 + (y - \eta)^2} d\xi d\eta \tag{2.18}$$

Consider a straight line segment, in direction of y-coordinate, in the (x, y) plane. The integral of v over this line segment, as in equation (2.15), will now be determined. By substituting (2.18) into (2.15) and integrating over y, one obtains the following formula

$$\phi(x, t) \propto 2 \int \int \omega_\zeta (\tan^{-1}(\frac{R - \eta}{x - \xi}) + \tan^{-1}(\frac{R + \eta}{x - \xi})) d\xi d\eta \tag{2.19}$$

Integral in (2.19) has a very simple geometrical interpretation. The factor that ω_ζ is multiplied by in (2.19) is the angle α shown in Figure 2.1, with a positive sign for ξ less than x, and a negative sign for ξ greater than x, where x is the x-coordinate of the location of the line segment analogous to an ultrasonic beam, and ξ is the x-coordinate of the location of the contributing vorticity source.

In Figure 2.1, the location of the vorticity source is outside of the pipe. This is because in order to use equation (2.16), the vorticity field must be defined for all location in space, including locations outside of the pipe wall.

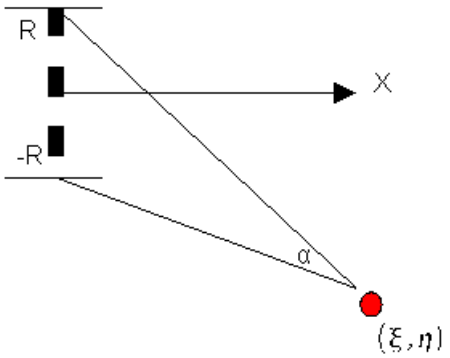

Figure 2.1: Angle formed by connecting curl source with ends of ultrasonic beam.

The effect of the wall must then be generated by defining an appropriate vorticity field that acts as a wall at the desired locations. This is discussed later in this section [100].

In polar coordinates, the formula for α is

$$\alpha(r,\theta,x) = \tan^{-1}(\frac{R - r\sin(\theta)}{x - r\cos(\theta)}) + \tan^{-1}(\frac{R + r\sin(\theta)}{x - r\cos(\theta)}) \tag{2.20}$$

For the polar coordinate equivalent to Figure 2.1, see Figure 2.2.

For any given r value, the absolute value of α is largest for values of $\theta = 0$ or $\theta = \pi$. For such values of θ, it can be shown with limit analysis that for large r the absolute value of α tends to zero as $2R/r$ tends to zero. For other values of θ at the same r value, α has smaller values.

To demonstrate that the integral on the left side of (2.19) converges, we will consider the integral

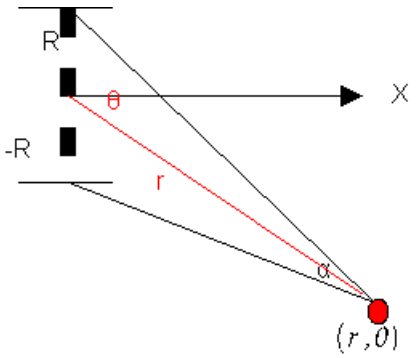

Figure 2.2: Angle connecting curl source with ends of ultrasonic beam in polar coordinates.

$$\int_0^\infty \frac{\omega_\zeta}{r} dr \tag{2.21}$$

It is clear that (2.19) converges if and only if (2.21) converges. If ω_ζ is a constant, (2.19) is undefined, but the nature of ω_ζ is that it is not a constant. Since ω_ζ is the result of turbulent fluctuations in the velocity field, its distribution in the (x, y) plane is random variations around zero. Let us assume that the typical magnitude of ω_ζ is W, and the typical spacial scale of variation of ω_ζ is l. Integrating ω_ζ over an area with radius $r = a$, where a is much larger than typical scale of variation l, should give a value of the same order of magnitude as the value obtained by integrating ω_ζ over area with $r = b$, where b is much larger than typical scale of variation l, for all a and b. Therefore, when r tends to infinity, the integral in (2.21) tends to a constant value with order of magnitude $1/r$. Hence, the integrals of (2.19) and (2.21) are defined. The analytical solution for the demodulated signal in two dimensions, derived from known vorticity, can therefore be represented as

$$\phi(x,t) \propto \int_0^\infty \int_{-\pi}^{\pi} \omega_\zeta(r,\theta,t)\alpha(r,\theta,x) d\theta dr \tag{2.22}$$

The result given by equation (2.22) has the following geometrical interpretation. In order to calculate the integral of a velocity field along a straight line segment through space, knowing the vorticity field in all space, one must do the following: integrate over all space, the vorticity field weighted by the angle formed between two lines connecting the location of vorticity to the ends of the line segment along which the integral of velocity is being calculated.

A noteworthy similarity exists between equation (2.18) and equation (2.22). According to equation (2.18), in order to calculate the velocity field from a known vorticity field, one must integrate over all space, the vorticity field multiplied by a weight function, that function being the inverse distance from the vorticity location to the location where calculation of the velocity is desired. According to equation (2.22), in order to calculate the integral of the velocity field from a known vorticity field, one must also integrate over all space, the vorticity field multiplied by a weight function, that function being the angle α.

In equation (2.22) the vorticity distribution depends on time. If at a given time this distribution is known, its dependence on time is approximately described by equation (2.14). The physical significance of this result is as follows: Equations (2.22) and (2.14) explain why the demodulated signal changes as it is transported along a pipe, and as a result the demodulated signal collected at a downstream pipe cross section will never be identical to a demodulated signal collected at the upstream pipe cross section. If the frozen turbulent approximation were true, then the entire vorticity field would be transporting in the dominant flow direction x, without deformation, and the spacial integral of the vorticity field along a line segment, weighted by the angle a, would repeat, identically, at downstream line segments of equal length and location along the y-axis, at later moments in time. Hence, if the frozen turbulence approximation were true, a demodulated signal recorded at an upstream cross section, would be recorded identically at a downstream cross section at a later time. Since vorticity is not perfectly frozen, but is locally

frozen along streamlines defined by a y-value as is described by equation (2.14), the integral of the vorticity field along a line segment weighted by the angle α will not repeat identically at a downstream line segment of identical length and position along the y-axis. The non-frozen character of the vorticity field will cause turbulent structures to deform as they are transported downstream. Hence, once turbulent structures move from the upstream location to the downstream location, the vorticity field has changed, and the integral of the field, weighted by α, will not be the same. Demodulated signals collected at two different locations at the same time will also be different, because although the integrated vorticity fields are identical, the weights of α will be different for the two locations. Figure 2.3 shows how a locally frozen vorticity field results in deforming turbulent structures, while a vorticity field under the classical frozen turbulence approximation does not, using a cloud as an example of a turbulent structure. Formation and dissipation of structures, as well as structure to structure interaction, is not modeled by the frozen or locally frozen turbulence model. As was demonstrated in the theoretical analysis above, the transport terms are the dominant terms describing pipe flow in a domain where axial flow profile can be considered independent of location along the direction of the flow. Hence, transport, and deformation due to non-uniform axial flow profile, and the dominant features of turbulent motion in such flow, and these features are modeled by the locally frozen turbulence approximation.

It is important to note, though, that the demodulated signals not being identical does not imply that they are not similar enough to produce a significant cross correlation. As is observed in cross correlation pipe flow measurement, the upstream and downstream demodulated signals are not identical, but they are similar enough and do produce a significant cross correlation.

In general, the analytical solution given by (2.22) can be used for quantitative analysis of the effect of turbulent scales and time-averaged velocity on the phase modulation of a signal in time and space.

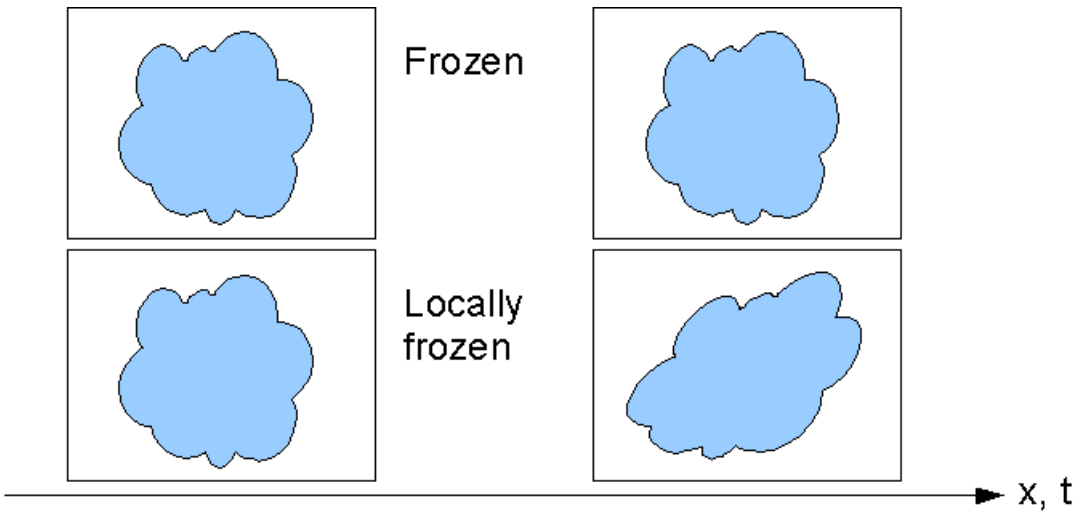

Figure 2.3: Cloud moving through space-time. TOP: Classical frozen turbulence approximation. BOTTOM: Locally frozen turbulence approximation.

Equation (2.16) integrates over all of space in order to calculated the velocity field for a known curl field that is also defined for all of space. For the case of a wall bounded flow, such as channel flow, a similar solution can be obtained by creating a vorticity field outside of the flow domain using a mirror reflection method. Setting all vorticity outside of the walls to 0 does not sufficiently define the vorticity field to solve for the velocity field. If the vorticity for all location outside of the wall were set to zero, the resulting solution for the velocity field will allow for fluid to pass through the walls. Hence, the vorticity field must be defined in a way that not only represents the vorticity in the flow medium, but also represents walls. This can be achieved by treating the locations of the walls as vorticity mirrors [100]. On the side of a wall where the fluid medium exists, the vorticity field is defined as the fluid vorticity field. On the side of a wall where the fluid medium does not exist, the vorticity field is defined as a mirror image of the vorticity field on the side of the wall of the fluid medium.

For the two dimensional case of channel flow, there are two parallel walls. Hence, two mirror images would have to be created in the vorticity field.

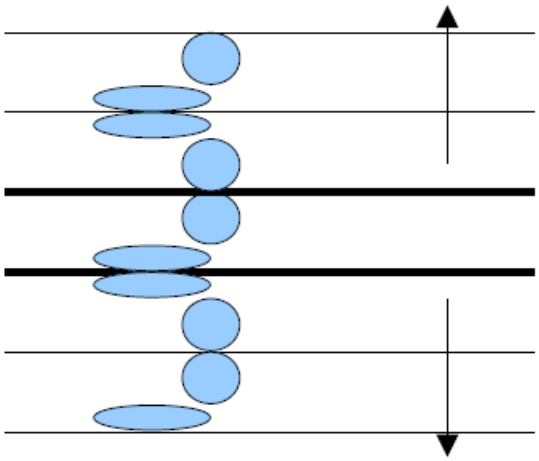

Figure 2.4: Mirror method for modeling walls in a vorticity field.

Each mirror image would contain the image of the opposite wall. For example, consider a pipe, in two dimensions, with a north wall and a south wall. The mirror image on the other side of the south wall will not only present the reflection of the vorticity in the channel, but will also present the reflection of the north wall. Similarly, the mirror image on the other side of the north wall will present the reflection of the south wall. These imaginary walls must also be represented in the vorticity field. Hence, the vorticity field must define reflections of vorticity in the mirror image channels too. This will produce two more imaginary walls, on the other side of which mirrored vorticity will have to be defined again, and so on. The number of mirrored channels that must be defined is finite, because in equation (2.18) the vorticity is weighted by the inverse distance between the location where velocity is calculated and the location of vorticity. Therefore, after a sufficient number of reflections, the weighting value would be so small, that the vorticity can be set to zero. Figure 2.4 demonstrates the mirror reflection method. Bold lines, and shapes between them, indicate real walls and turbulent structures respectively. Other lines and shapes are mirror images intended to model the presence of real and mirror-image walls. Arrows indicate that the mirroring process continues beyond what is shown.

2.3 Relation Between Vorticity Transport and Cross Correlation Flow Meter Signal for the Three-Dimensional Case

In three dimensions, the additional spacial components of vorticity make the mirror reflection method, described for the two dimensional case, more difficult to apply, especially for the case of pipe flow. Therefore, a different method to connect velocity and vorticity is used for the three-dimensional case.

2.3.1 Analysis of Time-Space Invariant Characteristics of a Turbulent Velocity Field in Channel Flow

Cross correlation flow measurement is based on the fact that certain properties of the velocity field, in particular the integral (2.15), approximately preserve their value throughout space and time. Such flow characteristics, called space-time invariant characteristics, play a fundamental role in turbulence theory. A number of studies have been conducted on such characteristics for homogeneous isotropic turbulence and for special cases of turbulence such as Rayleigh-Benard Flow and others [61,87,91-93,95]. However, a quantitative understanding of the cross correlation flow measurement technology requires specific analysis, which have previously not been conducted.

The work conducted as part of this thesis, considered space-time invariant phenomena of a turbulent velocity field under the specific condition of an invariant vorticity field along flow stream lines, as is described by equation (2.14). In the author's opinion, such analysis, although conducted for a specific application, could be useful in general.

The following mathematical property relates vorticity to velocity [59].

$$\nabla \times \vec{\omega} = \nabla^2 \vec{u} \tag{2.23}$$

By expanding equation (2.23) for velocity and vorticity, using the variables presented in (2.13), applying equation (2.14), and looking at the spacial component perpendicular to the dominant direction of the flow, following equation is obtained.

$$\begin{aligned}
&\frac{\partial^2 v}{\partial \zeta^2} + \frac{\partial^2 v}{\partial \eta^2} + \frac{\partial^2 v}{\partial \tau^2} + \\
&+ (\frac{1}{U^2} + (\frac{\zeta}{U^2}\frac{\partial U}{\partial \eta})^2 + (\frac{\zeta}{U^2}\frac{\partial U}{\partial \tau})^2)\frac{\partial^2 v}{\partial \xi^2} + \\
&+ \frac{2}{U}\frac{\partial^2 v}{\partial \xi \partial \zeta} - \frac{2\zeta}{U^2}\frac{\partial U}{\partial \eta}\frac{\partial^2 v}{\partial \xi \partial \eta} - \frac{2\zeta}{U^2}\frac{\partial U}{\partial \tau}\frac{\partial^2 v}{\partial \xi \partial \tau} + \\
&+ (\frac{2\zeta}{U^3}(\frac{\partial U}{\partial \eta})^2 - \frac{\zeta}{U^2}\frac{\partial^2 U}{\partial \eta^2} + \frac{2\zeta}{U^3}(\frac{\partial U}{\partial \tau})^2 - \frac{\zeta}{U^2}\frac{\partial^2 U}{\partial \tau^2})\frac{\partial v}{\partial \xi} = \\
&= \frac{1}{U}\frac{\partial \omega_z}{\partial \xi} - \frac{\partial \omega_x}{\partial \tau} + \frac{\zeta}{U^2}\frac{\partial U}{\partial \tau}\frac{\partial \omega_x}{\partial \xi}
\end{aligned} \tag{2.24}$$

It should be noted, that in this section, and in all remaining sections of this thesis, the variables ζ, ξ, and η refer to the change of variables presented in (2.13). In equation (2.24), U and all components of ω are independent of ζ, although there are terms in equation (2.24) that are proportional to ζ or to the square of ζ. The assumption that the turbulent velocity field has time-space invariant properties similar to vorticity had been used in [45,46]. Equation (2.24) can be used to validate this assumption. If it is assumed that v is not dependent on ζ, then the terms of (2.24) with linear or quadratic

dependence on ζ must cancel each other out. One must note, though, that both quadratic instances of ζ in equation (2.24) are multiplied by squared partial derivatives of U and divided by quartic U. These terms are the only quadratic instances of ζ in equation (2.24), and they must both be positive, because they are taken to even powers. Therefore, for these terms to be equal zero, the partial derivatives of U with respect to η and τ must be equal to zero. Therefore, U must be independent of η and τ. Recalls, U is defined as being independent of x and time, which would imply that U is also independent of ζ and ξ. Since U is already defined as being independent of time and ζ, the additional independence of η and t would mean U must be a constant through space and time. Therefore, equation (2.24) demonstrates that v can be independent of ζ only if U is a constant through space and time.

Detail analysis of equations (2.24) is a subject of separate study and is not presented in this work, but even from very basic observations, it can be seen that the terms, which are responsible for dependence of v on ζ, are formed by products of ζ, and derivatives of U. Therefore, for a small enough domain in the x-direction, or for cases where the derivatives of U are small, the dependence of v on ζ is small. The region where v remains approximately invariant of ζ depends on the derivatives of U.

It is known experimentally that for the case of pipe flow, and for most turbulent flows, U is not constant, but despite this, the approximation that v is locally frozen is often made. It is therefore important to analyze under which conditions such approximations are appropriate. This will now be done, for the case of pipe flow.

2.4 Space-Time Invariant Properties of the Integral Characteristics of Turbulent Velocity in Pipe Flow

For the case of pipe flow, equation (2.23) may be integrated over the pipe cross section area, resulting in the following relation.

$$\int_{-\pi}^{\pi}\int_{0}^{R} \nabla \times \vec{\omega} r dr d\theta = \int_{-\pi}^{\pi}\int_{0}^{R} \nabla^2 \vec{u} r dr d\theta \tag{2.25}$$

By expanding equation (2.25) in cylindrical coordinates, and applying the no-slip condition, one obtains the following relation.

$$\int_{-\pi}^{\pi}\int_{0}^{R} (\frac{\partial^2 v}{\partial z^2} - \frac{\partial \omega_\theta}{\partial z}) r dr d\theta = 0 \tag{2.26}$$

One possible solution to equation (2.26) is the term inside the integral being equal to zero, resulting in the following relation.

$$\frac{\partial^2 v}{\partial z^2} - \frac{\partial \omega_\theta}{\partial z} = 0 \tag{2.27}$$

Consider a turbulent pipe flow with vorticity field ω_θ and velocity field v at a particular moment in time. These fields must satisfy equation (2.26). Consider another velocity field $\hat{v}$ that satisfies the equation

$$\frac{\partial^2 \hat{v}}{\partial z^2} - \frac{\partial \omega_\theta}{\partial z} = 0 \tag{2.28}$$

The fields ω_θ and $\hat{v}$ will also then satisfy equation (2.26). Since ω_θ is independent of ζ, $\hat{v}$ can also be defined to be independent of ζ while satisfying equation (2.28), and hence will also satisfy equation (2.26) where $\hat{v}$ replaces v. This relation is demonstrated in equation (2.29).

$$\int_{-\pi}^{\pi}\int_{0}^{R}\frac{\partial^2\hat{v}}{\partial z^2}rdrd\theta = \int_{-\pi}^{\pi}\int_{0}^{R}\frac{\partial^2 v}{\partial z^2}rdrd\theta$$

$$where \tag{2.29}$$

$$\frac{\partial\hat{v}}{\partial\zeta} = 0$$

Although the time evolution of v depends on ζ, and the time evolution of $\hat{v}$ does not depend on ζ, and v and $\hat{v}$ may not be equal at any points in time, the integral over the pipe cross-section area of the double z partial derivative of v and $\hat{v}$, will be equal for all time, since both velocity fields satisfy equation (2.26) with the same vorticity field ω. Recall, if a field is independent of ζ, it is called locally frozen. Therefore, although the locally frozen velocity approximation does not typically predict the space-time development of a turbulent velocity field, a surrogate locally frozen turbulent velocity field can be used to predict the space-time development of the integral shown in equation (2.26), and hence equation (2.29) is true.

Integrating equation (2.29) twice over z, gives the following equation:

$$\int_{-\pi}^{\pi}\int_{0}^{R}\hat{v}rdrd\theta = \int_{-\pi}^{\pi}\int_{0}^{R}vrdrd\theta + K_1 z + K_2 \tag{2.30}$$

K_1 can be set to zero because it is reasonable to assume that integral properties of turbulence do not have a linear dependence on location along the pipe. K_2 can also be set to zero, because any added constant K_2 can be redefined as part of the surrogate velocity field $\hat{v}$. One may therefore assume the following relation holds:

$$\int_{-\pi}^{\pi}\int_{0}^{R} \hat{v} r dr d\theta = \int_{-\pi}^{\pi}\int_{0}^{R} v r dr d\theta \tag{2.31}$$

Since v is the turbulent velocity, its dependence on r is chaotic. If v is represented as a sum of sinusoidal functions, set to zero at the pipe walls as according to the no slip condition, it can be shown that if (2.31) describes turbulent pipe flow, it is reasonable to approximate that the following equation describes turbulent pipe flow as well:

$$\int_{-\pi}^{\pi}\int_{0}^{R} \hat{v} dr d\theta = \int_{-\pi}^{\pi}\int_{0}^{R} v dr d\theta \tag{2.32}$$

Therefore, a surrogate velocity field that follows the locally frozen turbulence approximation, may not evolve in the way an actual turbulent velocity field would evolve, but the double radial-angular integral of the surrogate velocity field will evolve in the way the double radial-angular integral of the actual velocity field will evolve. Hence a locally frozen turbulent velocity field might not describe the space-time development of the actual velocity field, but it will describe the space-time development of the double radial-angular integral of the actual velocity field.

2.5 Discussion on Theoretical Analysis

The theoretical analysis conducted as part of this work has achieved the following results and conclusions.

1. Operation of the cross correlation flow meter is based on the fact that certain characteristics of the turbulent velocity field remain invariant while moving along a pipe, with an average axial flow velocity, which we call *measured velocity* V_m. To understand how measured velocity V_m is related to flow characteristics, such as time-averaged velocity components and turbulence, theoretical analysis has been conducted by the author.

2. It was shown that in typical turbulent pipe flow, the vorticity field can be described by using the *Locally Frozen Turbulence Approximation*, which means that vorticity is transported by time-averaged velocity components. Estimations show that this approximation is valid on a long distance along the pipe, but eventually becomes invalidated due to neglected terms representing the change of the axial flow profile along the direction of the flow, which become important for larger domains representing longer pipe runs.

3. Analysis of simplified two dimensional turbulent flow in an infinite plane allows for an analytical solution, which relates the vorticity field with an integral characteristic of the velocity field along a straight line segment located at a certain position within the flow. This integral characteristic is analogous to the demodulated signal detected by the cross correlation flow meter, as seen in equation (2.15). From this analysis, it becomes clear that the demodulated signal, as a function of time and position, does not remain constant moving along the pipe. The reason for this, is the deformation of the vorticity field by the time-averaged velocity components. However, on a short distance, the vorticity field and the demodulated signal remain almost constant while moving along the flow. This distance can be calculated, and it depends

on turbulent scales and time-averaged velocity gradients.

4. General analysis of the relation between velocity and vorticity for three-dimensional flow have been conducted in Section 2.3. It was shown that the Local Frozen Turbulence Approximation for vorticity does not imply a similar approximation for turbulent velocity, unless the time-averaged velocity component in the dominant flow direction is constant in all space and time. However, the locally frozen turbulent velocity approximation can be applied over a short distance along the flow direction.

5. In application to cross correlation flow measurement, it was shown that in pipe flow, a simple relation between the integral characteristics of the vorticity field and velocity field can be obtained. The double radial-angular integral of vorticity, at a given cross-section of a pipe, depends on position along the pipe and on time, and does not have space-time invariant properties even if vorticity is described by the Locally Frozen Turbulence Approximation. The same is valid for the velocity field. However, the Local Frozen Velocity Approximation allows for correct prediction of the space-time development of the double radial-angular integral of radial turbulent velocity. This result is used in the next chapter, in order to develop a mathematical model which allows simulation of cross correlation flow measurement under different flow conditions and design parameters.

6. Equation (2.14) for vorticity transport using the Local Frozen Turbulence Approximation, and variables (2.13), use the assumption that time-averaged radial and angular velocity components are negligibly small compared with the time averaged axial velocity component U. Therefore, all analysis following these equations uses this assumption. Cases with strong radial and angular velocity components, such as cases with significant swirl, are not considered in this work. However, the

presented analysis can be extended on such flow if variables (2.13) include other velocity components. This would also result in the same equation (2.14), but the vorticity will remain invariant along curved (not straight) streamlines. Also, for the case of negligible swirl, a surrogate locally frozen turbulent velocity field can be used to predict the space-time development of the demodulated signal.

The next chapter describes synthetic turbulence simulations developed by the author, based on the hypothesis that a surrogate velocity field generating a demodulated signal with the same average power spectrum as the demodulated signals of the real flow, is sufficient for studying the space-times development of the demodulated signal, when applying a locally frozen radial turbulent velocity approximation.

Chapter 3

Numerical Simulations

Cross correlation flow measurement is based on detecting certain integral characteristics of the turbulent velocity field at two pipe cross sections, separated by a distance of order magnitude of the pipe diameter. The theoretical analysis developed in this work, allows for calculation of these integral characteristics at both cross sections, if the angular-averaged turbulent velocity field and the time-averaged velocity distribution at one of the cross sections is known. Therefore, in order to implement these theoretical results into a mathematical model, an initial turbulent velocity field must be obtained or generated, and an algorithm calculating the evolution of this field along a pipe must be developed.

This chapter describes a method of numerical simulation of turbulent flow, developed as part of the work conducted for this thesis, in order to implement the theoretical result described in the previous chapter, into a mathematical model. There are four main sections in this chapter. The first section is a review of computational fluid dynamics methods, and the benefits and drawbacks of different methods. The second section discusses the conditions that the generated turbulent velocity field must meet. The third section describes the original synthetic turbulence simulation method for generating a turbulence velocity field, and how it allows the user to simulate various flow conditions. The fourth section describes the simulation algorithm, demonstrating the process of both simulation of the evolution of

a velocity field, and simulation of cross correlation flow measurement, allowing the user to analyze flow measurement dependence on flow condition.

3.1 Computational Fluid Dynamics

For a non-compressible fluid, and no external forces, flow is governed by the Navier-Stokes equations, given below.

$$\frac{d\vec{u}}{dt} + (\vec{u} \cdot \nabla)\vec{u} = -\frac{1}{\rho}\nabla p + \nu\nabla^2\vec{u} \tag{3.1}$$

$$\nabla \cdot \vec{u} = 0 \tag{3.2}$$

where $\vec{u} = \vec{u}(u, v, w)$, and u, v, and w are the x, y, and z components of flow velocity respectively, p is pressure, ρ is density, and ν is kinematic viscosity. By assigning initial conditions of a fluid system, the Navier-Stokes equations give the solution for how that system will evolve through time and space.

When solving for the behavior of time-dependent turbulent structures, small differences in the initial conditions could result in significant differences in the solution. Therefore, solving such problems requires very fine space and time resolution. In order to reproduce turbulence, the space and time resolution of the numerical algorithm should be of order of magnitude smaller than the space and time scales of the turbulent motion in the flow. The higher the Reynolds Number, the smaller the turbulence scales. For typical industrial flow, Reynolds Numbers are quite high, of order of $10^6 - 10^7$. For these reasons, modeling turbulent flow is a very difficult mathematical problem. Even if using the most powerful computers available today,

the Navier-Stokes equations can not be solved directly for the majority of industrial applications within practical time frames. Rather than solving the equations directly, different types of approximation models are used.

Reynolds Averaged Navier-Stokes (RANS) simulations are based on taking the time average of every term in the Navier-Stokes equations. The effects of time dependent structures are modeled prior to solving the system of equations, and the equations are solved to determine time-averaged behavior. Solving the time-averaged Navier-Stokes equations, called the Reynolds Equations, requires additional models to close the system. Since RANS simulations are not capable of describing cross correlation flow measurement, because they not model turbulent structures, since turbulent structures are time-dependent. [52].

Direct Numerical Simulation (DNS) models solve the Navier-Stokes equations directly [52,53,61,75,79,80]. Such computations require an impractical amount of time and computer power for most applications of computational fluid dynamics, including the modeling of cross correlation flow measurement. DNS is typically used to solve problems set in small computational domains and with small Reynolds numbers. The Reynolds numbers typically seen in industrial settings are at least a few hundred thousand. Using DNS models to solve for flow conditions with such Reynolds number is not practical.

LES is a combination of RANS and DNS [71-77,84]. Using LES, turbulent structures are separated into large and small scales, based on the Kolmogorov turbulence scales. Temporal and spacial averaged affects of small scale turbulent structures are modeled, and the behavior of larger scale turbulent structures is calculated. LES modeling can be conducted for larger Reynolds numbers in much more reasonable time frames than DNS modeling. Therefore, LES is useful for more applications.

Initially in this work, the modeling of cross correlation flow measurement using LES was perused. In order to conduct such modeling, it is necessary to assign an initial turbulent velocity field. However, if an initial turbulent

velocity field is assigned, the development of turbulent structures between upstream and downstream ultrasonic beams can be described using results of the theoretical analysis presented in the previous chapter. The theoretical results described in the previous chapter allow the modeling of cross correlation flow measurement to be conducted using much simpler calculations than what is required by LES, and hence allow the modeling to be conducted in more practical time frames and without requiring significant computer power. Thus, it was decided to model cross correlation flow measurement based on the results of the previous chapter, rather than with LES.

Synthetic Turbulence simulation, compared to RANS, DNS, and LES, is a unique approach to turbulence modeling, and can be conducted in very reasonable time frames [83-85]. Artificial turbulent structures are generated, and their space time evolution is calculated based on a flow model. The artificial structures are typically mathematical structures based on random sequences or sinusoidal functions. The flow model used to calculate the evolution of these structures can be DNS, LES, RANS, or a simpler model such as a Frozen Turbulence Approximation. The synthetic turbulence is created such that it has the statistical properties that the modeled flow condition would have. Therefore, rather than modeling the exact turbulent structures that would appear within a given flow, synthetic turbulence models how artificial turbulent structures would evolve within a given flow. If the flow model used to evolve the synthetic turbulence is a RANS model or a Frozen Turbulence approximation, a flow simulation can be conducted in reasonable time frames, even if using personal computers and simulating high Reynolds Number flows.

Synthetic Turbulence simulation is ideal for modeling cross correlation flow measurement for the purposes of the work conducted for this thesis. Cross correlation flow measurement does not depend on individual turbulent eddies, but on the development of a signature of an ensemble of many turbulence structures. Therefore, modeling the exact turbulent structures present in a flow is not necessary for modeling cross correlation flow measurement. Since the turbulent structures between upstream and downstream

beams are continuously changing, and a flow measurement is conducted every few seconds, and an ensemble of many flow measurements is averaged to deduce the flow rate, the time-averaged flow conditions are sufficient to model cross correlation flow measurement dependence on the evolution of turbulent structures. Therefore, time averaging based flow models, such as RANS or the Frozen Turbulence approximation, can be used to predict the time-evolution of synthetic turbulent properties between the upstream and downstream beams.

The affect of different turbulent conditions on cross correlation flow measurement, can be very efficiently studied using Synthetic Turbulence, by conducting various simulations where the generated synthetic turbulence has realistic average statistical properties corresponding to different flow conditions. In previous attempts to model cross correlation flow measurement, a method such as this has never been used. In the opinion of the author, this is the most efficient method of conducting such a study, given today's level of technology.

3.2 Requirements for Generating a Turbulent Velocity Field

It was deduced in chapter 2, that the space-time evolution of the double radial-angular integral of a radial turbulent velocity field, may be calculated by applying the Locally Frozen Turbulence Approximation to the velocity field. This holds true even if the Locally Frozen Turbulence Approximation does not calculate the space-time evolution of the real velocity field.

According to this theory, if the time and angularly averaged axial flow profile is known, and a synthetic radial turbulent velocity field can be generated based on time averaged properties representative of a particular flow condition, the space-time evolution of the double radial-angular integral of that velocity field can be calculated. Recall, that the demodulated signal col-

lected by the cross correlation flow meter is proportional to the radial integral of the radial turbulent velocity field. If many cross correlation flow meters are installed at the same location along a pipe, but with different angular orientations, their summed demodulated signal represents a double angular-radial integral of the radial turbulent velocity field. By defining a generated turbulent velocity field as being the angular averaged radial turbulent velocity field, as a function of time and location along the pipe diameter, evolving it along a pipe using the locally frozen turbulence approximation, and integrating it along the pipe diameter at desired cross sections, the demodulated signal obtained by the cross correlation flow meter can be numerically simulated. By generating synthetic angular averaged radial turbulent velocity fields representative of different flow conditions, one can simulate cross correlation flow meter behavior at different flow conditions.

In order to conduct such numerical simulations, the time-averaged axial flow profile must be known, and the synthetic turbulence field must be generated based on a time-averaged property representative of the turbulence at the flow condition for which simulation is desired. The time-averaged axial flow profile can be obtained through RANS simulation, or literature on common flow conditions. The time-average turbulent power spectrum is a property representative of the turbulence at a given flow condition. The time-averaged power spectrum of the demodulated signal collected by the cross correlation flow meter is the time-averaged power spectrum of the integral of turbulent velocity, and is therefore also representative of the turbulence at the flow condition at the location of measurement. Since the time-averaged power spectrum of the demodulated signal can be obtained using the cross correlation flow meter, this method can be used to obtain time-averaged properties of turbulence for the numerical simulations. Turbulent power spectrum can also be obtained from literature.

3.2.1 Signal Power Spectrum as Input for the Simulation

The power spectrum of the demodulated signal at the location of measurement is mathematical information gathered from the flow meter that can inform an observer of the flow condition at the location of measurement, and particularly how the flow condition affects turbulent structures. Hence, to simulate cross correlation flow measurement for various flow conditions using synthetic turbulence, a demodulated signal power spectrum representative of the flow condition can be used to generate an initial synthetic radial turbulent velocity field. The power spectrum of the demodulated signal is defined by the following formula.

$$S(x, \omega) = |F(\phi(x, t))| \tag{3.3}$$

where F represents the Fourier Transform operator, ϕ is the demodulated signal as a function of time t and pipe cross section location x, ω represents frequency, and the straight brackets are absolute values brackets. The resulting spectrum, a function of ω, is dependent on the location x along the pipe, but it is observed experimentally that the power spectrum of the demodulated signal does not change significantly between the upstream and downstream locations involved in flow measurement, which are of order one pipe diameter apart.

A single measurement typically records a demodulated signal a few seconds long. The power spectrum of a four second demodulated signal would not be an accurate representation of the time-averaged turbulent conditions at the measurement location, due to the predominance of frequencies of instantaneous non-regular effects. Averaging the power spectrum of many demodulated signals would smooth out irregularities, resulting in time-averaged properties remaining. Figure 3.1 shows a power spectrum of a single four second demodulate signal, and the average power spectrum of 100 four second

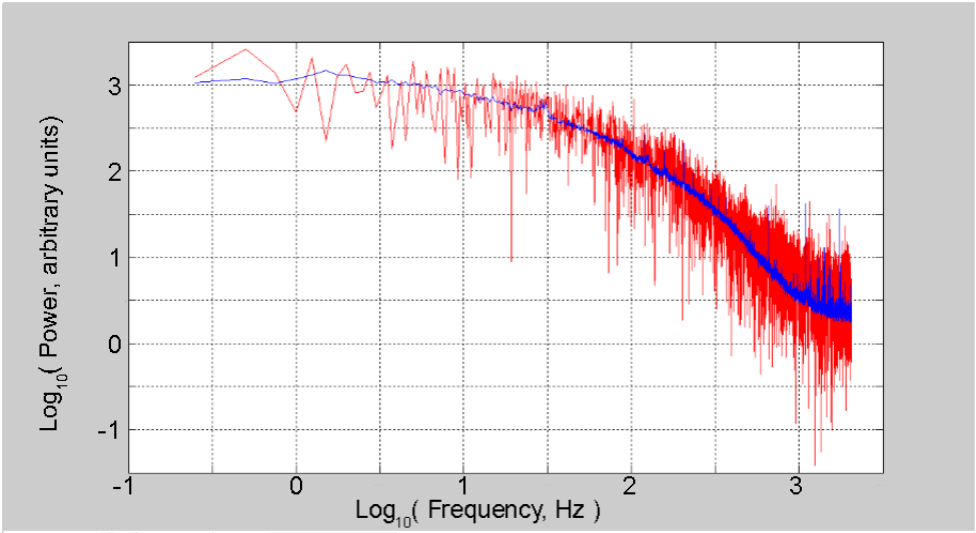

Figure 3.1: Demodulated signal power spectrum, on a base 10 logarithmic scale for both x-axis and y-axis. Red represents the power spectrum from a single 4-second demodulated signal. Blue is the average power spectrum of 100 4-second demodulated signals collected at the same location during the same set of measurements and same flow condition.

demodulated signals from the same flow condition. These power spectrum are obtained by first normalizing every four second demodulated signal to its root-mean-square, and then taking the absolute value of the Fast Fourier Transform of demodulated signals collected by the cross correlation flow meter in the AMAG Laboratory. Demodulated signals must be normalized, because their amplitude may differ depending on the carrier frequency used to obtain the signal.

The process of averaging the power spectrum from many single measurements smoothens out temporary properties present during a single measurement but not generally present at the given flow condition, and reveals properties present in the given flow condition that may not appear when looking at the power spectrum of a single measurement. Such an effect is the bump near 31Hz near the 1.5 location on the x-axis in Figure 3.2, which is shown in the average power spectrum, but not in the power spectrum of a single measurement.

This method was applied when conducting the simulations of cross correlation flow measurement for this work. In order to simulate cross correlation flow measurement for a particular flow condition where a cross correlation flow meter may be installed, data was collected at that location, and the collected demodulated signals were used to create an average power spectrum. This power spectrum is then used, along with other inputs, to generate an initial synthetic radial turbulent velocity field as a function of time and location along the pipe diameter. The field is generated such the its integral along the pipe diameter yields the same power spectrum as the average power spectrum seen in real flow. Such a field is not unique, and should not be, since in real flow, the turbulent velocity field is different every moment in time due to the chaotic nature of turbulence, but the average statistical properties, such as power spectrum, remain the same.

This method is one of many options of defining a power spectrum for the simulation. It was chosen for this work, to compare simulated flow measurement results to results of laboratory testing. In the general case, any power spectrum may be used as input for the simulation method developed in this work.

3.3 Synthetic Turbulence Equation

The equation used to simulate a turbulent radial velocity field is given below. This equation was developed by the author as part of the work conducted for this thesis.

$$v(y,t) = \sum_{j=0}^{m} k_j C_j(y)(\cos(\theta_j(y))\cos(\omega_j t) + \sin(\theta_j(y))\sin(\omega_j t)) \tag{3.4}$$

where

$$\theta_0(y) = 0$$

$$\theta_{j+1}(y) = \pi \sin(\frac{\pi y j}{p N_y} + q_j) \tag{3.5}$$

The turbulence is represented as a sum of sine and cosine functions. The resultant field, a function of time t and location along the diameter y, is a sum along all time harmonics j, corresponding to frequency ω_j, of the turbulent structures. The multiplier k_j ensures that the power spectrum of the simulated demodulated signal is equal to the desired spectrum. The k_j values are typically not user specified, and are deduced by the simulation program based on user specified demodulated signals. The $C_j(y)$ function define radial turbulent spectrum distribution, allowing for user control of the axial scale of turbulence. The function $\theta_j(y)$ defines the space correlation in the radial direction, allowing for user control of the radial scale of turbulent structures.

Within $\theta_j(y)$, the factor p controls the level of correlation between velocity values along the pipe diameter. N_y is the number of spacial cells along the pipe diameter within the simulation. The phase shift q_j is a random value between $-\pi$ and π, assigning a random phase shift to every harmonic through time.

The purpose of every factor in these equations will be explained in more detail, with examples given to show how each factor acts as a control parameter for the properties of the simulated velocity field. In section 3.4, the algorithm used to develop the flow velocity field based on the specifications presented in this section, simulated the space-time evolution of this field, and simulate cross correlation flow measurement, will be explained.

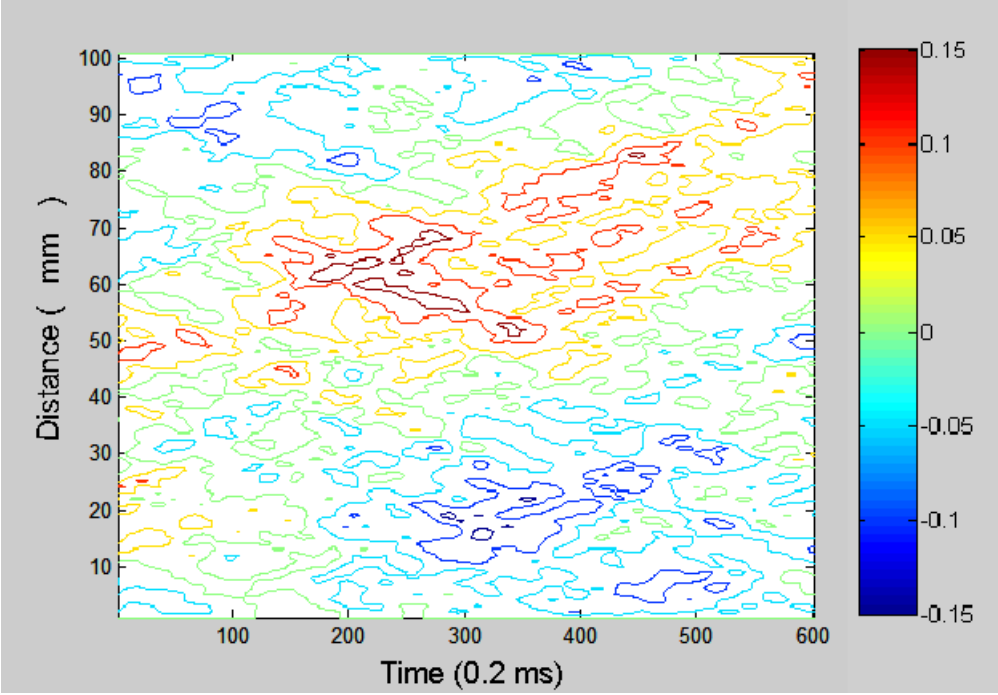

Figure 3.2: Simulated radial turbulent fluctuations velocity in meters per second, as a function of time and location along the diameter. Time is along the horizontal axis, covering a span of 120 milliseconds. Location along the diameter is along the vertical axis, covering the entire diameter's length of 0.1 meters. The portion of the simulated velocity field shown is a small portion of the entire simulation, which spans 4 seconds.

3.3.1 Control Parameters of the Velocity Field and Factors in the Velocity Field Equation

Figure 3.2 shows the level curves of a radial turbulent velocity field generated by equation (3.4). Time is on the horizontal axis and location along the pipe diameter is on the vertical axis. The colours indicate radial fluid velocity from approximately -0.15m/s to 0.15m/s, with blue being lower velocity and red being higher velocity. The portion of the time domain shown in Figure 3.3 spans over 0.12 seconds, although Figure 3.2 shows part of a simulation that spans 4 seconds. The diameter length is 0.1 meters. The 0.021 second span is from 1.96 seconds to 2.08 seconds of the 4 second simulation.

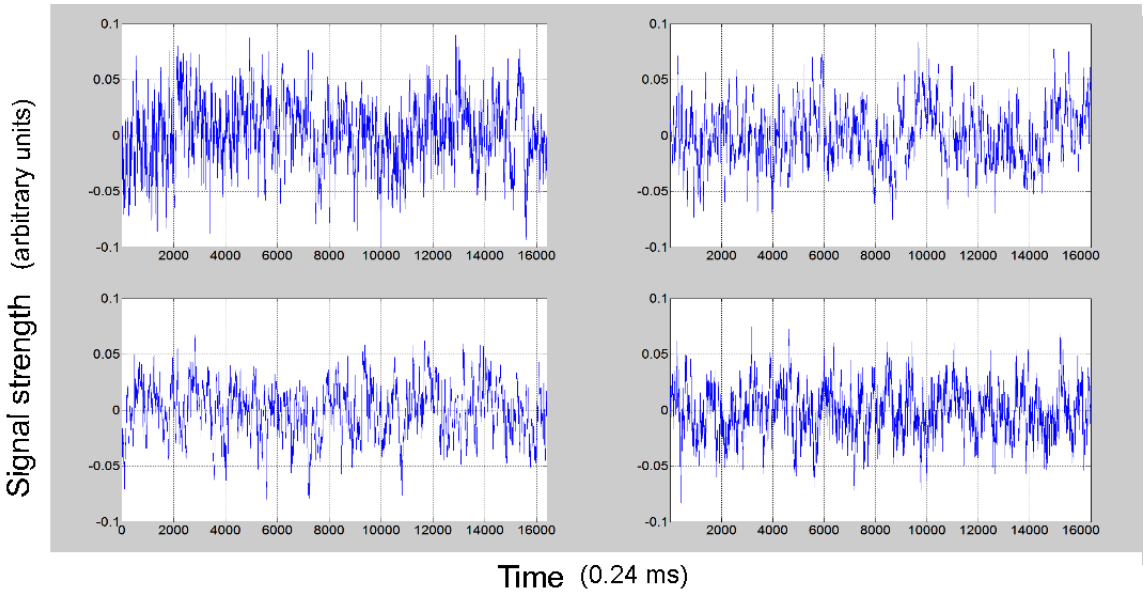

Figure 3.3: Four, of the one hundred, demodulated signals collected to create an average power spectrum to define the flow condition used to simulate flow.

The velocity field used in Figure 3.2 was created using the power spectrum show in blue in Figure 3.1. The power spectrum, as mentioned above, is the average power spectrum of 100 four-second long collected demodulated signals. Four of these signals are shown in Figure 3.3. The x-axis covers a 4 second span in 1/4096 second intervals, because a sampling frequency of 4096Hz was used during data collection.

Every demodulated signals in the set of 100 are different signals, but with similar spectral properties. The red power spectrum in Figure 3.1 is the power spectrum of the first of the four demodulated signals shown in Figure 3.3. The rest of the 100 demodulated signals have a similar looking power spectrum, with wide chaotic spread around a distinct curve. When all 100 power spectrum are averaged, the result is the blue power spectrum in Figure 3.1, showing just a well defined curve without a wide chaotic spread.

The simulated radial turbulent velocity, shown in Figure 3.2, can be integrated along the diameter to produce a simulated demodulated signal. The

simulated demodulated signal will not be equal to any of the 100 signals used to produce the average power spectrum that was used to produce the velocity field, but the simulated demodulated signal will have the same power spectrum as the average power spectrum produced by the 100 demodulated signals. Figure 3.4 shows the simulated demodulated signal, as a function of time, derived from integrating the simulated velocity field shown in Figure 3.2 along the pipe diameter. Figure 3.4 shows the entire time span of 4 seconds, rather than just the 21 milliseconds shown in Figure 3.2. The 4 second time span in Figure 3.4 has a resolution of 0.00002 seconds. Such a resolution is chosen for simulating the velocity field, in order to observe measured velocity dependence on measurement settings such as transducer spacing. More detail on simulation parameters, such as time resolution, is given in Section 4 of this chapter.

The y-axis magnitude in Figure 3.4 is much larger than the y-axis magnitudes given in Figure 3.3. This is because the radial turbulent velocity field is scaled, by a factor dependent on a user specified axial flow velocity profile, in order to give the turbulent radial velocity field a realistic magnitude. Basing the magnitude of the turbulent velocity field on demodulated signal magnitude is not correct, because the demodulated signal magnitude depends on the carrier frequency of the ultrasonic beam used to collect the demodulated signal.

The power spectrum of the simulated demodulated signal, obtained from the simulated velocity field, is shown in Figure 3.5 in red, along with the average power spectrum of the 100 demodulated signals used to generate the simulated velocity field shown in blue. The magnitude is different due to the scaling factor applied to the simulated velocity field after simulation, but the shapes of the two power spectrum are identical, up to a particular frequency. Figure 3.6 shows the power spectrum of the simulated demodulated signal in red with the scaling factor removed, along with the average power spectrum of the 100 demodulated signals used to generate the simulated velocity field shown in blue. One can then see that the shapes of the two power spectrum are identical up to a particular frequency.

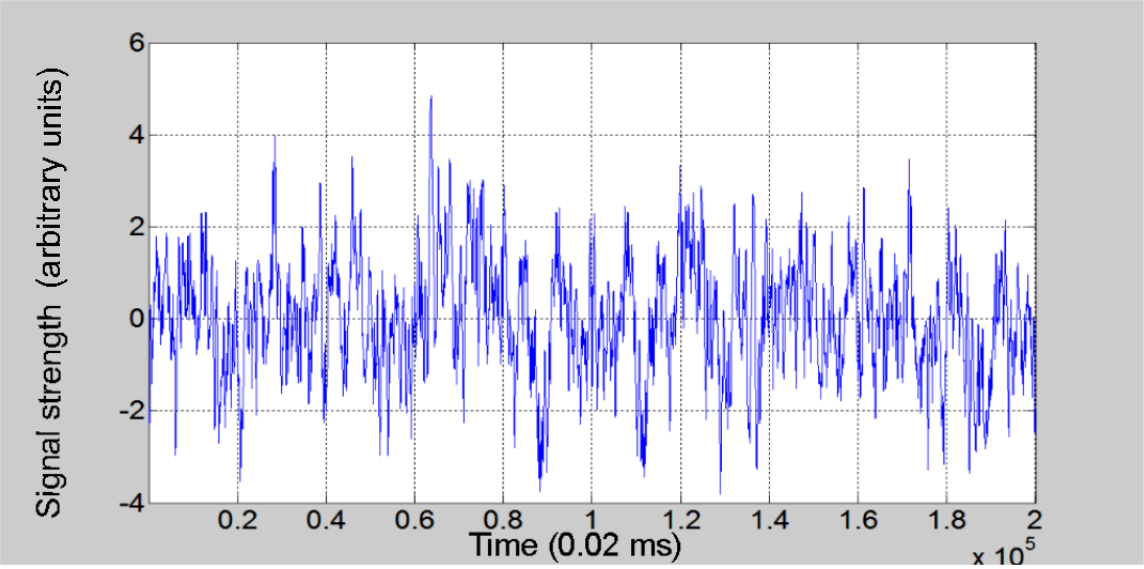

Figure 3.4: Simulated demodulated signal, obtained by integrating simulated radial turbulent fluctuations velocity field over pipe diameter. The horizontal axis spans 4 seconds.

The reason the magnitude of the simulated power spectrum drops after a particular frequency, is because the simulation is designed to not simulate turbulent structures with frequency higher than a user specified value. This is done in order to save computing time by not simulating turbulent structures that have negligible effect on flow measurement. Simulating smaller structures has negligible effect because the cross correlation flow meters used as a part of this work detect turbulent fluctuations of up to approximately 200 Hz. Although the power spectrums of the collected demodulated signals extend to beyond 200Hz, the validity of the information provided by the power spectrums beyond this point is still a matter of study, and low pass filters are typically set at values much lower than 200Hz during cross correlation flow measurement. Such low pass filters were used during this work as well. It was also observed, through conducting cross correlation flow measurement with different low pass filters, that extending the low pass filter beyond 200Hz has negligible effect. More information about this is given below, and in Section 4 of this chapter.

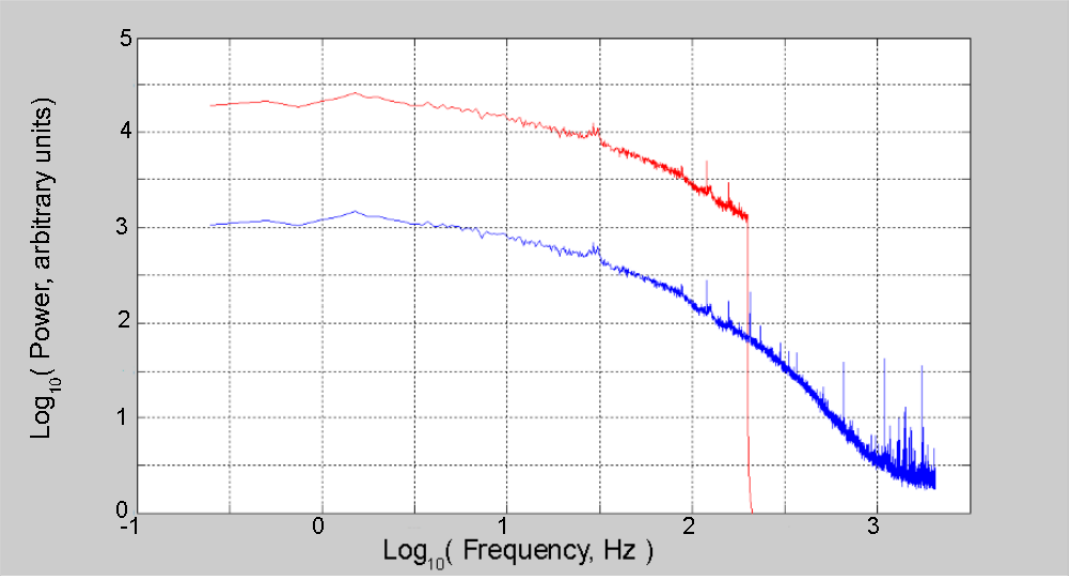

Figure 3.5: The power spectrum of the simulated demodulated signal, obtained from the simulated velocity field, is shown in red. The average power spectrum of the 100 demodulated signals used to generate the simulated velocity field shown in blue. Both axis scales are base 10 logarithmic, with the frequency in Hz on the horizontal axis. The two power spectrum are of same shape, but different magnitude, because a scaling factor is applied to the simulated demodulated signal in order to remove magnitude affecting effects of carrier frequency.

The Factor k

In the process of simulating the velocity field, the factor k_j from equation (3.9) is responsible for ensuring that the diameter-integral of the simulated velocity field creates a simulated demodulated signal with the same power spectrum as the average power spectrum of the demodulated signals used to simulated the velocity field. In the simulation process, all aspects of equation (3.9) are defined or calculated prior to the calculation of k_j. The factor k_j is the final step in the simulation, insuring that the simulated demodulated signal has the desired power spectrum. The factor k_j is automatically deter-

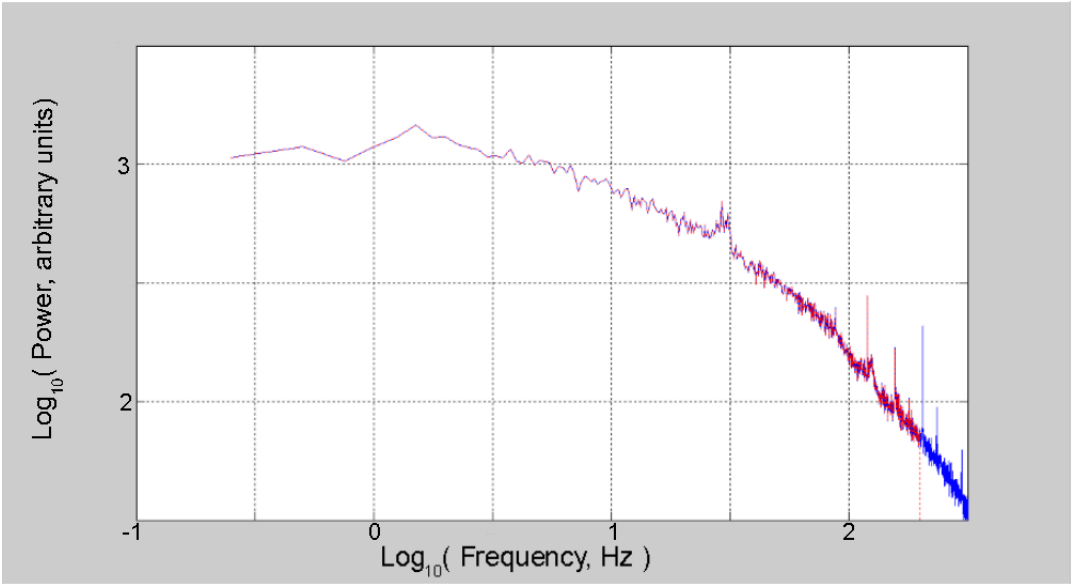

Figure 3.6: The power spectrum of the simulated demodulated signal in red with the scaling factor removed, along with the average power spectrum of the 100 demodulated signals used to generate the simulated velocity field shown in blue. Both axis scales are base 10 logarithmic, with the frequency in Hz on the horizontal axis.

mined by the simulation program, without user input. If the factor k_j were to not exist, in other words, if k_j were equal to 1 for all j values, the simulated velocity field would not represent the turbulent conditions in the pipe when the demodulated signal used to conduct the simulation was collected.

Figure 3.7 shows contours of a portion of a simulated velocity field, while Figure 3.8 shows the contour of the same portion of a velocity field simulated with exactly identical parameters except in the simulation shown in 3.8 k_j equals 1 for all j values. The colours indicate radial turbulent velocity from approximately -0.15m/s to 0.15m/s, with blue being lower velocity and red being higher velocity. The portion of the time domain shown in Figure 3.7 and Figure 3.8 spans 0.12 seconds, although Figure 3.7 and Figure 3.8 show a part of simulations that span 4 seconds each. The diameter length is 0.1 meters. The 0.12 second span is from 2.88 seconds to 3 seconds of the 4 second simulation.

Figure 3.9 shows the power spectrum of a regular simulation, with regularly defined k_j values, in red. The red power spectrum is taken from the same simulation used to produce Figure 3.7. Figure 3.9 shows in blue, the power spectrum of a simulation with the exact same parameters, except the simulation the blue power spectrum is taken from has k_j equal to 1 for all j values. The blue power spectrum is taken from the same simulation used to produce Figure 3.8. The power spectrum of the demodulated signals collected from the pipe in order to conduct both simulations is also shown in black in Figure 3.9. It is clear that the use of the k_j multiplier results in a simulation more representative of the power spectrum the simulation is attempting to replicate.

The simulated demodulated signals, with and without k_j equal to 1 for all j values, shows the greatest difference. This can be seen in Figure 3.10, where the blue curve is the regularly simulated demodulated signal, and the red curve is the simulated demodulated signal from an identical simulation, but with k_j equal to 1 for all j values.

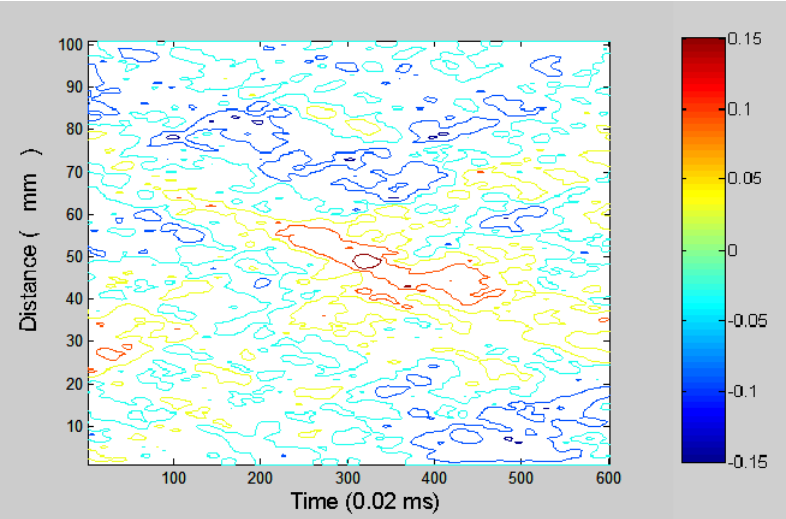

Figure 3.7: Simulated radial turbulent fluctuations velocity in meters per second, as a function of time and location along the diameter. Time is along the horizontal axis, covering a span of 120 milliseconds. Location along the diameter is along the vertical axis, covering the entire diameter's length of 0.1 meters. The portion of the simulated velocity field shown is a small portion of the entire simulation which spans 4 seconds.

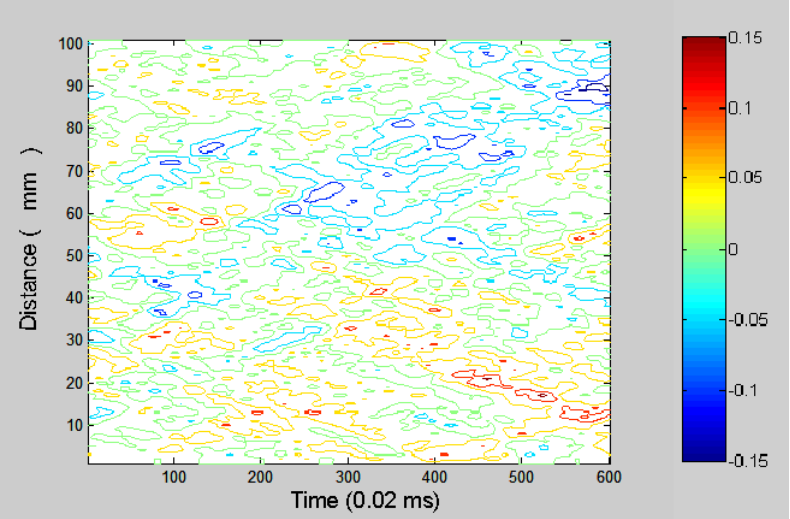

Figure 3.8: The contours in Figure 3.8 are the results of a simulation with the exact same parameters are the simulation from which the contours in Figure 3.7 were taken, except the simulation in Figure 3.8 has k equal to 1 for all j values.

High Pass and Low Pass Filters

High pass and low pass filters may be applied to the demodulated signal's power spectrum by the user, in order to only consider simulation of eddies of a particular range of frequencies. A high pass filter is a lower limit of the allowed frequencies, and a low pass filter is an upper limit of the allowed frequencies. Figure 3.11 shows the unfiltered power spectrum of a demodulated signal, and a filtered power spectrum of the same demodulated signal with a high pass filter of 12 Hz and a low pass filter of 50 Hz. Figure 3.12 shows the same information using logarithmic scales. A simple top hat filter is used.

Since cross correlation flow measurement measures the transport velocity of turbulent structures, high-pass and low-pass filters are applied to demodulated signals of measurements in order to focus velocity measurement on the transport velocity of eddies within a particular frequency range. By focusing on eddies of a particular frequency, one may obtain higher quality cross correlation curves.

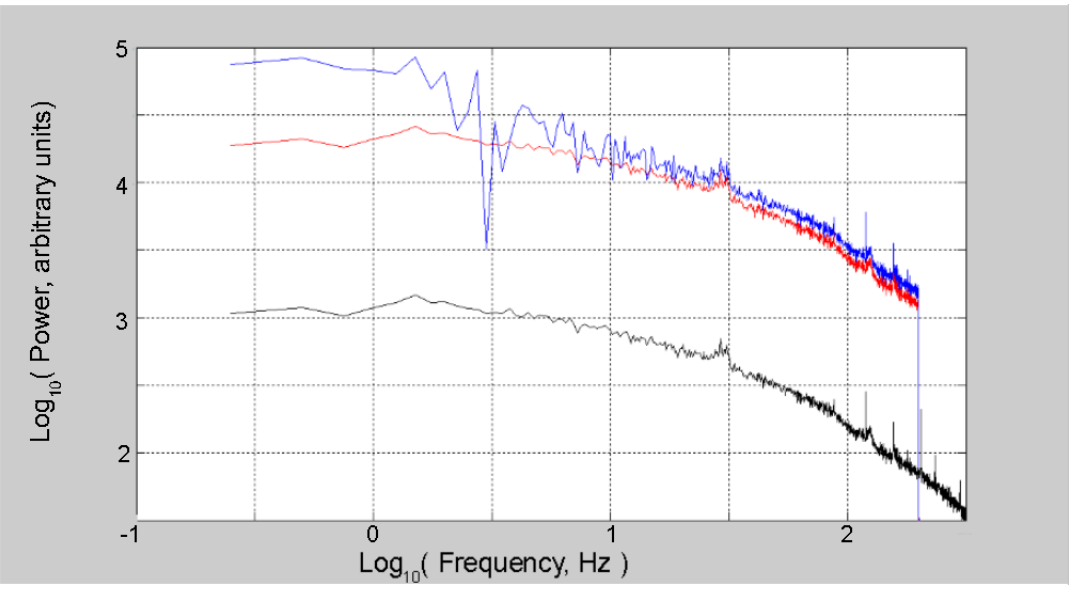

Figure 3.9: Power spectrum of real demodulated signal shown in black. Power spectrum of regularly simulated demodulated signal shown in red. Power spectrum of simulated demodulated signal of simulation same as that or red curve, but with k equal to 1 for all j values is shown in blue. Both axis use base 10 logarithmic scales, with frequency on the horizontal axis.

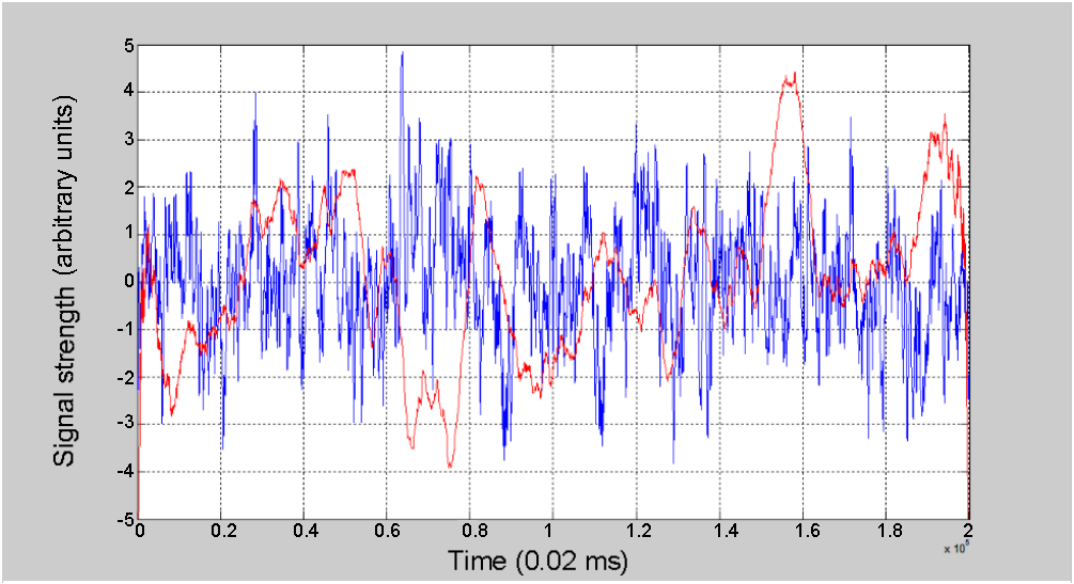

Figure 3.10: Blue curve is the regularly simulated demodulated signal. Red curve is the simulated demodulated signal from an identical simulation, but with k equal to 1 for all j values.

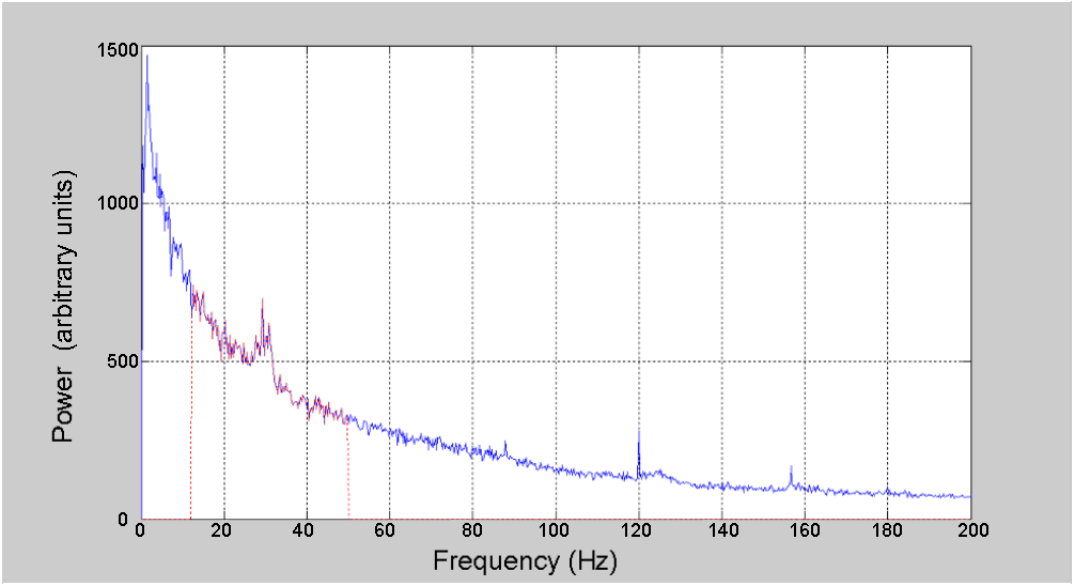

Figure 3.11: Filtered spectrum shown in red. Original spectrum shown in blue.

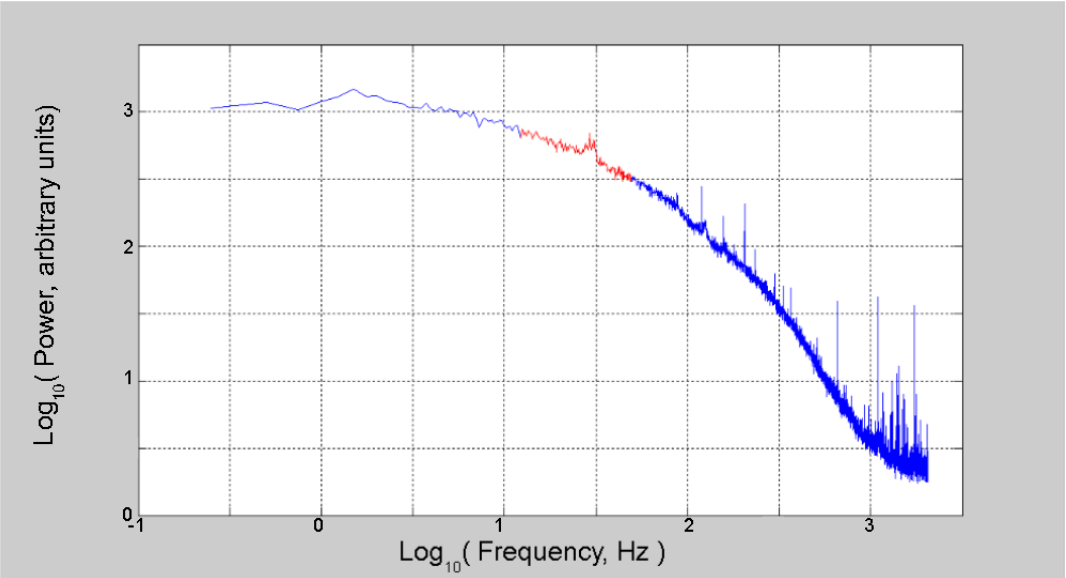

Figure 3.12: Filtered spectrum shown in red. Original spectrum shown in blue. Base 10 logarithmic scales used.

When conducting cross correlation flow measurements, high-pass and low-pass filters are applied to the collected demodulated signals prior to cross correlation. In the simulations discussed in this chapter, high-pass and low-pass filters are applied to the demodulated signal used for simulating the velocity field, prior to simulation. As a result, the simulated velocity field will be composed only of turbulent structures within the frequency ranges between the high-pass and low-pass filter settings. The simulated demodulated signals and cross correlation signals will then also be generated using only turbulent structures within the frequency ranges between the high-pass and low-pass filter sittings. Hence, sensitivity to high-pass and low-pass filters can also be studied by using these simulations.

Figure 3.13 shows a portion of a simulated velocity field with no high-pass or low-pass filters applied, Figure 3.14 shows the same portion of a simulated velocity field, that was simulated using identical parameters to the filed in Figure 3.13, except the field in Figure 3.14 has high-pass and low-pass filters

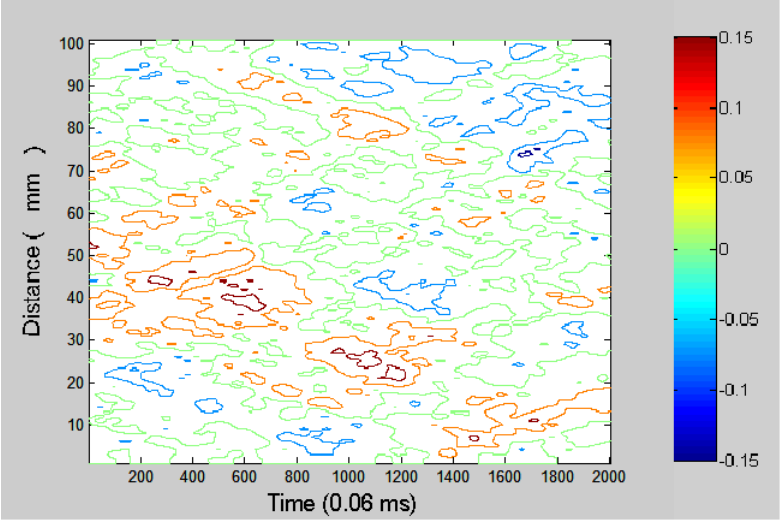

Figure 3.13: Simulated radial turbulent fluctuations velocity in meters per second, as a function of time and location along the diameter. Time is along the horizontal axis, covering a span of 120 milliseconds. Location along the diameter is along the vertical axis, covering the entire diameter's length of 0.1 meters. The portion of the simulated velocity field shown is a small portion of the entire simulation which spans 4 seconds.

set at 12 Hz and 25 Hz respectively. Figure 3.15 shows the same portion of a simulated velocity field, that was simulated using identical parameters to the fields in Figure 3.13, except the field in Figure 3.15 has high-pass and low-pass filters set at 12 Hz and 50 Hz respectively. The colours indicate radial turbulent velocity from approximately -0.15m/s to 0.15m/s, with blue being lower velocity and red being higher velocity.

Figure 3.16 shows a portion of the simulated demodulated signals from the simulations shown in Figure 3.13, Figure 3.14, and Figure 3.15, in blue, red, and black respectively. As expected, the blue curve contains characteristics of highest and lowest frequencies, compared to the other two curves. The red and black curves show low frequency characteristics of roughly the same frequency, but the black curve shows slightly higher frequency structures than the red curve.

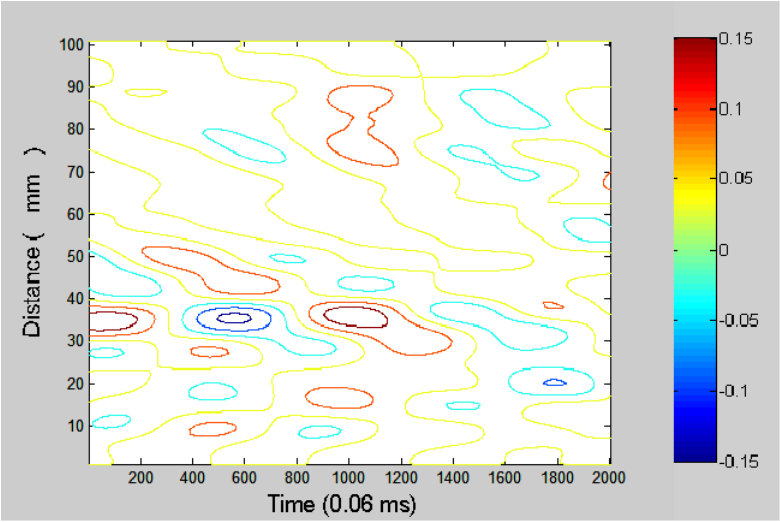

Figure 3.14: The contours in Figure 3.14 are the results of a simulation with the exact same parameters are the simulation from which the contours in Figure 3.13 were taken, except the simulation in Figure 3.14 has high pass and low pass filters at 12Hz and 25 Hz respectively.

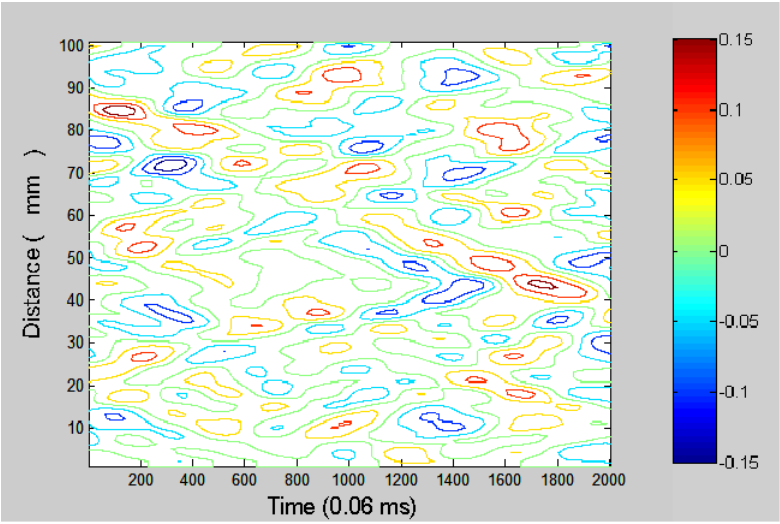

Figure 3.15: The contours in Figure 3.15 are the results of a simulation with the exact same parameters are the simulation from which the contours in Figure 3.13 were taken, except the simulation in Figure 3.15 has high pass and low pass filters at 12Hz and 50Hz respectively.

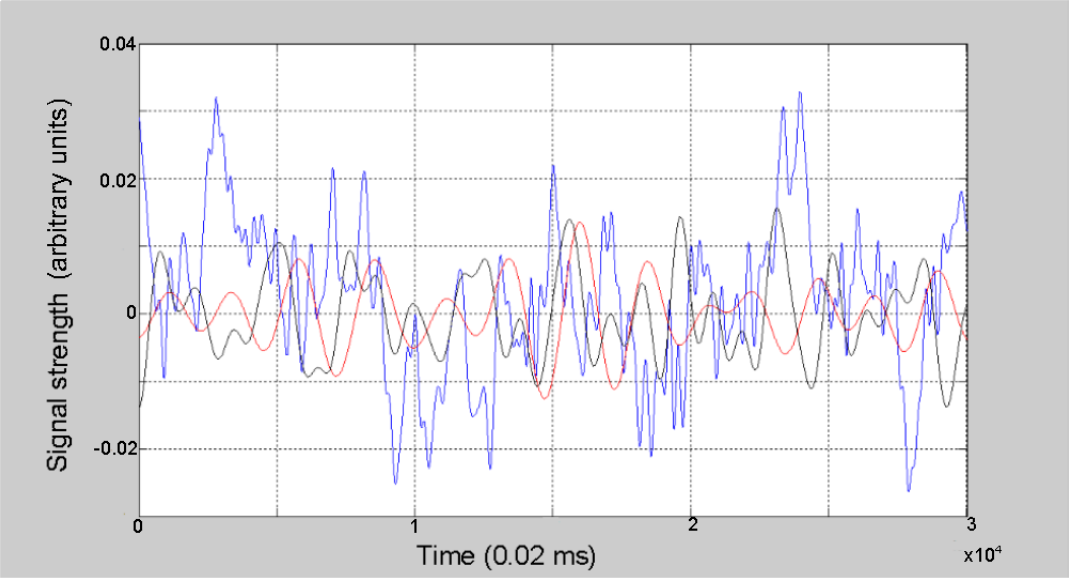

Figure 3.16: A portion of the simulated demodulated signals from the simulations shown in Figure 13, Figure 3.14, and Figure 3.15, in blue, red, and black respectively.

Turbulence Intensity Along Pipe Diameter

The factor $C_j(y)$ is defined as $C_j(y) = C(y) \cdot S_j$ where $C_(y)$ is a user specified function that controls the turbulence intensity along the pipe diameter, and S_j is the turbulence power spectrum. $C(y)$ is equal to zero at the pipe walls, in order to assure that the no slip condition is met. Between the pipe walls, it typically follows a near flat profile, as demonstrated by Laufer et al [101]. Figure 3.17 shows two possible curves for the function $C(y)$. The x-axis is location along the pipe diameter, and the y-axis values are irrelevant, since the flow velocity field is multiplied by S_j to obtain the function $C_j(y)$, and then normalized by factor k_j . More on the order of operations of the simulation algorithm is described in Section 2.4. The equation for the blue curve in Figure 3.17 is

$$y = M(1 - \frac{r}{R})^{1/20} \tag{3.6}$$

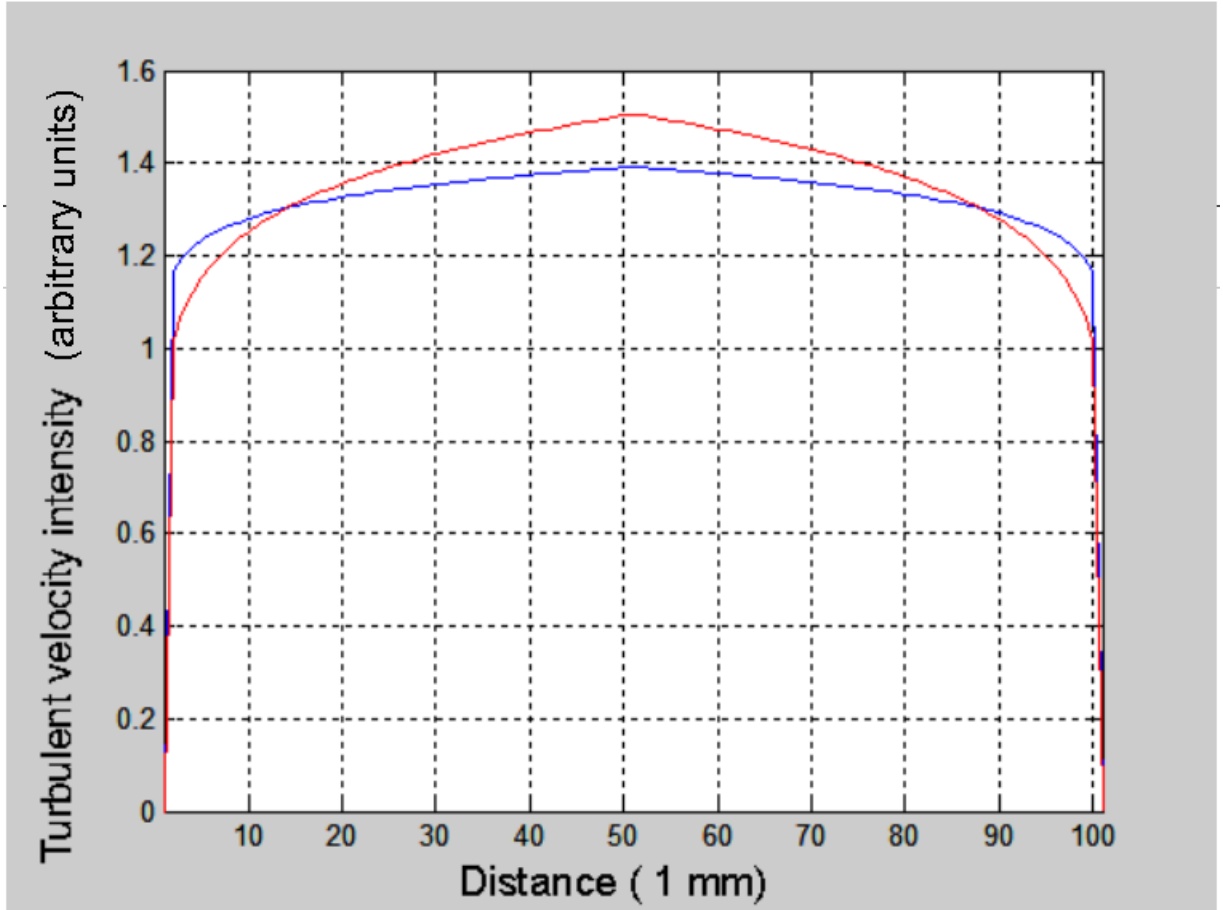

Figure 3.17: Two possible curves for the function C(y)

and the equation for the red curve is

$$y = M(1 - \frac{r}{R})^{1/9} \tag{3.7}$$

where M is the maximum value along the y-axis, r is the distance from the pipe center, and R is the pipe radius.

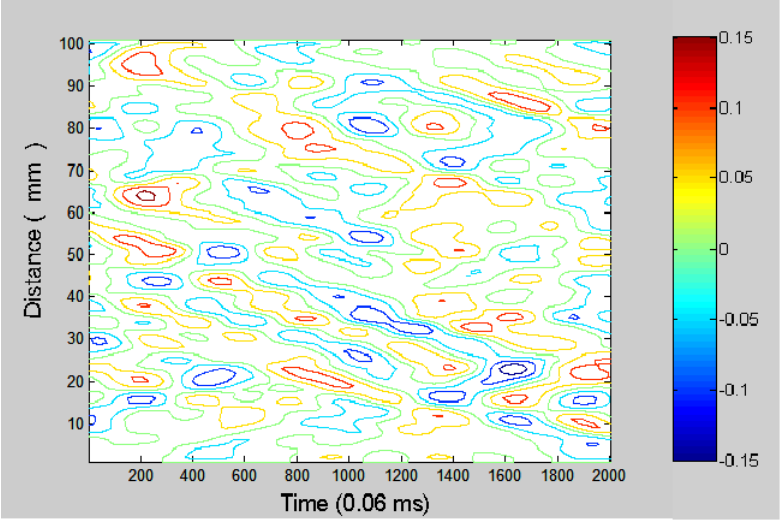

Figure 3.18: Simulated radial turbulent fluctuations velocity in meters per second, as a function of time and location along the diameter. Time is along the horizontal axis, covering a span of 120 milliseconds. Location along the diameter is along the vertical axis, covering the entire diameter's length of 0.1 meters. The portion of the simulated velocity field shown is a small portion of the entire simulation which spans 4 seconds. Simulation uses equation (3.6) for function C(y).

Figure 3.18 and Figure 3.19 show a portion of a simulated turbulence velocity field. The field in Figure 3.18 uses the blue curve for $C(y)$ from Figure 3.17, and the field in 3.19 uses the red curve for C(y) from Figure 3.17. One can see that Figure 3.18, showing a simulation that uses a flatter profile of radial turbulence intensity dependence, shows a velocity field with intense velocity fluctuations spread rather evenly along the pipe diameter. Figure 3.19, on the other hand, shows higher turbulent velocity fluctuations near the center of the pipe, than closer to the edges. The colours indicate radial turbulent velocity from approximately -0.15m/s to 0.15m/s, with blue being lower velocity and red being higher velocity.

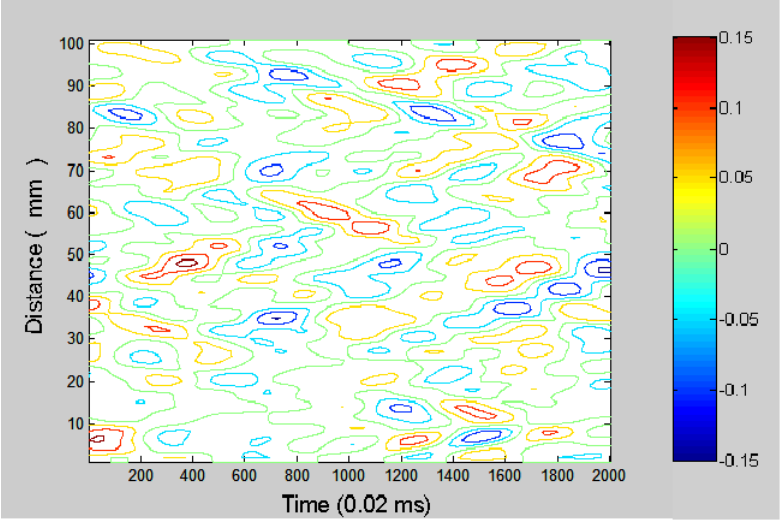

Figure 3.19: The contours in Figure 3.19 are the results of a simulation with the exact same parameters are the simulation from which the contours in Figure 3.18 were taken, except the simulation in Figure 3.19 uses equation (3.17) for function C(y).

Correlation of Turbulent Structures Along Pipe Diameter

Recall, function $\theta_j(y)$ is defined in equation (3.5) as

$$\begin{aligned} \theta_0(y) &= 0 \\ \theta_{j+1}(y) &= \pi \sin(\frac{\pi y j}{p N_y} + q_j) \end{aligned} \tag{3.8}$$

In function $\theta_j(y)$, the user specifies the values p, N_y , and the maximum values of j. The values q_j are randomly generated phase shifts, and are not specified by the user. N_y is the number of cells along the pipe diameter used in the simulation. The maximum value of j is determined by the formula

$$m = \frac{TUn}{D} \tag{3.9}$$

where m is the maximum value of j, T is the time domain of the simulated velocity field, U is the cross section average flow velocity, and D is the pipe diameter. The value n is user defined, by the desired value of D/n, where D/n is the smallest characteristic radial length of simulated eddies. The values T, U, n, and D are all user specified. Since m must be an integer, the value TUn/D is rounded up. The value n is usually chosen to be the smallest realistic characteristic radial length of eddies that can be detected by the cross correlation flow meter, and are of interest to the user of the meter. Figure 3.20 and Figure 3.21 show portions of two simulated radial turbulent velocity fields. The field in Figure 3.20 uses $n = 8$, and the field in Figure 3.21 uses $n = 4$. It can be seen that the simulation using $n = 8$ produces eddies of smaller characteristic length, than the simulation using $n = 4$. No high-pass of low-pass filters were used in the simulations presented in Figure 3.20 and Figure 3.21. The colours indicate radial turbulent velocity from approximately -0.15m/s to 0.15m/s, with blue being lower velocity and red being higher velocity.

The key parameter in the function $\theta_j(y)$ is the value p. This value determines the correlation of turbulent velocity along the pipe diameter, for every value j, that is, for ever time harmonic in the simulation. The function $\theta_j(y)$ may be represented as a function of j and y. The level curves of an example of such a function, $\theta(j, y)$ are shown in Figure 3.22. The function $\theta(j, y)$ in Figure 3.22 has $n = 4$ and $p = 16$. The y-axis is the pipe diameter of length 0.1m, and the x-axis is the j values, i.e. the time harmonics of turbulent velocity fluctuations. For every j value, the fluctuations along the pipe diameter are different. As j increases, the fluctuations of $\theta(j, y)$ increase along the pipe diameter. Since $\theta(j, y)$ is the argument of the sinusoidal function forming the radial turbulent velocity field, structures of higher time frequency, i.e. higher j values, will change more along the pipe diameter, while structures of lower time frequency, i.e. lower j values, will change less

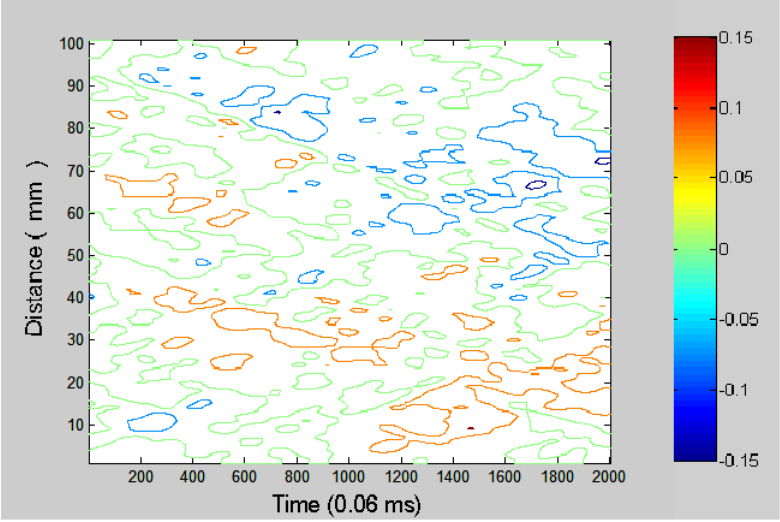

Figure 3.20: Simulated radial turbulent fluctuations velocity in meters per second, as a function of time and location along the diameter. Time is along the horizontal axis, covering a span of 120 milliseconds. Location along the diameter is along the vertical axis, covering the entire diameter's length of 0.1 meters. The portion of the simulated velocity field shown is a small portion of the entire simulation which spans 4 seconds. Simulation uses n=8 for the n value.

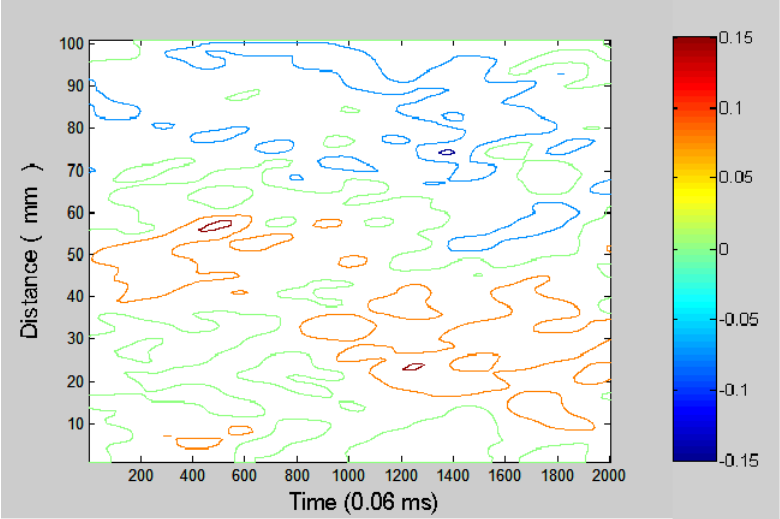

Figure 3.21: The contours in Figure 3.21 are the results of a simulation with the exact same parameters are the simulation from which the contours in Figure 3.20 were taken, except the simulation in Figure 3.21 uses n=4 for the n value.

along the pipe diameter. In the $\theta(j, y)$ function shown in Figure 3.22, the function is equal to zero for all j values below 5, as specified by the user. The user may choose at which j value to begin fluctuating values along the pipe diameter.

Figure 3.23 shows a $\theta(j, y)$ function with $p = 8$ instead of 16, and has $n = 4$ and the diameter is 0.1m just like the $\theta(j, y)$ function in Figure 3.22. Comparing the two figures, one can see that the $\theta(j, y)$ function in Figure 3.23 has greater fluctuation of $\theta(j, y)$ value for every j value. As a result, the simulated velocity field that uses the $\theta(j, y)$ function from Figure 3.23 will have faster deterioration of turbulent structures along the pipe diameter, than the simulated velocity field from Figure 3.22.

Figure 3.24 and Figure 3.25 show portions of two simulated radial turbulent velocity fields, using the $\theta(j, y)$ function from Figure 3.22 and Figure 3.23 respectively. One can see that the field shown in Figure 3.25 has eddies deteriorating faster along the diameter, compared to the field shown in Fig-

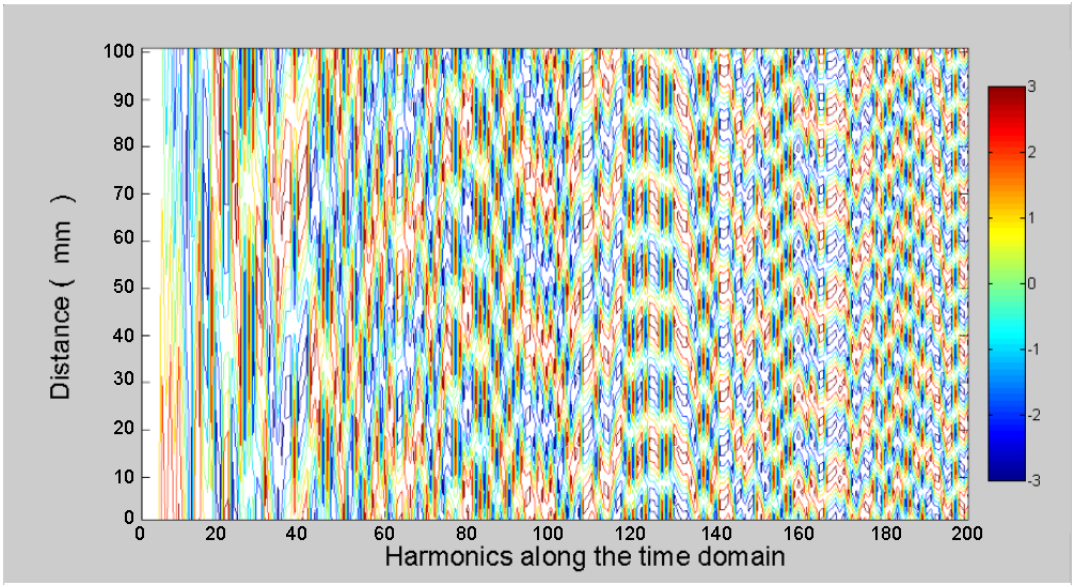

Figure 3.22: The phase correlation function with n=4 and p=16. The vertical axis is the pipe diameter of length 0.1m, and the horizontal axis is the j values, i.e. the time harmonics of turbulent velocity fluctuations.

ure 3.24. The colours indicate radial turbulent velocity from approximately -0.15m/s to 0.15m/s, with blue being lower velocity and red being higher velocity.

3.4 Simulation Algorithm

This section describes the simulation process. A typical simulation uses 100 cells along the pipe diameter, and approximately 200,000 cells along the time domain, each representing 0.00002 seconds. Simulating 5 seconds of real life measurement, which is approximately how long it takes a cross correlation flow meter to obtain one measurement, takes approximately 2 minutes on a personal laptop.

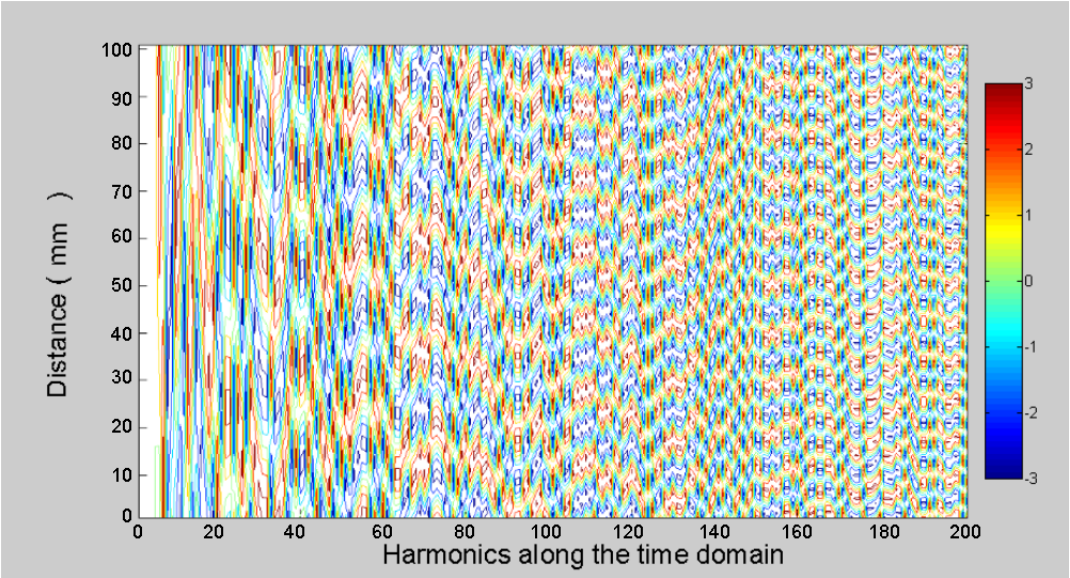

Figure 3.23: The phase correlation function is shown here with the same parameters as those used in Figure 3.22, except with p=8.

3.4.1 User Inputs

The user specifies the following properties:

D The physical length of the pipe diameter

T The time domain of the simulated radial turbulent velocity field at the upstream pipe cross section, henceforth referred to as cross section x=a

d_t The time resolution to be used in simulation

S_j The turbulence power spectrum to be used for simulation. This may be created by the user manually, or derived from a user determined demodulated signal and sample frequency used to collect the demodulated signal

$C(y)$ This function defines radial turbulent intensity distribution

$P(y)$ The time averaged axial velocity flow profile. Since simulation

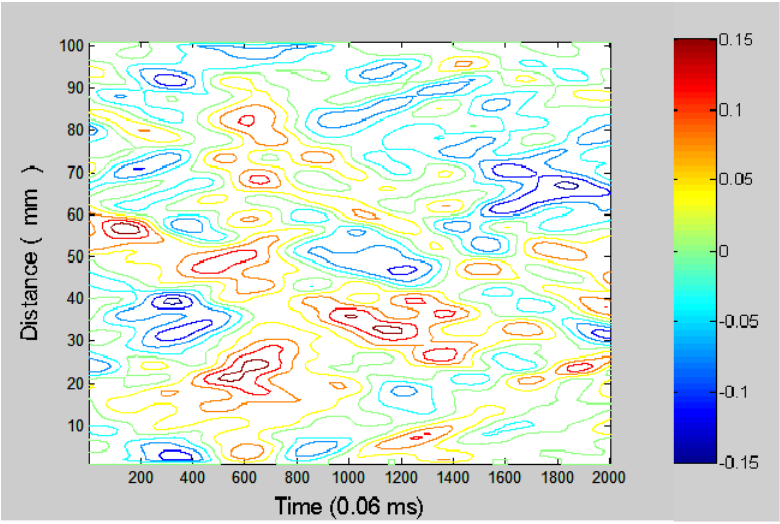

Figure 3.24: Simulated radial turbulent fluctuations velocity in meters per second, as a function of time and location along the diameter. Time is along the horizontal axis, covering a span of 120 milliseconds. Location along the diameter is along the vertical axis, covering the entire diameter's length of 0.1 meters. The portion of the simulated velocity field shown is a small portion of the entire simulation which spans 4 seconds. Simulation uses n=4 and p=16

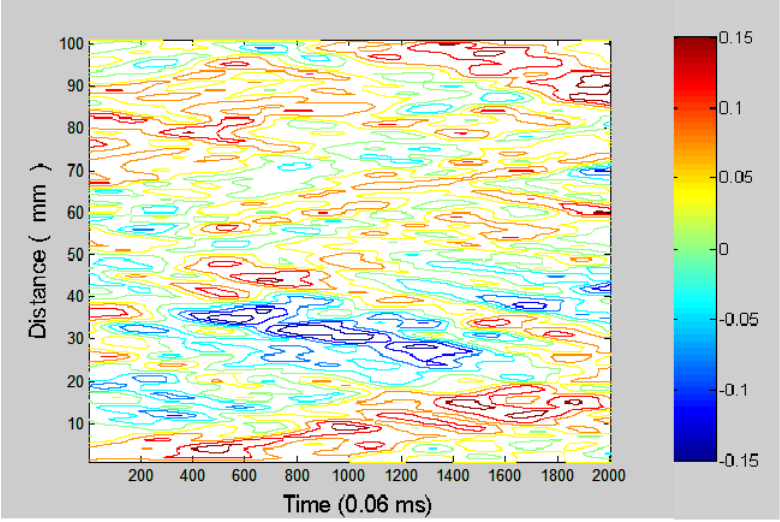

Figure 3.25: The contours in Figure 3.25 are the results of a simulation with the exact same parameters are the simulation from which the contours in Figure 3.24 were taken, except the simulation in Figure 3.25 uses a different phase correlation functions for which p=8.

is conducted on a single plane, this is only a function of position along the diameter, y, and not angle. P(y) is considered to be the axial flow profile after averaging over the angle.

N_y The number of spacial cells along the diameter to be used in the simulation n This defines the smallest length scale of turbulence in the direction of the diameter, to be simulated. This smallest scale is D/n.

p A value determining the level of correlation of phase along the pipe diameter. A greater value signifies greater correlation.

h_s The harmonic value after which phase correlation becomes non-constant.

L The distance between the upstream and downstream beams of the cross correlation flow meter who's measurements are to be simulated.

3.4.2 Numerical Computations

The simulation algorithm consists of a sequence of processes, which are described below.

Turbulent power spectrum

The power spectrum, S_j, is a function of frequency, though in the simulation it is a function of the variable j, which represent the number of the time harmonic. Since every harmonic corresponds to one and only one frequency, the relation between j and frequency is one-to-one. S_j may be created manually by the user, or derived from a user specified set of demodulated signals and sample frequency used to generate those signals.

In the case of derivation from a known demodulated signal set and sample frequency, which is usually the case, for every demodulated signal in the set, the absolute value of the fast Fourier transform is taken. All absolute values of the fast Fourier transform are then added, and the square root of the sum is taken. The result is the power spectrum along time harmonics representing the turbulent flow condition in the pipe. This power spectrum is derived from many demodulated signals, for example 100 signals representing 4 seconds each. The power spectrum is hence derived from 400 seconds of collected turbulence data. It is therefore considered an adequate representation of the state of turbulence in a pipe.

The power spectrum S_j may then be filtered if desired. Typically a hat-filter or Butterworth filters are used, although any user defined filter shape may be used. If a high-pass and low-pass frequency filter is used, the program determines two harmonics from the S_j function, which closest correspond to the user selected high-pass and low-pass frequencies, and bases the filter shape on those harmonics. The new filtered S_j is then used to simulate the radial turbulent velocity field.

Turbulence Phase Correlation

The function $\theta_j(y)$, determined using the user specified values of p, n, N_y, and h_s, defines the correlation of values of the radial turbulent velocity field along the pipe diameter. In effect, it defines the radial scale of turbulent eddies. The user specifies the number of cells to be used to define the pipe diameter (N_y), the number of time harmonics to be used in the simulation (m value determined from n value, see equation (3.9)), a value determining the level of correlation (p), and the lowest harmonic at which non-perfect correlation should occur (h_s).

Generation of Upstream Radial Turbulent Velocity Field

Following the creation of the square root of the filtered turbulent power spectrum S_j, and the phase correlation function $\theta_j(y)$, the upstream radial turbulent velocity field may be generated. This is accomplished using the following steps.

The number of cells representing the time domain are determined using the user specified time domain and time resolution. Since the user specified time domain might not be a multiple of the user specified time resolution, the program conducts rounding and as a result generates a time domain greater than or equal to the user specified time domain, with a resolution very close to the user specified resolution.

The function $C_j(y)$ is then defined as

$$C_j(y) = C(y)S_j \tag{3.10}$$

Functions $\alpha_j(y)$ and $\beta_j(y)$ are then defined as

$$\alpha_j(y) = C_j(y)\cos(\theta_j(y))$$
$$\beta_j(y) = C_j(y)\sin(\theta_j(y)) \tag{3.11}$$

For every y value, $\alpha_j(y)$ and $\beta_j(y)$ are the Fourier coefficients of the to-be-simulated radial turbulent velocity field. By defining them as described above, the shape of the turbulent power spectrum for every location along the pipe diameter will resemble the shape of S_j. With the phase correlation function $\theta_j(y)$ as the argument in these definitions, the correlation along the pipe diameter will fade faster for greater harmonics than for smaller harmonics. As a result, eddies smaller in the x-domain will also be smaller in the y-domain.

Next, the functions Γ_j and Δ_j are defined as the y-integrals of $\alpha_j(y)$ and $\beta_j(y)$ respectively. Since the demodulated signal is the y-integral of the radial turbulent velocity field, Γ_j and Δ_j are the Fourier coefficients of the demodulated signal.

The function k_j is then defined as

$$k_j = \pm\sqrt{\frac{S_j}{{\Gamma_j}^2 + {\Delta_j}^2}} \tag{3.12}$$

k_j is the multiplier at the front of the equation defining $v(y,t)$. So far, the Fourier coefficients of the velocity field have been defined to have the desired shape for every y value, but the same shape must exist for the Fourier coefficients of the integral, so that the demodulate signal has the desired turbulent spectrum. To ensure this, the functions $\alpha_j(y)$ and $\beta_j(y)$ are then redefined as follows, to maintain their shape per y-value, but alter their magnitude per

harmonic.

$$\begin{aligned} \hat{\alpha_j}(y) &= k_j \alpha_j(y) \\ \hat{\beta_j}(y) &= k_j \beta_j(y) \end{aligned} \tag{3.13}$$

Now that the final Fourier coefficients have been defined for the radial turbulent velocity field, the field may be generated. This is done by defining a function

$$F_j(y) = \hat{\alpha_j}(y) - i\hat{\beta_j(y)} \tag{3.14}$$

Although F is a function of j and not time t, its j domain is equal in amount of cells to the desired time domain of the to-be-simulated velocity field. Since the number of cells along the time domain will exceed the number of harmonics, the function F will have many "extra" slots in its harmonic domain, all of which are filled with zeros. In effect, for every y value, F defines the Fourier transform of the to-be-simulated velocity field. The velocity field is then generated by taking the inverse fast Fourier transform of F for every y value.

One must note that although F is a function of two variables, the inverse Fourier transform taken is a one-dimensional inverse Fourier transform, not a two-dimensional inverse Fourier transform. For every y value, keeping that value constant, F becomes a function of one variable j. The one dimensional inverse fast Fourier transform of this function of one variable is taken to create the slice of the velocity field for that particular y value. For the next y value, another one dimensional inverse fast Fourier transform is taken to create the slice of the velocity field for that y value. Due the the phase

correlation function $\theta_j(y)$, these slices will form coherent structures who's scales in the time and radial domains will be as the user specifies.

After the initial generation of the radial turbulent velocity field, the field is the desired shape, but not necessarily the desired magnitude. The field must be scaled using the user specified time averaged axial flow velocity. The reason for the scaling is that the simulated upstream radial turbulent velocity field is used, along with the axial flow profile, to generate the downstream radial turbulent velocity field, and hence, the upstream radial turbulent velocity field must be scaled to represent a flow condition that realistically corresponds to the axial flow profile. This scaling is done as follows:

$$v_{new}(y,t) = v(y,t)\frac{0.04U}{v_{rms}} \tag{3.15}$$

where v_{new} is the new velocity field, v is the old velocity field, U is the cross section average axial flow velocity, and v_{rms} is the root-mean-square of the old velocity field. The multiplier 0.04 determines the turbulence intensity as a percentage of U. It was chosen by the author to be 0.04 for this algorithm, since it is a typical value for pipe flow [102]. The user may select a different multiplier if desired.

The cross section average axial flow velocity, U, is determined using the axial flow profile $P(y)$. Since $P(y)$ is considered to be the axial flow profile averaged over time and angle, the value U is determined using the equation

$$U = \frac{1}{R^2}\int_{-R}^{R} P(y)r\,dr \tag{3.16}$$

Where R is the pipe radius, and r is the distance from the center of the pipe to the location y along the diameter.

Generation of the Time and Angle Averaged Flow Profile P(y)

$P(y)$ may be create manually by the user, or generated using other computational flow simulation methods. When generated by the user, typically the following equation is used

$$P(r) = U_{max}(1 - \frac{r}{R})^{\frac{1}{n}} \tag{3.17}$$

where U_{max} is the velocity at the center of the pipe, r is the location along the radius, R is the radius of the pipe, and n is a user specified value determining the flow profile flatness. Equation (3.17) is commonly used when describing axial flow profile of turbulent flow [102]. The greater the number n, the flatter the profile. An n value is chosen based on fluid dynamics knowledge about the simulated flow condition. Typically, an n value between 7 and 20 is used. This n value has nothing to do with the n value in the phase correlation function $\theta_j(y)$. For comparison of simulated and experimental results conducted in this work, the n values were selected based on RANS simulations.

Generation of Downstream Radial Turbulent Velocity Field

The upstream simulated turbulent velocity field represents a characteristic turbulent picture at cross section $x = a$, corresponding to the upstream beam of a cross correlation flow meter. This simulated field, along with the time and angle averaged axial flow profile $P(y)$, is used to simulate a downstream turbulent velocity field at cross section $x = b$, corresponding to the downstream beam of the cross correlation flow meter. The downstream velocity field is generated using the following formula

$$v_b(y,t) = v_a(y, t - \frac{L}{P(y)}) \tag{3.18}$$

where v_b is the velocity field at $x = b$, and v_a is the velocity field at $x = a$. L is specified by the user, and is equal to $b - a$. This formula is based on the Locally Frozen Turbulence Approximation, as discussed in Chapter 2. Since the downstream velocity field can not be defined for all time values that the upstream velocity field is defined for, the upstream field is truncated to be defined for the same time values as the downstream field.

Figure 3.26 shows a portion of a simulated upstream radial turbulent velocity field, and Figure 3.27 shows the same portion of the corresponding downstream radial turbulent velocity field. The flow velocity for the fields in Figure 3.26 and Figure 3.27 is 1.25 m/s, the pipe diameter is 0.1 m, and the distance between upstream and downstream cross sections is 0.1 m. One can see that the turbulent structures pictures in Figure 3.26 appear at a later time in Figure 3.27. From first glance, these figures may appear unrelated, but upon closer inspection it becomes clear that they share some of the same turbulent eddies slightly deformed, and shifted in time. More specifically, the eddies on the left side of figure 3.26 can be recognized on the right side of figure 3.27. The time shift depends on location along the y-axis, because the axial flow profile depends on location along the y-axis. Specifically, turbulent structures closer to the pipe walls in Figure 3.126 are seen later in time in Figure 3.27, compared to turbulent structures farther from the walls. This is because the axial flow is slower closer to the walls, and hence it takes the turbulent structures more time to reach the downstream ultrasonic beam. Due to the time shift depending on the y-axis, some turbulent structures seen in Figure 3.26 appear recognizable but slightly deformed in Figure 3.27. The colours indicate radial turbulent velocity from approximately -0.15m/s to 0.15m/s, with blue being lower velocity and red being higher velocity.

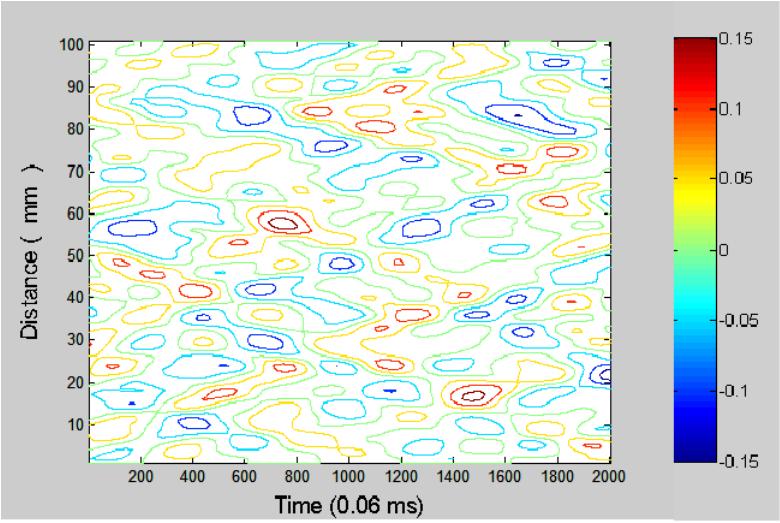

Figure 3.26: Simulated upstream radial turbulent fluctuations velocity in meters per second, as a function of time and location along the diameter. Time is along the horizontal axis, covering a span of 120 milliseconds. Location along the diameter is along the vertical axis, covering the entire diameter's length of 0.1 meters. The portion of the simulated velocity field shown is a small portion of the entire simulation, which spans 4 seconds.

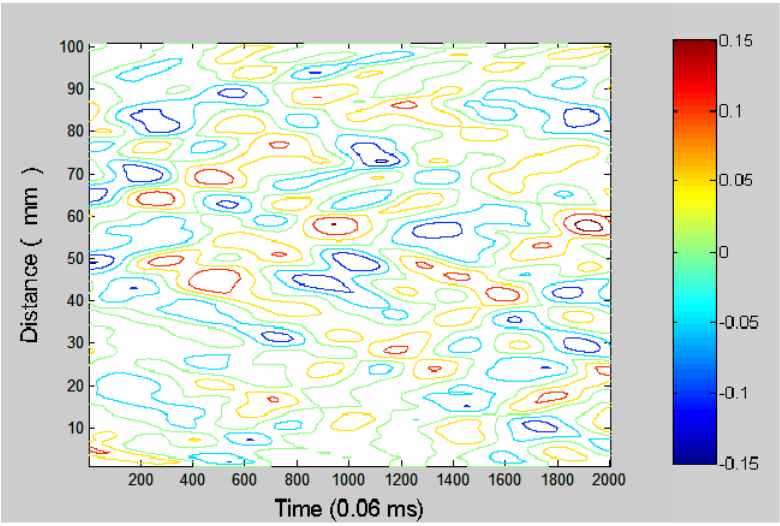

Figure 3.27: Simulated downstream radial turbulent fluctuations velocity in meters per second, corresponding to the upstream field in Figure 3.26, as a function of time and location along the diameter.

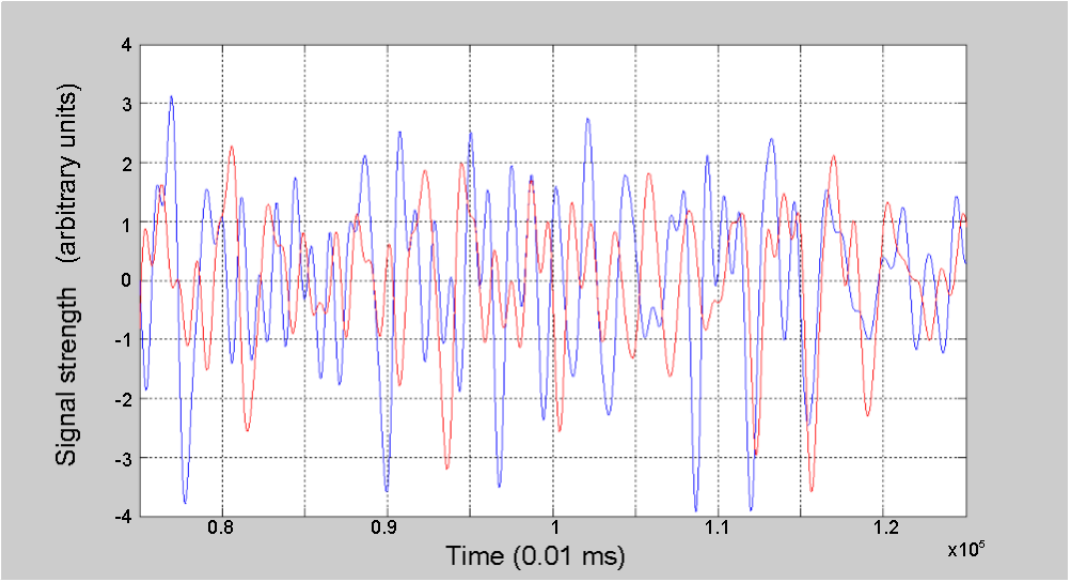

Figure 3.28: Upstream simulated demodulated signal (blue) and corresponding downstream simulated demodulated signal (red). The horizontal axis is time index, spanning 1 second. The vertical axis is signal strength, and units are arbitrary. The flow velocity is 1.25 m/s and the distance between upstream and downstream beams is 0.1 m.

Generation of Simulated Measured Flow Velocity

The cross correlation flow meter derives a measured flow velocity by comparing the y-integrals of the radial turbulent velocity fields at the upstream and downstream locations. For this reason, the next stage in simulation is the integration, along the pipe diameter, of the simulated upstream and downstream radial turbulent velocity fields. The result is a simulated upstream demodulated signal, and a simulated downstream demodulated signal. Figure 3.28 shows two such simulated demodulated signals, using the same simulated fields shown in Figure 3.26 and Figure 3.27. The blue signal is upstream demodulated signal, and the red signal is downstream demodulated signal. Figure 3.28 shows a 1 second portion of the 4 second demodulated signals.

The simulated upstream and downstream demodulated signals are then cross correlated, to generate a simulated cross correlation function. Figure

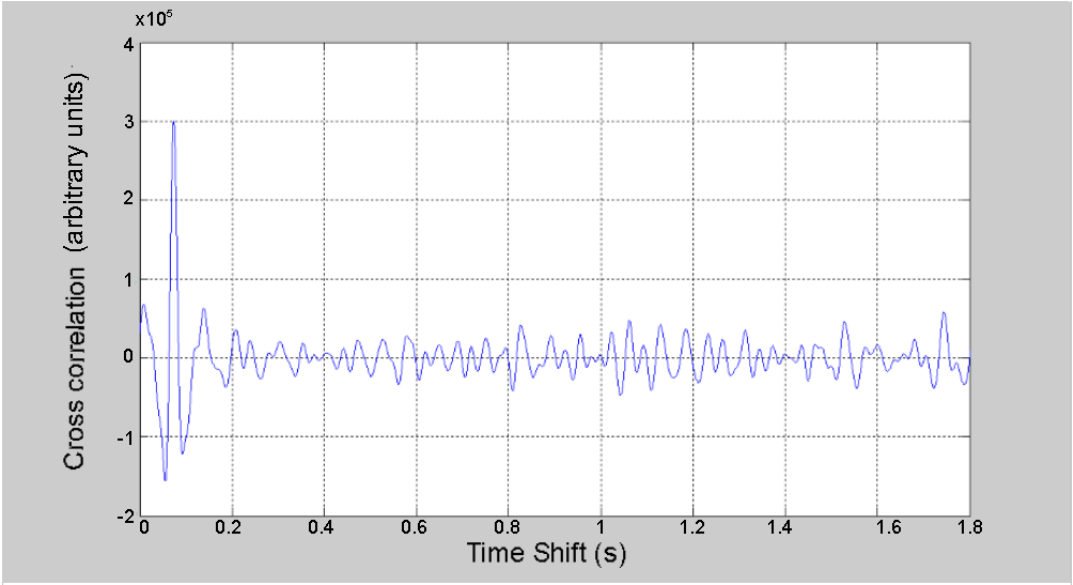

Figure 3.29: Cross correlation function of simulated upstream and downstream demodulated signals shown in Figure 3.28.

3.29 shows the cross correlation of the signals shown in Figure 3.28.

The location of the peak of the cross correlation function, is the time shift value for which the upstream and downstream demodulated signals are most similar. This is the time delay described in earlier chapters, indicating the characteristic time it takes the turbulent picture to move from the upstream cross section to the downstream cross section. Since the turbulent picture is moved forward by the axial flow velocity, the distance between the ultrasonic beams may be divided by the simulated time delay, i.e. the location of the peak of the simulated cross correlation function, in order to obtain a simulated measured velocity.

In the case presented in Figure 3.29, the location of the peak is 0.07334 seconds, and the distance between the upstream and downstream beams is 0.1 meters, hence the simulated measured flow velocity is 1.36 m/s. Knowing that the actual flow velocity used in the simulation is 1.25 m/s, the simulation results suggest that the hydraulic factor, obtained by dividing the actual flow

velocity by the measured flow velocity, is approximately 0.92 when conducting cross correlation flow measurement on the simulated flow condition. The simulated value of 0.92 is in good agreement with real cross correlation flow measurement observations. The hydraulic factor is typically smaller than 1, because cross correlation flow measurement is more sensitive to motion in the center of the pipe, where flow velocity is higher than the cross section average flow velocity. A detailed comparison of simulated and experimental hydraulic factors is given in Chapter 5.

Use of the simulation method described in this chapter, allows one to simulated measured velocity and hydraulic factor of the cross correlation flow meter, for flow conditions specified by the user. These simulation methods also allow one to study turbulent flow for other applications.

Chapter 4

Experimental Investigation of Cross Correlation Flow Measurement

Laboratory testing to validate the developed mathematical model was conducted at Advanced Measurement and Analysis Group Inc. (AMAG) laboratory in Canada. A flow loop was designed by AMAG engineers, including the author. A major purpose of the construction of this flow loop was the validation of theoretical analysis conducted as part of this work. This flow loop had a test section consisting of a straight 240" run of 4" diameter pipe, following two in-plane 90-degree bends. Ultrasonic cross correlation flow meters, provided by AMAG, were modified to allow measurement with difference spacings between ultrasonic beams of the cross correlation flow meter. Flow conditions were varied by changing the location of measurement along the test section of the piping configuration. More detail on test conditions are given in Section 4.2 and Section 4.3.

4.1 Equipment

The ultrasonic cross correlation flow measurement transducers that were used, are composed of a frame that attaches to the pipe, probes that are

Figure 4.1: Cross correlation flow meter setup.

inserted into the frame, and cables and electronics used to conduct measurements. Two photographs and a diagram of a typical flow measurement setup is shown in Figure 4.1, and Figure 4.2 respectively. A detailed description of the various pieces of equipment will follow.

A basic transducer uses four probes, and transmits ultrasonic signals through a single spacial plane. Figure 4.3 demonstrates this setup. It is possible to construct a transducer that transmits ultrasonic signals through many spacial planes, hence producing multiple measurements at the same time and location. These multiple planes can be planes of different sizes in the same greater spacial plane, as shown in Figure 4.4, or can be planes in different greater spacial planes, as seen in the foreground of figure 4.1. In these laboratory tests, two types of frames were used, called a Multispacing Frame and a Multibeam Frame, more commonly referred to as a multispacing transducer and multibeam transducer. In the work presented in this

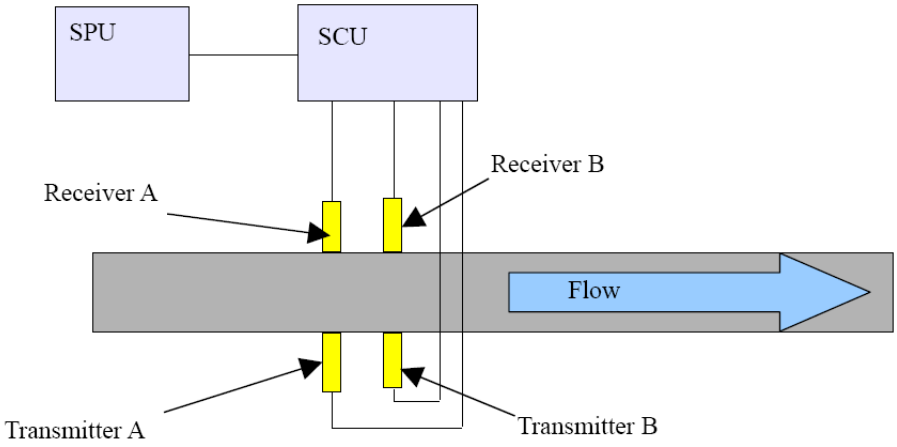

Figure 4.2: Cross correlation flow meter setup diagram.

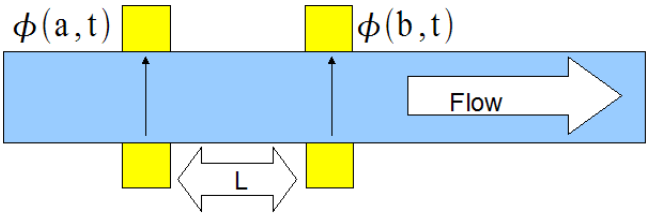

Figure 4.3: Cross correlation flow measurement concept.

thesis, only the results obtained with the mulitspacing transducer, and regular transducers, are used.

The multispacing transducer used in these tests, measures flow in a single greater spacial plane, but with two different nominal spacings of 0.5D and 3D, where D is the nominal inner pipe diameter of 4 inches (10cm). A photograph of this multispacing transducer is shown in Figure 4.5. Multispacing transducers were designed specifically for these laboratory tests, and have not been used for measurements in nuclear power plants in the past.

The purpose of the frames is to hold ultrasonic probes on the pipe, while the ultrasonic probes transmit and receive signals. The multispacing transducer frame was designed and constructed by the author at the AMAG lab-

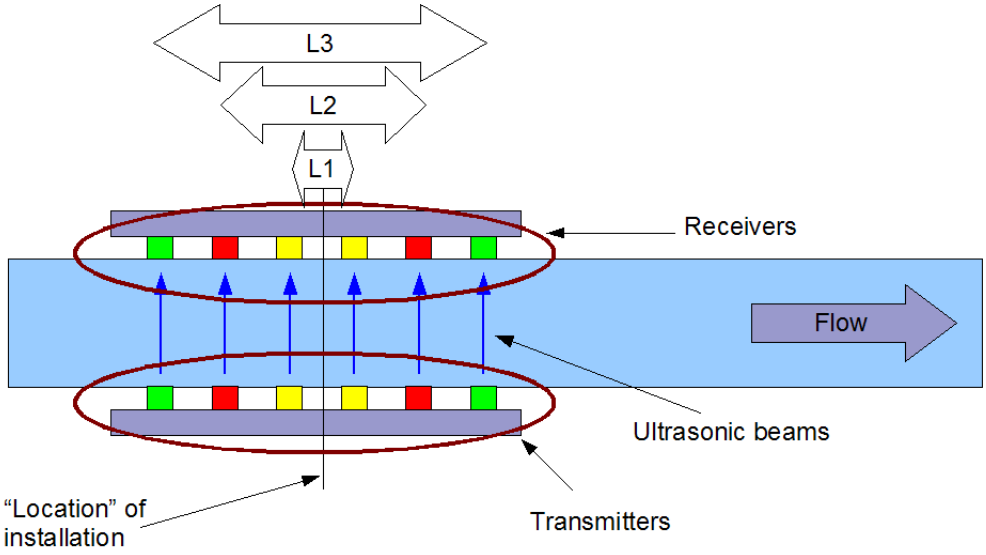

Figure 4.4: Multispacing transducer concept.

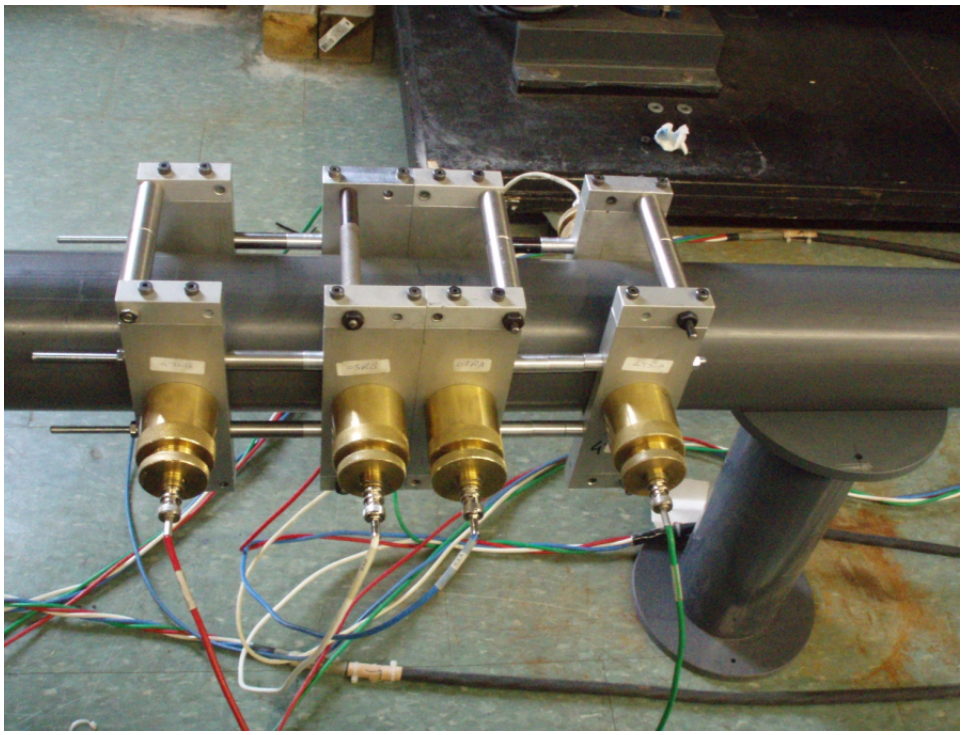

Figure 4.5: Multispacing transducer.

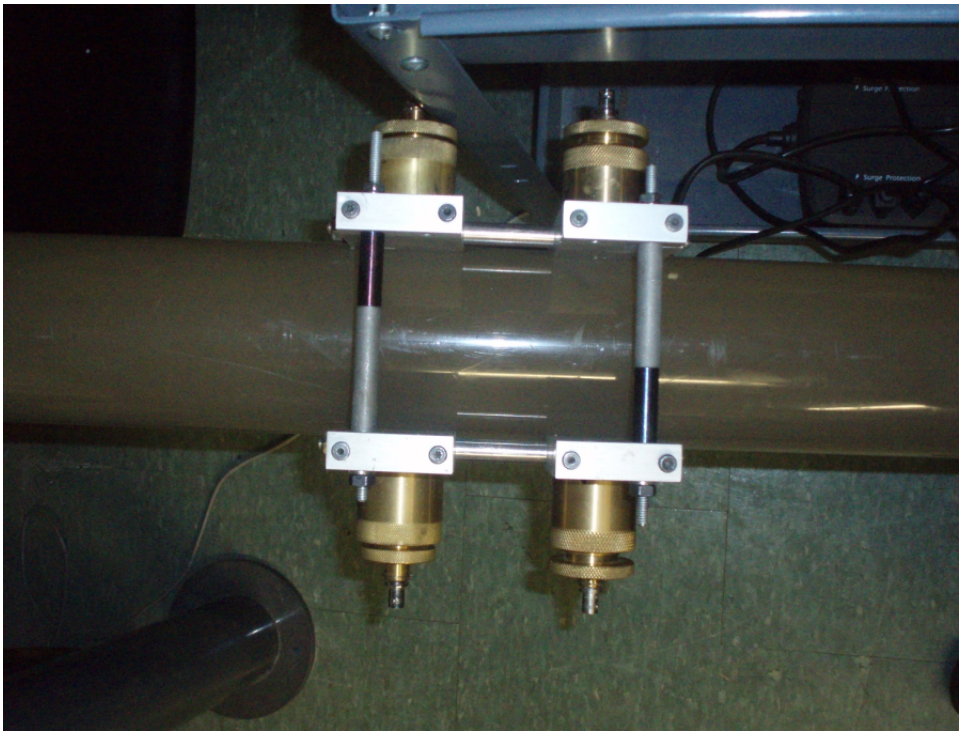

Figure 4.6: Cross correlation flow meter frame with probes and no cables.

oratory, specifically for these tests. The photograph in Figure 4.6 shows a frame with 4 attached probes and no cables. The probes in Figure 4.6 are the same type of probes used in these laboratory tests, and can also be used for flow measurement in nuclear power plants. These probes are designed and manufactured by AMAG, and used for flow measurements in industry.

The probes are composed of a piezoelectric crystal, and a structure holding the crystal in required contact with the pipe surface. The piezoelectric crystal vibrates if injected with an electric current, and releases an electric current if set into vibration.

The electronics consist of a signal processing unit (SPU), a signal conditioning unit (SCU), and cables connecting them to each other and the probes. Figure 4.7 shows the flow measurement process.

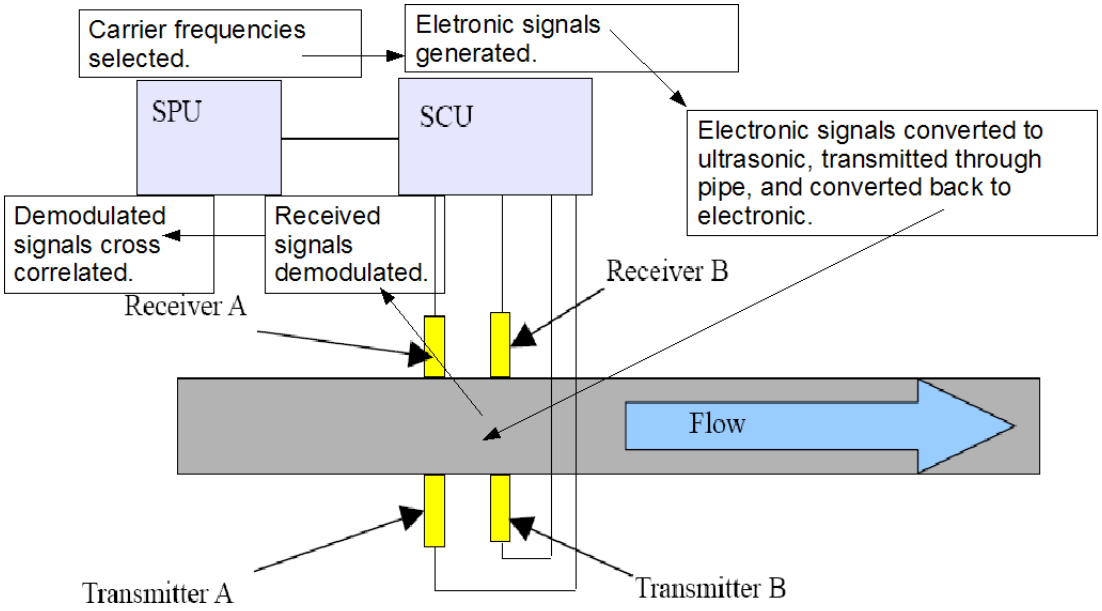

Figure 4.7: Cross correlation flow meter diagram.

The SPU selects a carrier frequency for an ultrasonic signal, and sends this information to the SCU. The SCU then generates an electrical signal corresponding to that frequency, and sends the signal to the probe. The piezoelectric crystal in the probe then vibrates at the selected frequency, sending an ultrasonic signal through the pipe wall, through water in the pipe to the other side of the pipe cross section along the pipe diameter, and through the pipe wall on the other side, reaching the piezoelectric crystal of the probe on the opposite side of the pipe. This process is shown in Figure 4.8.

The piezoelectric crystal of the receiving probe is then sent into vibration by the ultrasonic signal, and generates an electric signal that travels through cables to the SCU. The received signal is different from the transmitted signal, because the ultrasonic signal has been modulated by turbulence while passing through the pipe. The SCU performs phase demodulation of the received signal, removing the carrier frequency. As a result, a signal carrying only the signature of turbulence remains. This signal, called the *demodulated*

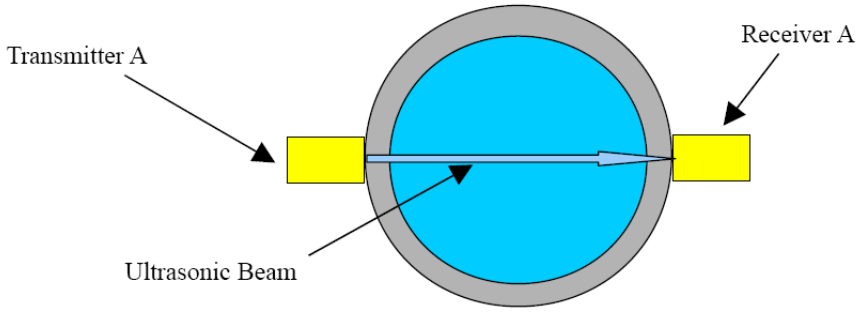

Figure 4.8: Ultrasonic beam transmitted along a pipe diameter for cross correlation flow measurement.

signal, is then sent to the SPU. For some cases, ultrasonic signals are affected by noise, such as pipe vibrations. For these cases, there are existing noise removal methods that may be applied.

The SPU is a customized computer with an AMAG software package for conducting flow measurement. The SPU receives two demodulated signals for a single flow measurement. These are the signals from the upstream and downstream ultrasonic beams, called signal x and signal y respectively. These signals carry the signature of the same turbulent structures traveling along the pipe, except signal y was disturbed by a set of structures a period of time later than signal x was disturbed by the same set of structures. This is because the traveling set of structures passed the upstream ultrasonic signal first, then traveled from the upstream signal's cross section to the downstream signal's cross section for some time, and then crossed the downstream signal. Hence, signals x and y should be somewhat similar if signal y is shifted back in time by the amount of time it took the turbulent structures to travel from the upstream probes' cross section to the downstream probes' cross section. The signals will not be identical after the time shift though, because turbulent structures deform, though not beyond recognition, while moving from the upstream signal location to the downstream signal location. This time shift, called *Time Delay* is defined by the location of the peak of the cross correlation of signal x and signal y. See Figure 4.9 below for two screen shots of measured flow values. These screen shots are

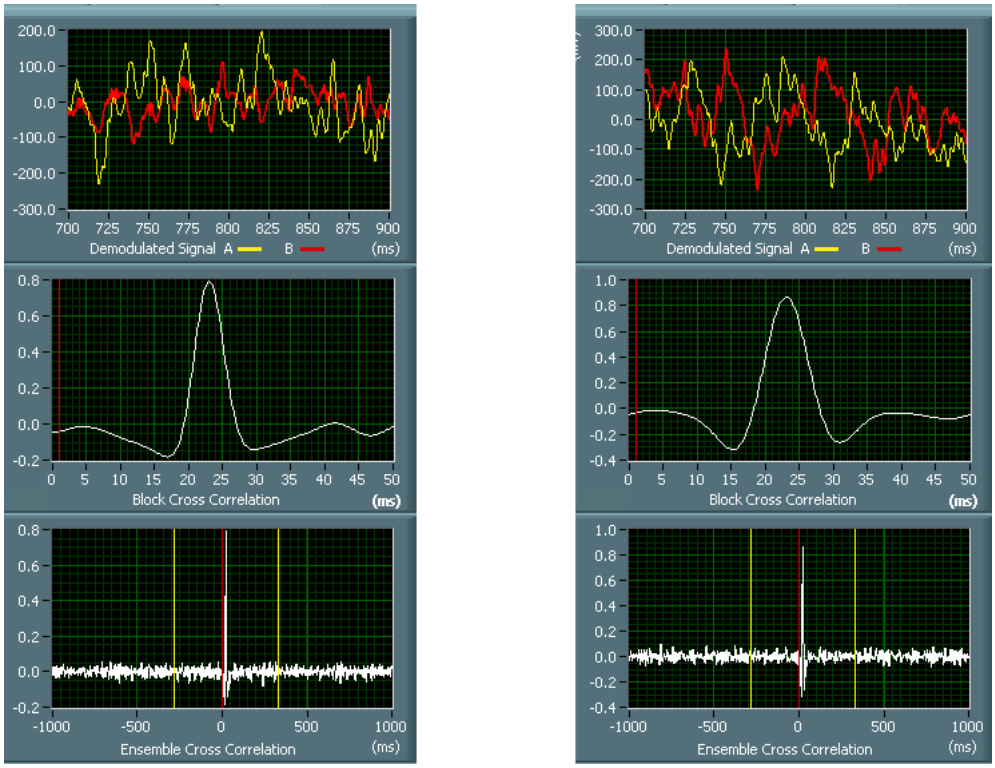

Figure 4.9: Screen shots of cross correlation curves from cross correlation flow measurement.

taken from the SPU screen during the laboratory tests described in this report.

The cross correlation of x and y is calculated by the SPU by taking the fast Fourier transform of x and y, being X and Y respectively, and then taking the inverse Fast Fourier Transform of X^cY, where X^c is the complex conjugate of X. This operation is based on the following cross correlation property [18].

$$F(f(t) \star g(t)) = F(f(t))^c F(g(t)) \tag{4.1}$$

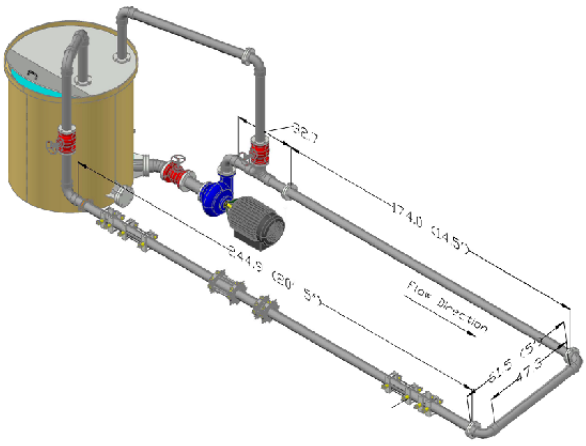

Figure 4.10: AMAG flow loop design.

Here, F denotes the Fourier Transform operator, and the star denotes the cross correlation of two functions.

4.2 Laboratory Setup and Test Preparation

The AMAG flow loop had a plastic test section consisting of a straight 240" run of 4" diameter pipe, following two in-plane 90-degree bends. The pipe walls between these bends was transparent, for ensuring that no air bubbles exist in the flow. Flow measurements were taken at nine locations downstream of the 90 degree bends. The flow loop was designed by AMAG engineers, including the author of this report, construction of separate parts for the loop was outsourced, and assembly of the loop was conducted by AMAG technicians. A sketch of the AMAG flow loop is given in Figure 4.10. The test section of the loop is shown in Figure 4.11.

Prior to formal laboratory testing, preliminary tests and measurements were conducted. Preliminary tests were conducted using single beam transducers of two different spacings of 1.1D and 3D, where D is the inner pipe diameter. A transducer of each of the two spacings was installed at two locations, approximately 9D from the upstream elbow, and 54D from the

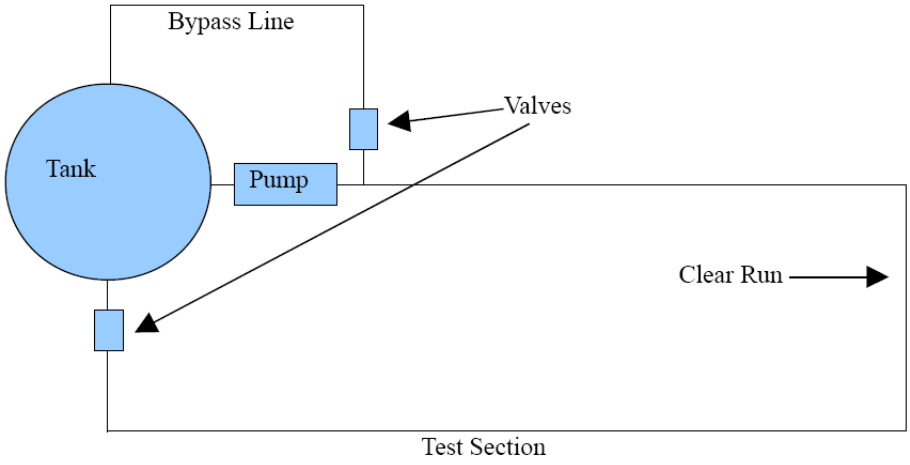

Figure 4.11: AMAG flow loop diagram.

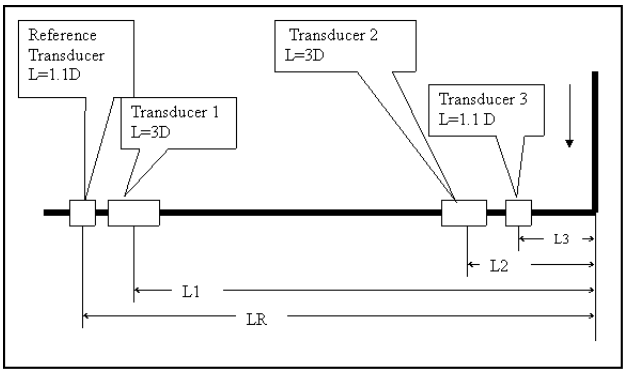

Figure 4.12: Preliminary test setup.

upstream elbow, along the test section of the loop. Figure 4.12 shows a diagram representing these preliminary tests. The preliminary tests showed that measured velocity depended on spacing and installation location, and hence motivated the laboratory tests described here.

Repeatability tests were also conducted, where transducer frames would be used to measure values at a particular location, and then taken off the pipe, then reinstalled in the same location, and used to measure flow again. The purpose of these tests was to evaluate the installation effect on flow

measurement values. All repeatability tests were conducted with a reference meter that was never removed from the pipe, in case the flow changed while the tested frame was being removed and reinstalled. Repeatability tests were conducting on all frames used in laboratory testing, and at different locations along the pipe. Variation of test results did not exceed 0.25%.

Measurements of inner pipe diameter were taken at six cross sections along the test section of the loop, and four orientations at every cross section. An average value over all orientations was taken to determine the inner diameter at each of the six cross sections, and the average value over the cross sections was used as the pipe inner diameter for flow calculations, rather than the nominal value of 4 inches. Inner pipe diameter was measured by measuring the outer pipe diameter, and wall thickness, at every location. Wall thickness measurements were conducted using an ultrasonic device. The two wall thickness measurements for every measurement location were subtracted from the outer diameter measurement to obtain an inner diameter measurement. Figure 4.13 shows a chart used for calculating inner pipe diameter at one of the six cross sections selected. Six measurements were taken for every orientation, to be sure of accurate measurement. Figure 4.14 shows a chart used to determine the average inner pipe diameter for the entire pipe, using all six cross sections selected. Every cross section measurement shown in Figure 4.14 was determined using the process demonstrated in Figure 4.13. Pipe wall temperature was also taken during these measurements, in case pipe diameter dependence on temperature were to be detected. It was later observed that pipe diameter was not significantly dependent on temperature.

Temperature measurements of the water and of the pipe wall were taken at different times while allowing flow through the pipe during the day, in order to determine temperature dependence on time, and whether it is a significant factor in calculations. It was determined that temperature did not play a significant role. Figure 4.15 shows a plot of water temperature measurements throughout the day. There are two different data sets, for two different days during which water temperature was measured during preliminary testing. Water temperature measurements were also regularly taken

Angular Position (deg)	Outer Diameter (inches)	Wall Thickness at x degrees (inches)		Inner Diameter (inches)
x to x+180		x	x+180	
0 to 180	4.5415	0.2590	0.2520	4.0305
	4.5405	0.2590	0.2520	4.0295
	4.5410	0.2590	0.2510	4.0310
	4.5270	0.2590	0.2510	4.0170
	4.5260	0.2590	0.2510	4.0160
	4.5260	0.2590	0.2510	4.0160
	4.5350	0.2600	0.2510	4.0240
	4.5355	0.2600	0.2510	4.0245
	4.5355	0.2600	0.2510	4.0245
45 to 225	4.5035	0.2630	0.2660	3.9745
	4.5035	0.2630	0.2660	3.9745
	4.5035	0.2630	0.2640	3.9765
	4.5010	0.2610	0.2660	3.9740
	4.5010	0.2610	0.2670	3.9730
	4.5020	0.2610	0.2680	3.9730
	4.5080	0.2630	0.2660	3.9790
	4.5090	0.2630	0.2660	3.9800
	4.5095	0.2630	0.2670	3.9795
90 to 270	4.4730	0.2660	0.2710	3.9360
	4.4730	0.2660	0.2710	3.9360
	4.4725	0.2660	0.2720	3.9345
	4.4825	0.2660	0.2720	3.9445
	4.4815	0.2670	0.2710	3.9435
	4.4805	0.2670	0.2710	3.9425
	4.4800	0.2690	0.2740	3.9370
	4.4795	0.2690	0.2750	3.9355
	4.4795	0.2690	0.2750	3.9355
135 to 315	4.5150	0.2640	0.2680	3.9830
	4.5145	0.2650	0.2680	3.9815
	4.5145	0.2660	0.2670	3.9815
	4.5060	0.2660	0.2660	3.9740
	4.5060	0.2700	0.2660	3.9700
	4.5065	0.2680	0.2660	3.9725
	4.5215	0.2660	0.2680	3.9875
	4.5205	0.2660	0.2690	3.9855
	4.5215	0.2660	0.2690	3.9865
			AVERAGE ID:	3.9796

Figure 4.13: Pipe inner diameter measurement at a single location.

during formal laboratory testing, although it was observed that water temperature did not have a significant effect on the ratio between measurements of the test meters and reference meter. Also, since repeatability tests were conducted at different temperatures, the temperature effect is included in the repeatability effect.

Distance From Flange (in)	ID (in)
23.0	3.9842
44.5	3.9866
122.5	3.9792
161.0	3.9763
204.0	3.9862
212.0	3.9796
AVERAGE	3.9820
Sample STD	0.0043
Smpl STD % Ave	0.1068

Figure 4.14: Average pipe inner diameter calculation.

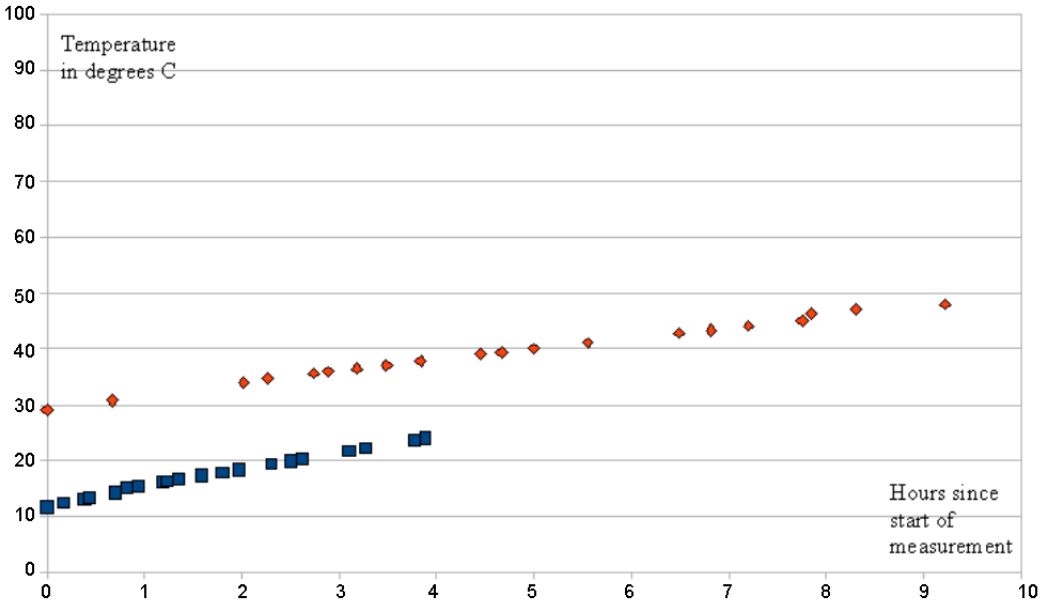

Figure 4.15: Flow temperature readings.

4.3 Conducting Laboratory Testing

Laboratory testing was conducted at the nominal flow rate of 4.6 m/s. For this flow rate, nine measurement locations downstream of a 90 degree bend were used, along with a tenth location used to install a reference meter. The nine locations were 6D, 9D, 12D, 15D, 20D, 25D, 30D, 42D, and 50D from the upstream 90 degree bend, where D is the nominal pipe diameter of 4 inches. The reference meter location was 58D from the upstream 90 degree bend, and the reference meter was a single beam meter with 1D spacing.

A photograph of part of the test section of the flow loop, with meters installed, is shown in Figure 4.16. Figure 4.16 depicts three frames: a multi-spacing frame, and two 1D beam frames one of which is used as a reference meter. The three transducer frames are circled on a smaller version of the photograph, under the larger version. The multibeam frame consist of a two sets of beams with 0.5D and 3D spacing, and is on the right side of figure 4.16. A single beam transducer with a nominal spacing of 1D was also used at every measurement location. As a result, every location was measured using 0.5D, 1D and 3D spacing. This 1D transducer is shown in the center-left of Figure 4.16. During measurement, the position of the frames along on pipe was defined by the center line between the upstream and downstream beams, which was the same for all three spacings. On the left most side of Figure 4.16 is another 1D single plane frame, used as a reference meter at that location for all test measurements.

Figure 4.17 shows the same set of transducer from a different angle, giving a better understanding of the structure of the metal frames.

Figure 4.16: Multispacing transducer next to sinlgebeam transducer and reference meter.

Every installation, at every measurement location, conducted measurement for approximately 2 hours. During testing, the electronics were set up to collect demodulated signal for 4 seconds to derive one velocity measurement data point. As a result, taking processing time into consideration, a data point was obtained approximate once every 5 seconds. During the low flow testing, the electronics were set up to spend 8 seconds collecting demodulated signal, and thus a data point was obtained approximately every 10 seconds.

The tests were conducted using a single plane multispacing transducer with 0.5D and 3D spacing, and a 1D single beam transducer. Both frames

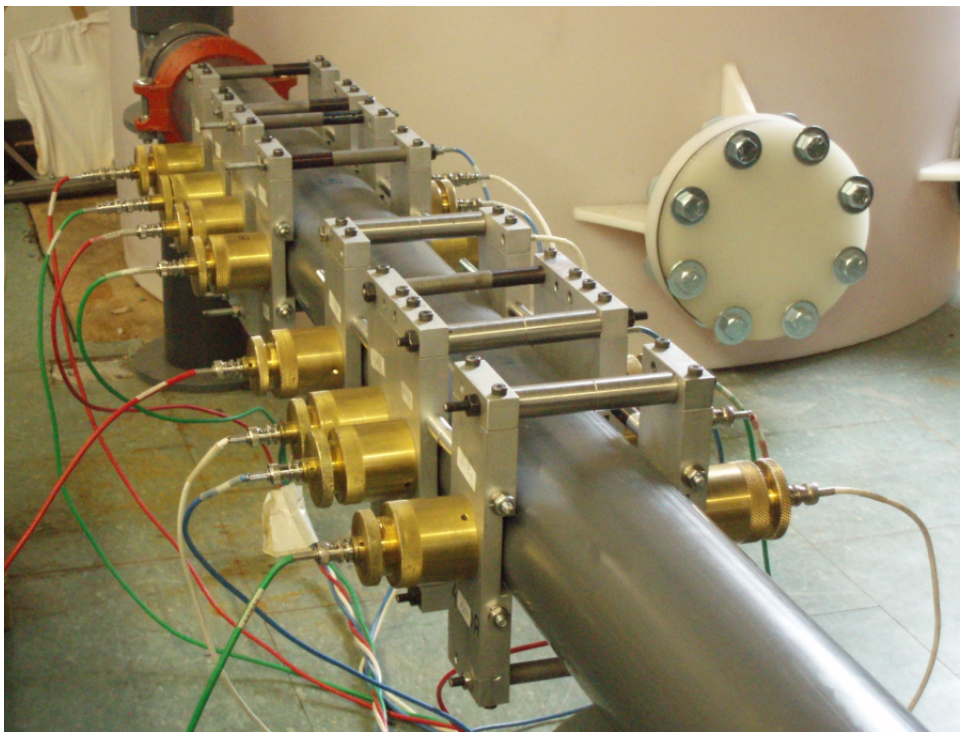

Figure 4.17: Multispacing transducer next to sinlgebeam transducer and reference meter.

were installed on each of the 9 locations by the end of the testing. First tests were conducted at every one of the 9 locations using only the 1D single beam transducer, by sliding it from location to location between the 2 hour measurement periods. Then, tests were conducted at every one of the 9 locations using the multispacing transducer.

By the end of the testing, with 9 locations measured for 2 hours each by a single beam 1D meter, and a multispacing 0.5D and 3D meter, approximately 60 hours of data were collected. Since a single measured point took roughly 5 seconds to produce, the testing produced over 40,000 data points to analyze.

4.4 Testing Uncertainty

Test results were presented as a hydraulic factor $C = V_a/V_m$, where V_a is the cross section average flow velocity determined by the reference meter, and V_m is the average measured flow velocity. Measured velocity, U_m is equal to the transducer spacing divided by the time delay, as shown in the equation below, and time delay is defined by the location of the cross correlation peak.

$$U_m = \frac{L}{\tau_m} \tag{4.2}$$

The reference meter was previously calibrated using a weight tank. According to standard AMAG uncertainty calculation methods, 95% confidence interval uncertainty of the reference meter was 0.6%, including uncertainty due to date scatter. Uncertainty of measurements, also with a 95% confidence interval, consisted of the following components: transducer spacing measurements (0.1%), pipe cross section area measurements (0.2%), statistical uncertainty due to data point scatter (0.2%), uncertainty in time delay calculations due to electronics and calculation algorithm (0.14%), and repeatability (0.25%). These uncertainty components are considered independent, and according to accepted standards in flow measurement uncertainty

calculation [50], total uncertainty was calculated as a square root of the sum of quares of individual components. As a result, total 95% confidence interval uncertainty of C is 0.73%, as shown below.

$$\sqrt{0.6\%^2 + 0.1\%^2 + 0.2\%^2 + 0.2\%^2 + 0.14\%^2 + 0.25\%^2} = 0.73\% \qquad (4.3)$$

Chapter 5

Numerical Simulation and Laboratory Test Results

Numerical simulations were conducted for all flow conditions studied in the experimental investigation, using the numerical simulations developed as part of this work and presented in Chapter 3. Commercially available Reynolds-averaged-Navier-Stokes (RANS) simulations, based on the $k-\epsilon$ model, were also conducted, of the flow conditions used in the experimental investigation described in Chapter 4, in order to obtain axial flow profiles used to calculate input in the numerical simulation. Figure 5.1 shows a RANS simulations of the AMAG flow loop.

The laboratory tests included nine locations downstream of a 90-degree elbow, and different transducer spacings at those locations. Results obtained from the numerical simulations were compared to experimental results. The purpose of these comparisons is to validate the mathematical model of cross correlation flow measurement developed as part of this work and presented in Chapter 2. Throughout this chapter, the term *simulation* is used to refer to the simulations developed as part of this project, not the RANS simulations, unless otherwise specified.

The flow rate was 4.63 m/s. The measurement locations are indicated by their distance from the upstream 90-degree bend, and are 6D, 9D, 12D,

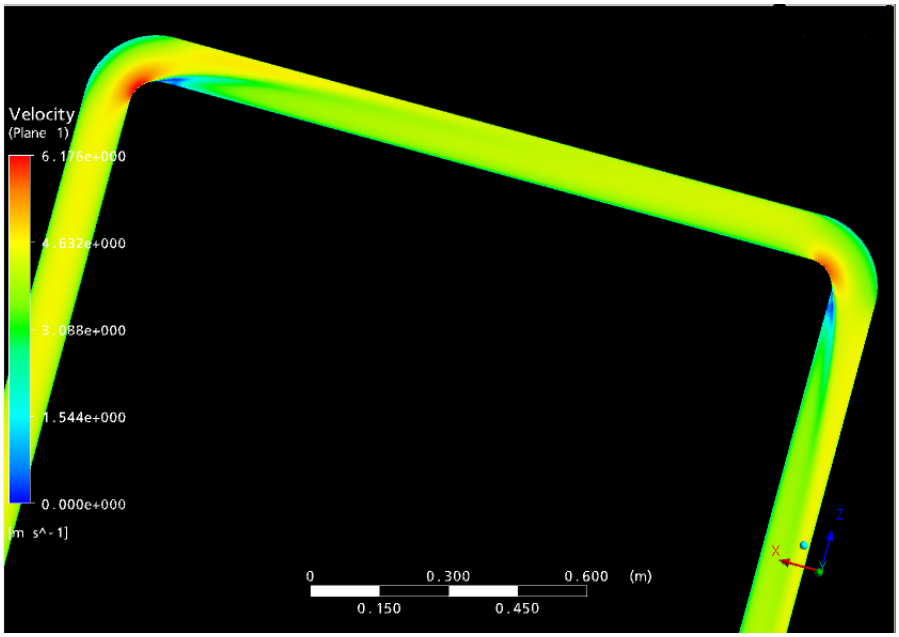

Figure 5.1: RANS simulation of AMAG flow loop, showing time-averaged velocity. Section between two bends upstream of test section shown. Flow moving clockwise.

15D, 20D, 25D, 30D, 42D, and 50D, where D is the pipe inner diameter of 0.1 meters. A measurement at 12D, for example, is a measurement where the midpoint between the locations of the upstream and downstream ultrasonic beams is 1.2 meters downstream of the upstream 90-degree bend. Due to different velocity distributions in the pipe at different distances from the bend, each measurement location corresponded to a different flow condition. Measurements were conducted using three different transducer spacings at the same angular orientation. The transducer spacings were 0.63D, 1.114D, and 3.18D. These transducer spacings are referred to in this thesis as 0.5D, 1D, and 3D spacing tests. More details on the laboratory testing can be found in Chapter 4 of this report.

One of the inputs for the numerical simulation is the angular average axial flow profile. The simulation input was a flow profile following the formula $U(r) = U_{max}(1 - \frac{r}{R})^{1/n}$ as presented in Chapter 3 of this report, where r is location along the pipe radius, R is the pipe inner radius, n is flatness of the flow profile, and U_{max} is the flow rate at the center of the pipe [102]. The values of U_{max} and n were determined with the use of commercially available RANS simulations of the laboratory setup, based on the $k - \epsilon$ model, conducted as part of this work. The flow profile along the pipe diameter perpendicular to the plane of the 90-degree bend was calculated for all measurement locations using RANS simulations, and the average velocity along each of these profiles was calculated. The pipe diameter perpendicular to the plane of the 90-degree bend was used, because it yields a symmetrical flow profile. The average flow along a pipe diameter is typically larger than the cross section average flow rate. Also, the cross section average flow rate remains constant for all locations due to conservation of mass and constant pipe inner diameter, but average flow along a pipe diameter depends on axial flow profile along that diameter. For the numerical simulation input, U_{max} was chosen such that the cross section average flow rate would equal the flow rate of the actual flow, and n was chosen such that the average velocity along the diameter of the input flow profile was equal to the average velocity along the diameter of the RANS simulated flow profile for that location. The power spectrum used as input for the numerical simulations was taken from

the real flow measurements at the simulated location.

Although the cross correlation flow meter was used to obtain power spectrums that were used to simulate cross correlation flow measurement, the comparison of measured flow velocity and simulated flow velocity is still independent, because the normalized demodulated signal is a property of the flow, not the meter, and is used by both the simulation and the meter in different ways, in order to obtain a simulated flow velocity and a measured flow velocity. The nature of the comparison, is whether the numerical simulation predicts the behavior of the flow meter, when both the numerical simulation and the flow meter are given the same power spectrum, and hence the same flow, as input. The power spectrum acts only as an indicator of the turbulent picture inside the pipe for both the simulation and the flow meter. Processing of the power spectrum by the flow meter, and the processing of the power spectrum by the numerical simulation, are independent.

Below, experimental and simulated results are shown. Specifically, the results shown are for testing using the orientation within the plane of the 90-degree bend, with 0.5D, 1D, and 3D transducer spacings. The results below are for the measurement locations of 12D, 20D, 30D, 42D, and 50D. Results from measurement locations at 6D and 9D are not presented in this thesis, for the following reasons: Typical industrial cross correlation flow measurement installations are 15D from an upstream bend or farther. Also, at 6D and 9D from an upstream bend, the radial and angular time averaged velocity components are not negligible, and therefore these location do not fit the approximations made in the numerical simulation. Results from the measurement locations at 15D and 25D are not presented in the thesis, because they are very consistent with trends observed in presented results.

The flow profile flatness values, n, used for the numerical simulations for these measurement location were 57, 20, 15.5, 12, and 10 for the measurement locations of 12D, 20D, 30D, 42D, and 50D respectively. The shape of the input flow profiles, representing angular averaged time averaged axial flow profiles, coincided well with the shape of the RANS simulated axial flow

profiles used to determine n. Although the numerical simulations are based on a double radial-angular integral, and the experimental results are based on a single beam, hence a single radial integral, the comparison is still valid, because tests conducted with multibeam transducers demonstrated that the hydraulic factor dependence on angular orientation is within the uncertainty of the laboratory testing.

5.1 Location and Spacing dependence

The figures below compare experimental measurement results to simulated measurement results. Rather than plotting measured velocity, the figures plot hydraulic factor, $C = V_a/V_m$, where V_a is the cross section average flow velocity of 4.63, and V_m is the average measured velocity, either experimentally measured or simulated. Recall, the simulations are intended to simulate measurement, and are expected to predict measured flow velocity V_m . The purpose of the simulations is to predict the hydraulic factor, and its sensitivity to flow conditions and design parameters of the meter. In the work presented in this thesis, the flow conditions were different distances from the upstream bend, and the design parameters of the meter were different transducer spacings. Hence, a positive results is one for which the simulated results give a C values close to that given by the experimental results.

There are 30 simulated measurement points and approximately 30 experimental measurement points for each of the various combinations of flow locations and transducer spacings presented in this section. Although every location and transducer spacing had approximately 700 measured points, only 30 are shown for simplicity. The initial 30 points are representative of all approximately 700 points for all cases. For determining power spectrum for numerical simulation input, all approximately 700 measurement points were used for every location. The reason there are exactly 30 simulated points shown, but approximately 30 experimental points shown, is because due to the nature of turbulence and cross correlation flow measurement, occasional flow measurement attempts do not produce a cross correlation curve with a

distinguishable peak rising above background noise. Such cross correlation curves, and the associated measurement points, are rejected based on criteria built into the cross correlation flow meter software and defined prior to flow measurement. These rejections are conducted in order to ensure that chaotic effects that do not represent pipe flow, but may effect flow measurement, do not skew the measurement results. Such effects include electronic noise, pipe vibrations, and instances of turbulent pictures that do not remain recognizable after traveling between ultrasonic beams. These rejected points are not shown in the figures below.

The 30 simulated points are all different, because different random phase shifts in the phase-correlation function $\theta_j(y)$ were used in the simulation process, mimicking the scatter of cross correlation flow measurement. The turbulent picture is different every instance in time, but the average characteristics remain the same. As a result, measured velocity is different every instance in time, but remains around the same average value. Laboratory test measurements used a sample frequency of 4096 Hz, and the numerical simulations used a sample frequency of 50,000 Hz. For this reason, in the plots below, measured results may appear to take more discrete values, compared to the simulated results. Increasing the sample frequency from 4096 yields more possible measured values, and hence less discrete looking measurement results. All flow measurements and simulations shown below use the same frequency filter, with high-pass 25Hz and low-pass 50Hz.

The purposes of the development of this model is to create a tool capable of studying the sensitivity of cross correlation flow measurement to various flow parameters and meter design parameters. In order to validate this model, cross correlation flow measurement dependence on transducer spacing and flow condition (where flow condition is defined by axial flow profile and power spectrum) is predicted by the model, and compared with experimental results. Asymptotic analysis of the model, and sensitivity of the model to various other input parameters, is a subject of future investigation.

It is expected, that as transducer spacing increases, turbulent structures

will deform more between upstream and downstream beams due to the non-uniformity of the axial flow profile. Since the center of the pipe has the most uniform section of the axial flow profile, it is expected that a greater transducer spacing will yield simulated measurements more bias towards the higher flow velocities at the center of the pipe, and hence lower hydraulic factor C, as is observed in real cross correlation flow measurement. Also, since time and angular averaged axial flow profile is more uniform at locations closer to the upstream bend, it is expected that simulated measurements closer to the upstream bend will be less bias towards higher flow velocities at the center of the pipe, and will therefore yield hydraulic factors C closer to 1.

Figures 5.2-5.6 plot Hydraulic Factor C for the five different locations. The transducer spacing used is 0.5D. Experimental results are represented by blue circles, and simulated results are represented by red stars.

Figures 5.7-5.11 plot Hydraulic Factor C for the five different locations and a transducer spacing of 1D. Experimental results are represented by blue circles, and simulated measurements are represented by red stars.

Figures 5.12-5.16 plot Hydraulic Factor C for the five different locations and a transducer spacing of 3D. Experimental results are represented by blue circles, and simulated measurements are represented by red stars.

Figures 5.17-5.19 show three graphs, depicting the average measured hydraulic factors, and average simulated hydraulic factors, for the three different transducer spacings, as a function of distance from the upstream bend.

Figure 5.20-5.24 show five graphs, depicting the average measured hydraulic factors, and average simulated hydraulic factors, for the five different distances from the upstream bend, as functions of transducer spacing.

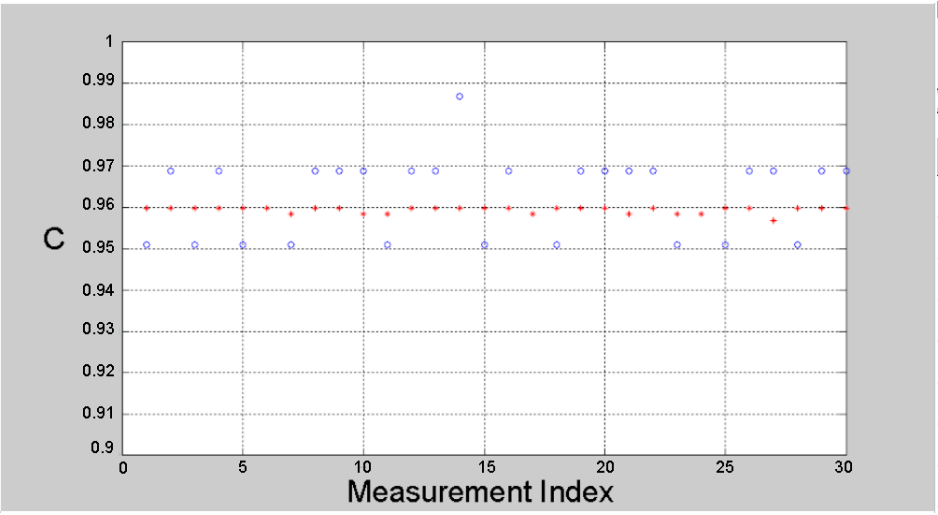

Figure 5.2: Hydraulic Factor is on the vertical axis, and measured and simulated points are along the horizontal axis. Measured points are represented by blue circles, and simulated points are represented by red stars. The measurement location is 12D from the upstream 90-degree elbow, and transducer spacing is 0.5D, where D is the pipe inner diameter of 0.1m.

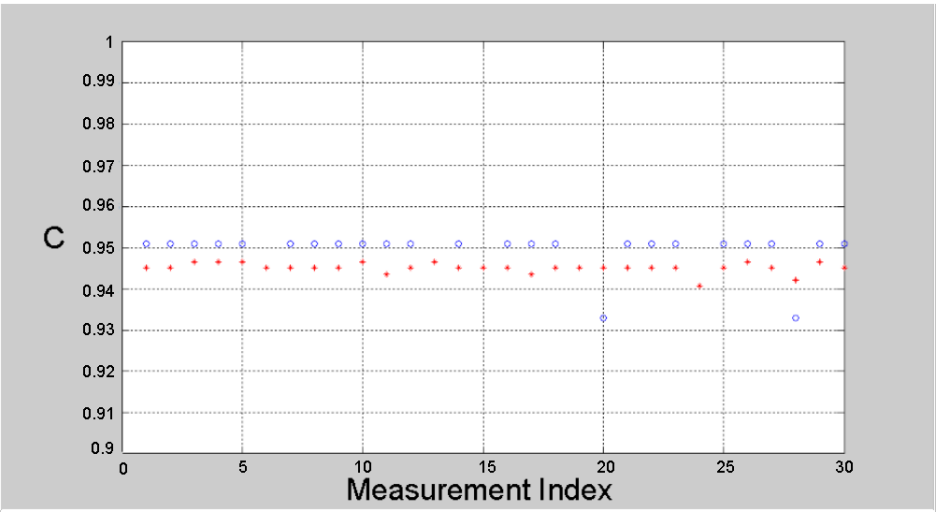

Figure 5.3: Hydraulic Factor vs measured and simulated velocity, as in Figure 5.2. The measurement location is 20D from the upstream 90-degree elbow, and transducer spacing is 0.5D.

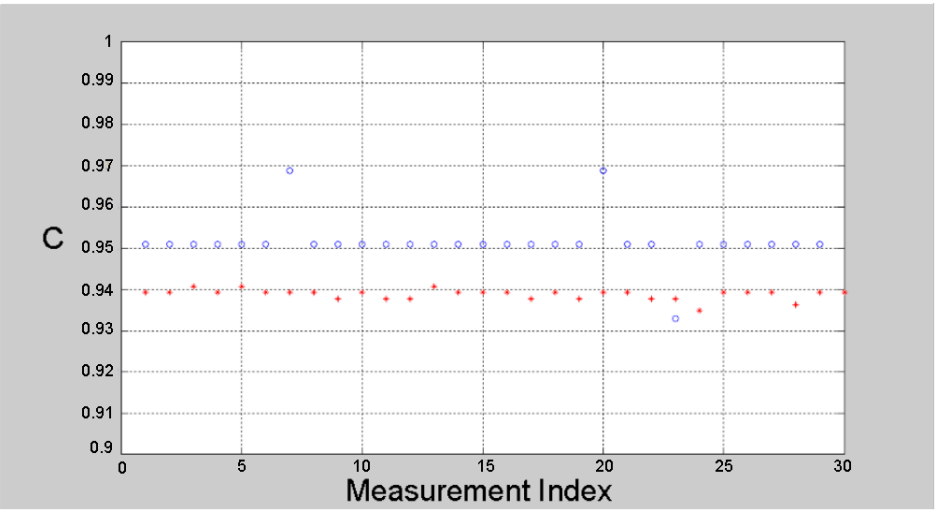

Figure 5.4: Hydraulic Factor vs measured and simulated velocity, as in Figure 5.2. The measurement location is 30D from the upstream 90-degree elbow, and transducer spacing is 0.5D, where D is the pipe inner diameter of 0.1m.

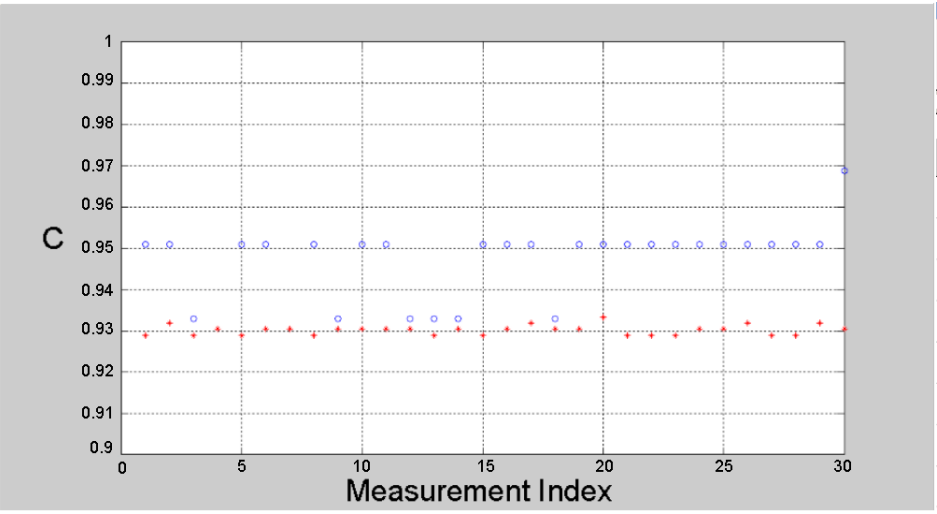

Figure 5.5: Hydraulic Factor vs measured and simulated velocity, as in Figure 5.2. The measurement location is 42D from the upstream 90-degree elbow, and transducer spacing is 0.5D, where D is the pipe inner diameter of 0.1m.

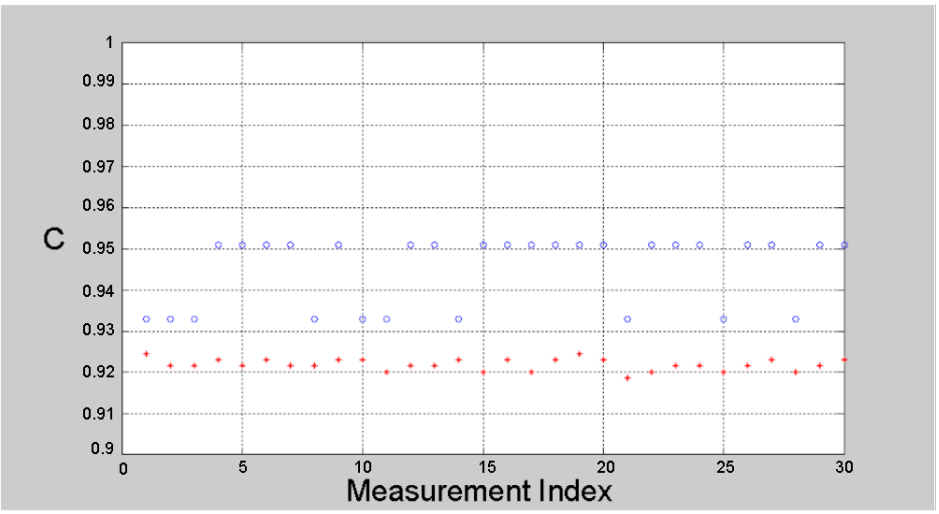

Figure 5.6: Hydraulic Factor vs measured and simulated velocity, as in Figure 5.2. The measurement location is 50D from the upstream 90-degree elbow, and transducer spacing is 0.5D, where D is the pipe inner diameter of 0.1m.

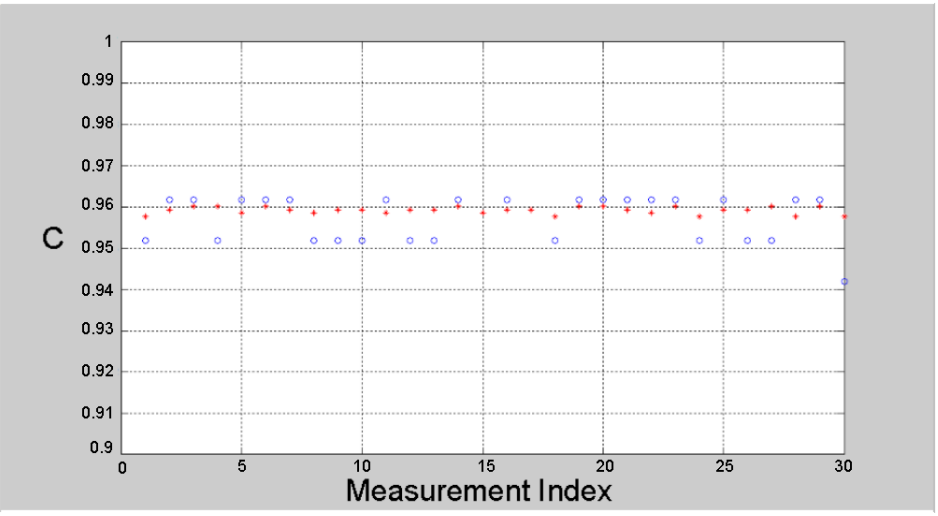

Figure 5.7: Hydraulic Factor vs measured and simulated velocity, as in Figure 5.2. The measurement location is 12D from the upstream 90-degree elbow, and transducer spacing is 1D, where D is the pipe inner diameter of 0.1m.

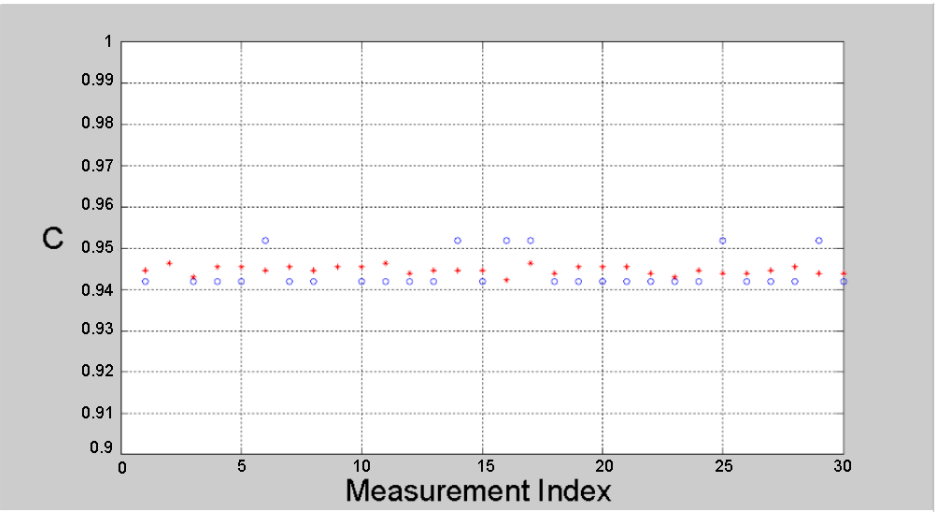

Figure 5.8: Hydraulic Factor vs measured and simulated velocity, as in Figure 5.2. The measurement location is 20D from the upstream 90-degree elbow, and transducer spacing is 1D, where D is the pipe inner diameter of 0.1m.

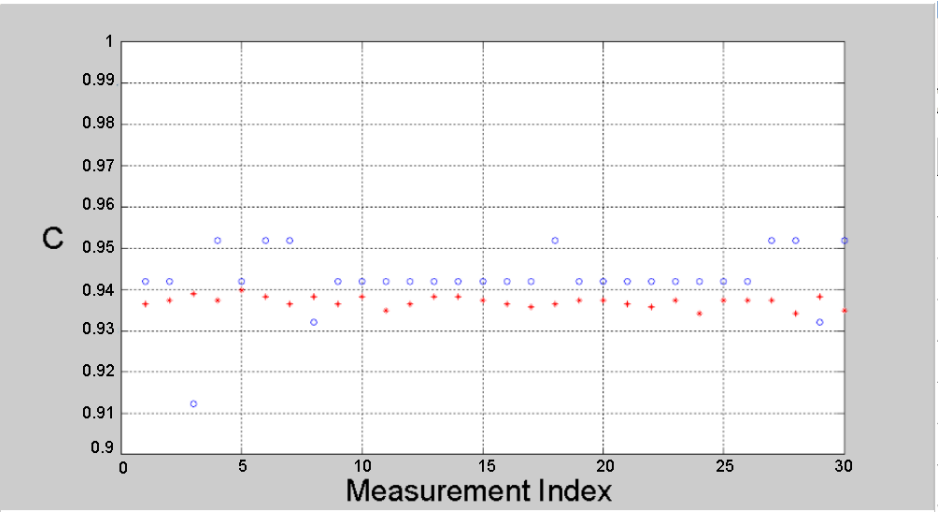

Figure 5.9: Hydraulic Factor vs measured and simulated velocity, as in Figure 5.2. The measurement location is 30D from the upstream 90-degree elbow, and transducer spacing is 1D, where D is the pipe inner diameter of 0.1m.

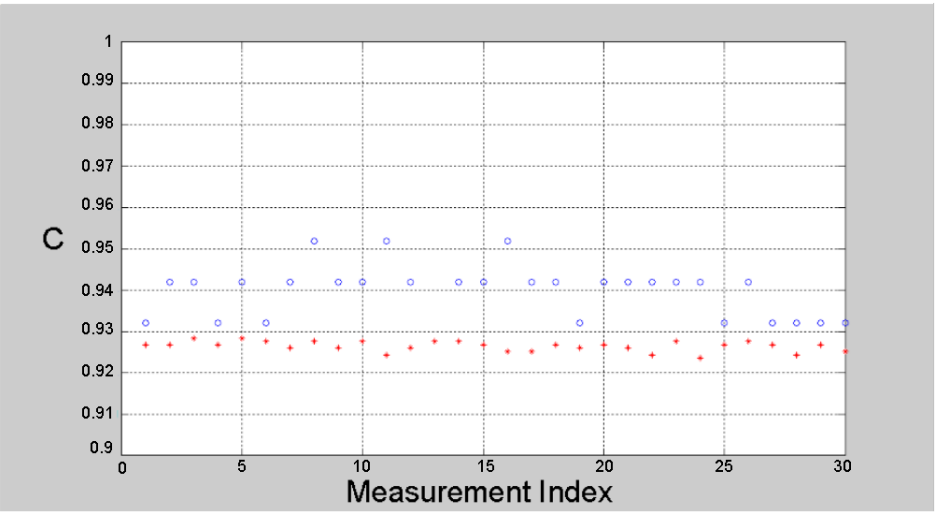

Figure 5.10: Hydraulic Factor vs measured and simulated velocity, as in Figure 5.2. The measurement location is 42D from the upstream 90-degree elbow, and transducer spacing is 1D, where D is the pipe inner diameter of 0.1m.

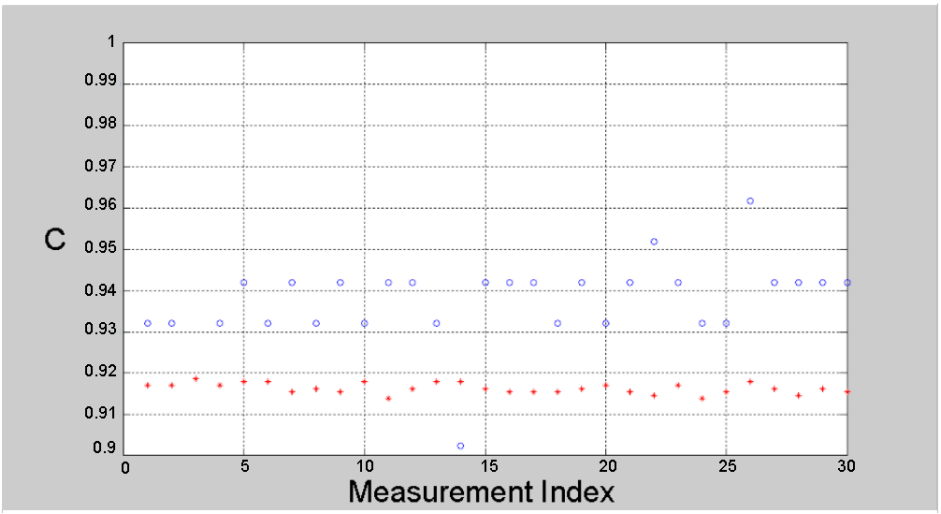

Figure 5.11: Hydraulic Factor vs measured and simulated velocity, as in Figure 5.2. The measurement location is 50D from the upstream 90-degree elbow, and transducer spacing is 1D, where D is the pipe inner diameter of 0.1m.

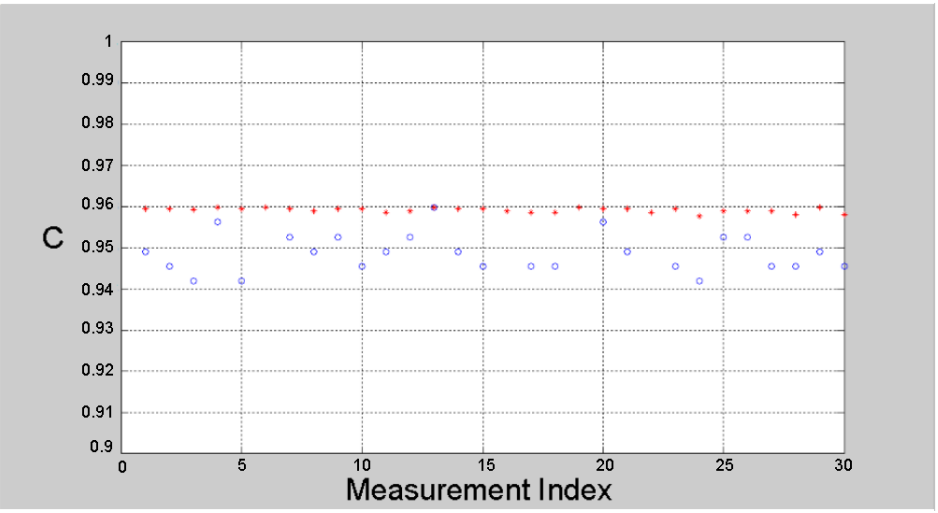

Figure 5.12: Hydraulic Factor vs measured and simulated velocity, as in Figure 5.2. The measurement location is 12D from the upstream 90-degree elbow, and transducer spacing is 3D, where D is the pipe inner diameter of 0.1m.

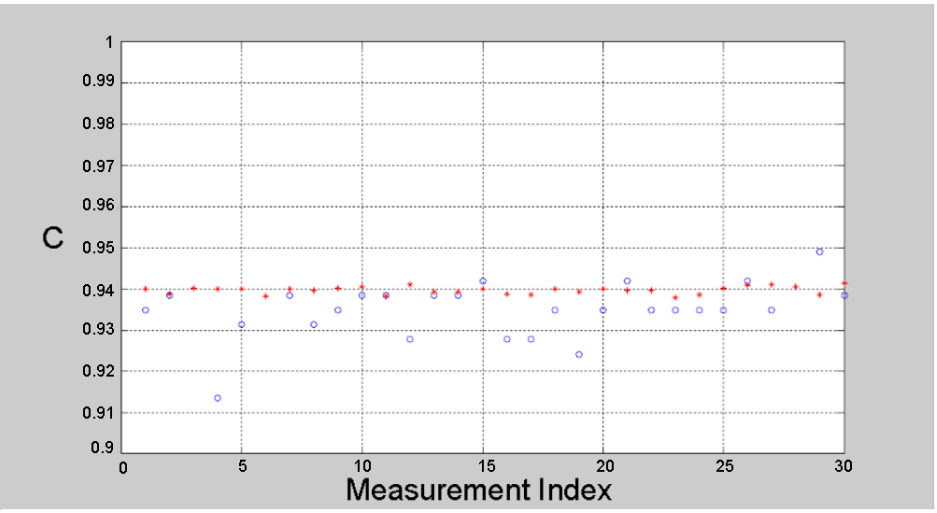

Figure 5.13: Hydraulic Factor vs measured and simulated velocity, as in Figure 5.2. The measurement location is 20D from the upstream 90-degree elbow, and transducer spacing is 3D, where D is the pipe inner diameter of 0.1m.

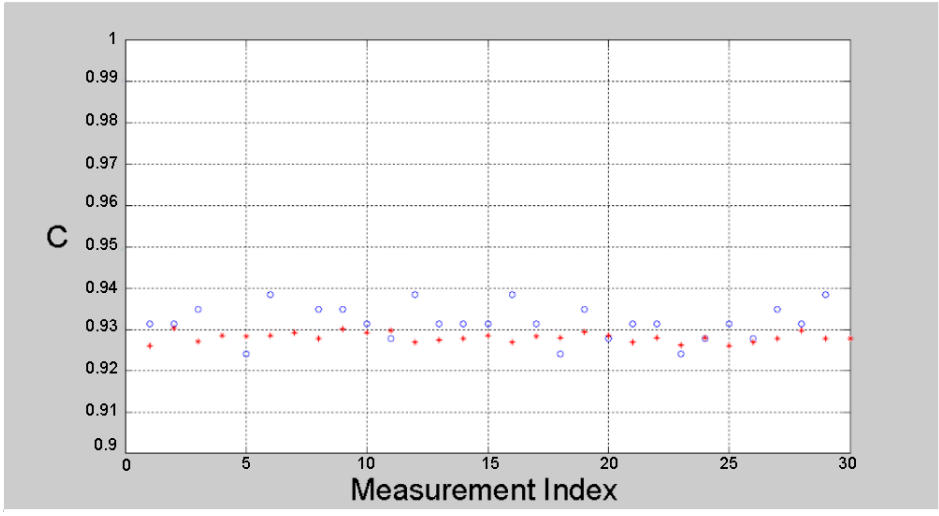

Figure 5.14: Hydraulic Factor vs measured and simulated velocity, as in Figure 5.2. The measurement location is 30D from the upstream 90-degree elbow, and transducer spacing is 3D, where D is the pipe inner diameter of 0.1m.

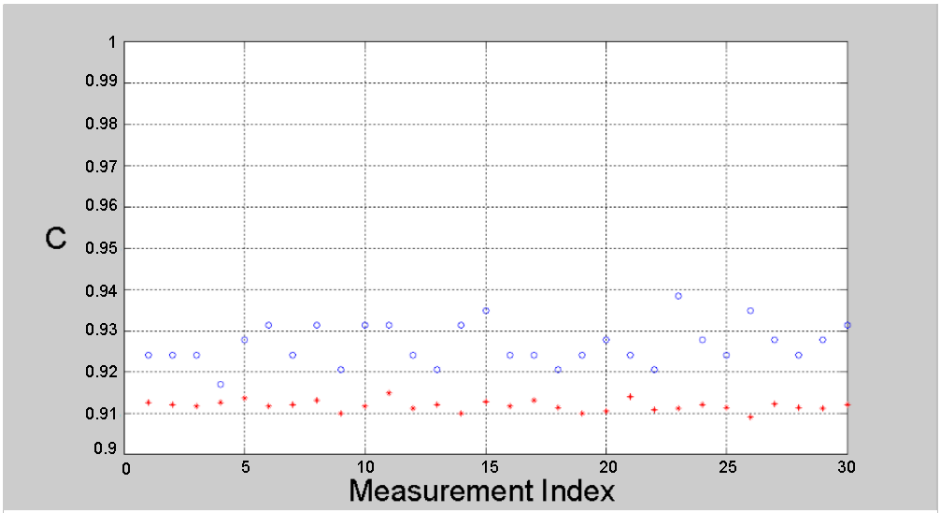

Figure 5.15: Hydraulic Factor vs measured and simulated velocity, as in Figure 5.2. The measurement location is 42D from the upstream 90-degree elbow, and transducer spacing is 3D, where D is the pipe inner diameter of 0.1m.

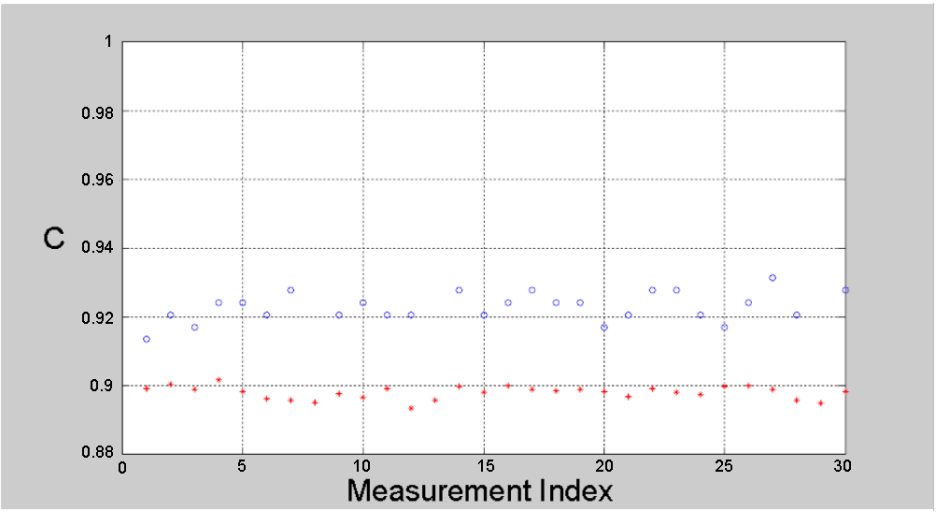

Figure 5.16: Hydraulic Factor vs measured and simulated velocity, as in Figure 5.2. The measurement location is 50D from the upstream 90-degree elbow, and transducer spacing is 3D, where D is the pipe inner diameter of 0.1m.

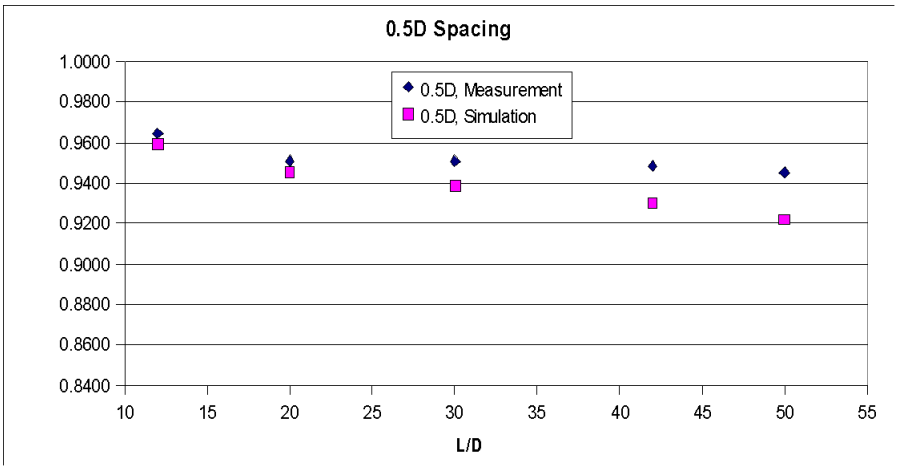

Figure 5.17: Simulated and measured hydraulic factor (C), as a function of distance from upstream bend normalized to pipe diameter (L/D), for 0.5D transducer spacings.

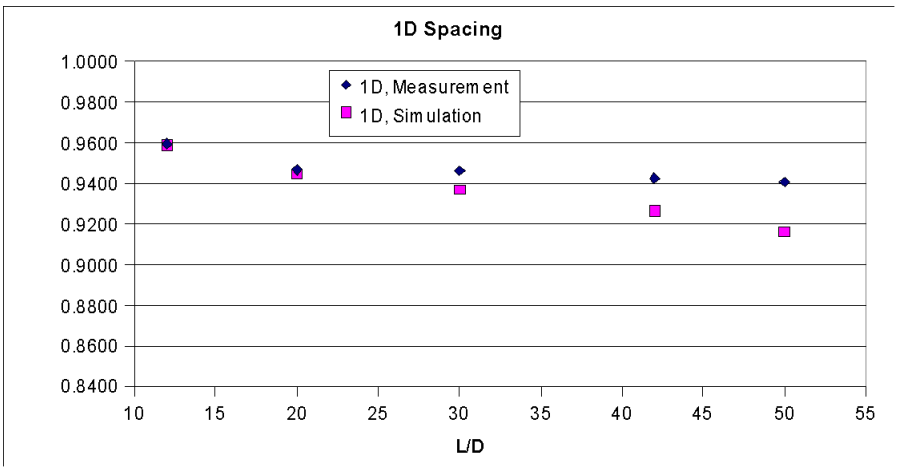

Figure 5.18: Simulated and measured hydraulic factor (C), as a function of distance from upstream bend normalized to pipe diameter (L/D), for 1D transducer spacings.

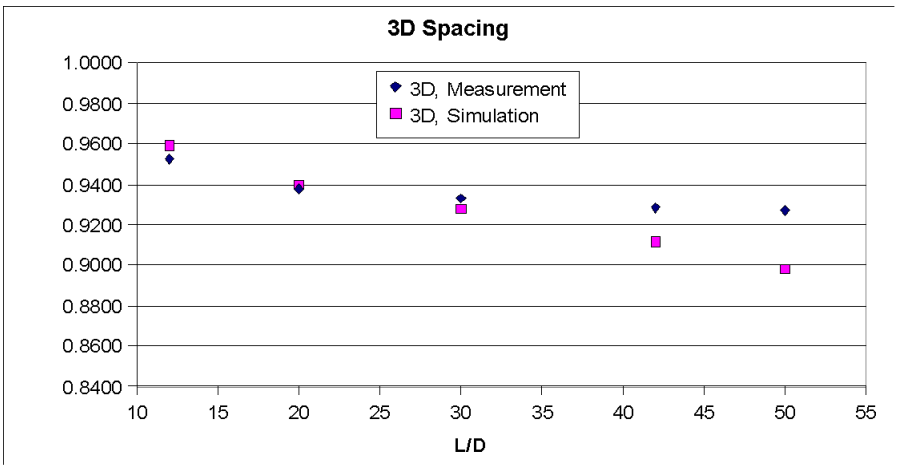

Figure 5.19: Simulated and measured hydraulic factor (C), as a function of distance from upstream bend normalized to pipe diameter (L/D), for 3D transducer spacings.

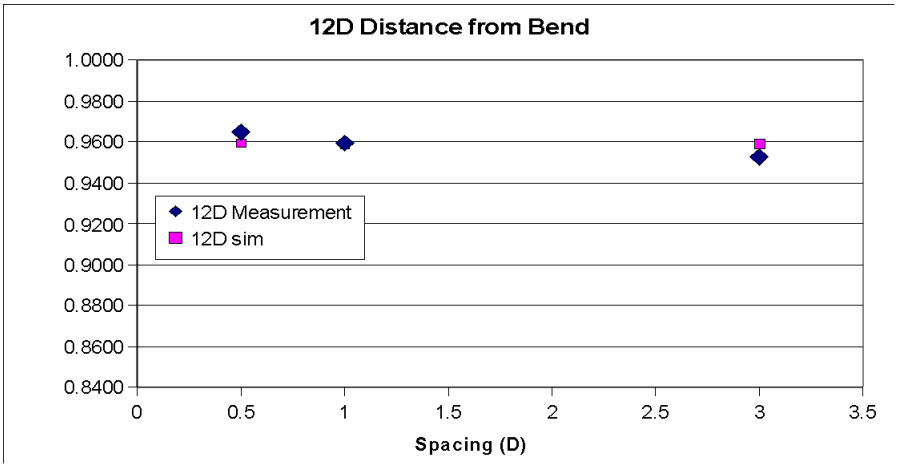

Figure 5.20: Simulated and measured hydraulic factor (C), as a function of transducer spacing, for distances 12D from the upstream bend.

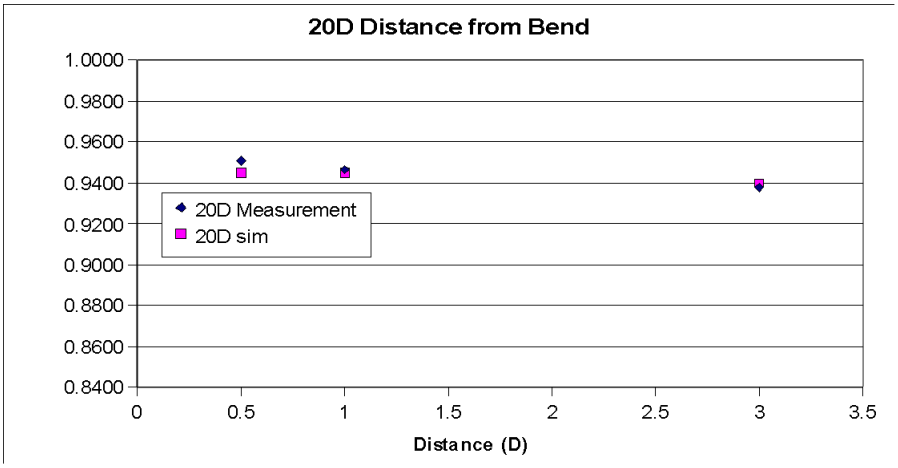

Figure 5.21: Simulated and measured hydraulic factor (C), as a function of transducer spacing, for distances 20D from the upstream bend.

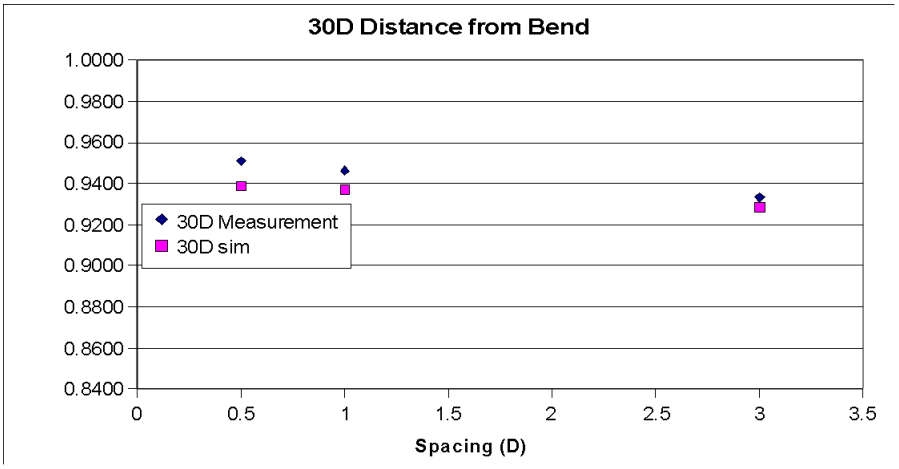

Figure 5.22: Simulated and measured hydraulic factor (C), as a function of transducer spacing, for distances 30D from the upstream bend.

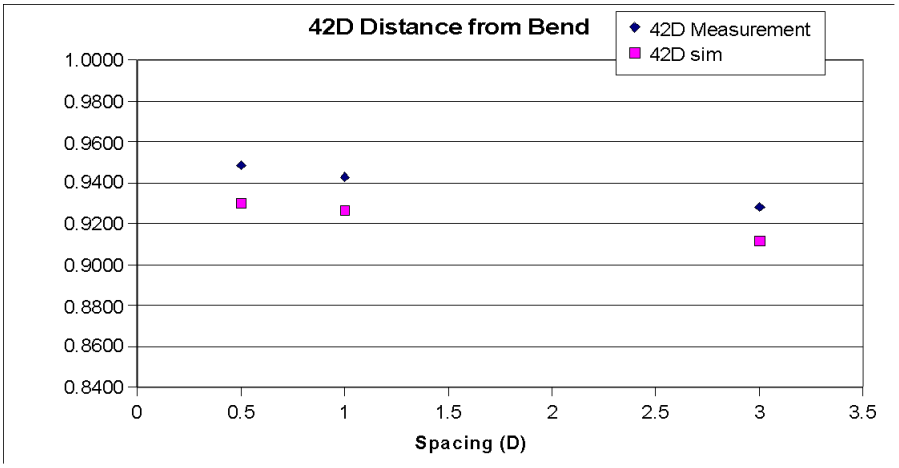

Figure 5.23: Simulated and measured hydraulic factor (C), as a function of transducer spacing, for distances 42D from the upstream bend.

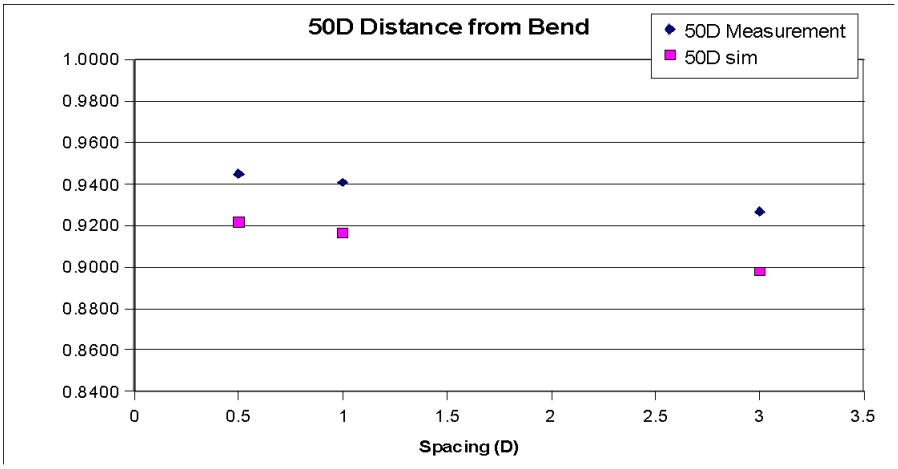

Figure 5.24: Simulated and measured hydraulic factor (C), as a function of transducer spacing, for distances 50D from the upstream bend.

Figure 5.25 depicts a chart that demonstrates the sensitivity of the model to time and angular averaged axial flow profile and to power spectrum. Columns along the horizontal direction represent different flow profile flatness values, n. Rows along the vertical direction represent different power spectrums labeled by the distance from the upstream bend, of the location where the power spectrum was taken from. The bottom row represents a power spectrum taken at 20D downstream of a 90-degree bend, from a different flow laboratory with a similar piping configuration but with a different flow rate and a different pipe. The purpose of this last row is to observe model behavior if numerical simulations are conducted using an input of a power spectrum unrelated to the simulated flow. The cells in the chart indicate hydraulic factor, where 4.63 m/s is taken as the cross section average flow velocity in every case, including the bottom row where the power spectrum comes from a flow condition with different flow velocity. Transducer spacing is 1D for all cases.

The results in Figure 5.25 suggest, that when modeling different locations along the same flow loop, power spectrum has very little effect on hydraulic factor, and axial flow profile has significant effect. When using a spectrum unrelated to the modeled flow, though, as is the case for the bottom row, the

	Flatness, n = 57	Flatness, n = 20	Flatness, n = 15.5	Flatness, n = 12	Flatness, n = 10
	Corresponding to 12D	Corresponding to 20D	Corresponding to 30D	Corresponding to 42D	Corresponding to 50D
Power Spectrum at 12D	0.9538	0.9390			
Power Spectrum at 20D	0.9529	0.9380	0.9306		
Power Spectrum at 30D		0.9371	0.9297	0.9186	
Power Spectrum at 42D			0.9306	0.9186	0.9065
Power Spectrum at 50D				0.9186	0.9065
Unrelated power spectrum	0.9501	0.9417	0.9343	0.9269	0.9186

Figure 5.25: Model sensitivity to averaged axial flow profile and power spectrum.

sensitivity to power spectrum becomes significant. Therefore, sensitivity to axial flow profile is significantly greater than sensitivity to power spectrum, but sensitivity to power spectrum is not negligible, and a power spectrum input representative of the modeled flow must be used.

5.2 Discussion of Results

Overall, there are several conclusions one can reach from the results presented in Section 5.1.

1. For all locations, simulated results predict experimental results to within 3.18%. On average, the difference between simulated and experimental results was 1.14%. This demonstrates the validity of the mathematical model. Predicting hydraulic factor to within 3.18% is very good agreement for such numerical simulations. Although industry requirements for measurement uncertainty are of order 0.5%, simulations predicting hydraulic factor to within 3.18% are very sufficient for designing and optimizing laboratory testing, optimizing cross correlation flow meter design and operation, and demonstrating traceability of industrial conditions to laboratory conditions.

2. Hydraulic factor dependence on transducer spacing, demonstrated the same trends in experimental and simulated results. Both simulated and

experimental results show greater sensitivity to spacing at locations farther from the upstream bend. Both simulated and experimental results also show lower C for greater spacing. For example, on a distance of 50 pipe diameters from the upstream bend, when changing spacing from 0.5 pipe diameters to 3 pipe diameters, simulated C drops from 0.9219 to 0.8980 and experimentally obtained C drops from 0.9451 to 0.9270. Thus, simulated C drops by 2.63%, and experimentally obtained C drops by 1.93%.

3. Hydraulic factor dependence on distance from an upstream bend, demonstrated the same trends in experimental and simulated results. Both simulated and experimental results shown lower C for measurement locations farther from an upstream bend. However, simulated results are more sensitive than experimental results, to distance from an upstream bend. For example, moving from 12 pipe diameters to 50 pipe diameters from an upstream bend, with spacing 1 pipe diameter, experimentally obtained C drops from 0.9596 to 0.9408, and simulated C drops from 0.9591 to 0.9163. Thus, experimentally obtained C drops by 1.98%, and simulated C drops by 4.56%.

4. Since the flatness of the shape of the time and angular averaged axial flow profiles in the simulation were determined using the RANS simulations based on the $k-\epsilon model$, it is in the opinion of the author that one could not expect the simulated results to be closer to measured results than they are. By predicting quantitative properties to within 3%, and by accurately predicting trends related to measurement location and transducer spacing for all situations, the simulations demonstrate the strength of the mathematical model developed in this work. Since the axial flow profile is the dominant flow property effecting the hydraulic factor, and the numerical simulations are weakly dependant on which location along the pipe the power spectrum was taken from, it is reasonable to hypothesize, that if the flatness of the shape of the time and angular average axial flow profiles in the simulation were deter-

mined using a method more accurate than RANS simulations based on the $k - \epsilon$ model, quantitative results given by the mathematical model would predict measured results to within less than 3%.

Chapter 6

Conclusion

1. The operating principals of ultrasonic cross correlation flow measurement are based on the transport of turbulent structures along the flow. Previously developed mathematical models are based on assumptions regarding turbulent flow, without the presence of rigorous analysis justifying those assumptions. In the work presented in this thesis, an original mathematical model of cross correlation flow measurement was developed, based on rigorous analysis of space-time development of a velocity field and vorticity field in turbulent flow. This model describes the effect of flow conditions on cross correlation flow meter output. Laboratory testing was conducted to validate the model. Results of numerical simulations based on the model were in good agreement with laboratory test results.

2. The following results were obtained through theoretical analysis in this work:

   It was obtained from order of magnitude analysis, that for a turbulent flow with a dominant time-averaged flow direction, such as channel flow, the space time development of the vorticity field is described by a simple equation, according to which, vorticity remains constant while moving along time averaged velocity streamlines in the dominant flow direction. This can be characterized as a locally frozen vorticity ap-

proximation. This approximation is valid for distances much greater than the spacial scale of turbulence.

Using the locally frozen vorticity approximation, the simplified case of turbulent flow in infinite two dimensional space was considered. For this case, an exact analytical solution was obtained, for calculating a particular integral characteristic of a turbulent velocity field. The signal collected by the cross correlation flow meter is proportional to this integral characteristic. Thus, a direct relation between the cross correlation flow meter signal, and turbulent flow conditions, was obtained. This relation clearly reveals the physical phenomena governing cross correlation flow meter behavior.

For the general case of three dimensional turbulent flow, a fundamental vector field relation was used to derive an equation relating the velocity field to the vorticity field, if vorticity is described by the locally frozen vorticity approximation. According to this equation, the turbulent velocity field is not described by an analogous locally frozen velocity approximation, unless time-averaged flow velocity is constant in space. If time-averaged flow velocity is not constant, quantitative parameters may be obtained, that describe the spacial scale for which a locally frozen velocity approximation is applicable.

For the case of pipe flow, it was shown, that although the locally frozen velocity approximation does not describe the space-time development of the velocity field, it does describe certain integral characteristics of the velocity field. These integral characteristics are directly related to the signal collected by the cross correlation flow meter.

3. Cross correlation flow measurement is based on detecting certain integral characteristics of the turbulent velocity field at two pipe cross sections, separated by a distance of order magnitude of the pipe diameter. The theoretical analysis developed in this work, allows for

calculation of these integral characteristics at both cross section, if the angular-averaged turbulent velocity field and the time-averaged velocity distribution at one of the cross sections is known. To implement these theoretical results into a mathematical model, the following steps were taken in this work:

An original equation describing an angular-averaged turbulent velocity field, as a function of time and radial position at one pipe cross section, was developed. A number of free parameters in this equation allow for the generation of a turbulent velocity field with desired statistical characteristic. These characteristics include spacial and temporal turbulent scales, spacial distribution of the turbulence power spectrum, and space and time correlation of turbulent velocity.

A computer algorithm was developed to generate the turbulent velocity field described above, with desirable statistical characteristics.

Signals collected through cross correlation flow measurement allow for calculation of certain spectral characteristics of the turbulence in the real flow during flow measurement. The algorithm described above, allows for the use of these spectral characteristics, as input. When using such input, the generated turbulent velocity field will have statistical characteristics representative of the real flow condition that existed during measurement.

A computer algorithm was developed to calculated integral characteristics of the turbulent velocity field along a pipe, given an angular-averaged turbulent velocity field and the time-averaged velocity distribution at one pipe cross section. This algorithm, applied to a generated turbulent velocity field with real flow spectral characteristics as input, can be used to simulate cross correlation flow measurement for different flow conditions.

Commercially available Reynolds Averaged Navier-Stokes simulations were conducted, using the $k-\epsilon$ model, to obtain the time-averaged velocity distribution at various pipe cross sections of the piping configuration configuration used in laboratory testing to validate the mathematical model.

4. Laboratory testing to validate the developed mathematical model was conducted at Advanced Measurement and Analysis Group Inc. (AMAG) laboratory in Canada. A flow loop was designed and constructed as part of this work, with assistance from AMAG personnel. This flow loop had a test section consisting of a straight 240" run of 4" diameter pipe, following two in-plane 90-degree bends. Ultrasonic cross correlation flow meters, provided by AMAG, were modified to allow measurement with difference spacings between the two cross sections of measurement. The modified cross correlation flow meters were used to measure flow at various locations along the test section. Original computational tools were developed to analyze the test data. Computational simulations, based on the developed mathematical model, were conducted using spectral characteristics and time-averaged flow profiles corresponding to the locations of measurement along the test section. Since flow conditions are different at different distances from an upstream bend, these tests and simulations allowed for validation of the mathematical model.

5. Comparison of laboratory test results and simulations based on the mathematical model yielded the following results. These results were represented as the ratio between measured velocity (whether simulated measurements or real measurement) and cross section area average velocity. This ratio is represented by the letter C. Cross section average flow velocity was obtained using a reference meter in laboratory testing.

Results of simulated cross correlation flow measurement are in good agreement with laboratory test results. Considering all test conditions,

the difference between simulated C and experimentally obtained C did not exceed 3.18%, and on average, experimental and simulated results differed by 1.14%. Such agreement between simulated and experimental results, are very sufficient for using the mathematical model and simulation method for designing and optimizing cross correlation flow meters, designing and optimizing laboratory testing, and demonstrating traceability of industrial conditions to laboratory conditions.

Simulated and experimental results demonstrated the same trends in dependence on spacing between ultrasonic beams. Greater sensitivity to spacing at locations farther from the upstream bend, and lower hydraulic factor C for greater spacing, was observed in both experimental and simulated results. For example, at the measurement location of 50 pipe diameters from the upstream bend, changing spacing from 0.5 pipe diameters to 3 pipe diameters, results in simulated hydraulic factor C changes from 0.9219 to 0.8980 (a change of 2.63%), and experimentally obtained hydraulic factor C changes from 0.9451 to 0.9270 (a change of 1.93%).

Simulated and experimental results demonstrated the same trends in dependence on distance from an upstream bend. Lower hydraulic factor C was observed at measurement locations farther from an upstream bend, in both simulated and experimental results. However, simulated results are more sensitive to distance from an upstream bend than experimental results are. For example, as the measurement location changes from 12 pipe diameters to 50 pipe diameters from an upstream bend, with spacing 1 pipe diameter, experimentally obtained hydraulics factor C changes from 0.9596 to 0.9408, and simulated hydraulic factor C changes from 0.9591 to 0.9163. Thus, where experimentally obtained hydraulic factor C drops by 1.98%, simulated hydraulic factor C drops by 4.56%.

Sensitivity study of the model suggests that the model is signifi-

cantly sensitivity to axial flow profile, and is not significantly sensitivity to the location along the pipe run from which the power spectrum was obtained. Sensitivity to power spectrum is still significant, though, and the power spectrum used as input must be representative of the pipe run that is being modeled. The user may have the freedom to use the power spectrum from one pipe location to model cross correlation flow measurement at all locations along the same pipe run, without significant change in results, but using a power spectrum from a different pipe or piping configuration would yield significantly different results.

The cross correlation of received ultrasonic signals obtained at upstream and downstream cross sections, regularly has a similar shape in experimental and simulated results.

6. As a result of the work presented in this thesis, a set of tools has been developed, capable of studying the effect of different flow conditions on cross correlation flow meter behavior. This set of tools is currently being used for optimization and improvement of cross correlation flow measurement technology. Also, work is being conducted on combining these tools with cross correlation flow measurement technology, to study turbulent flow in general. Work is also being conducted to expand these tools to applications involving more complicated flow conditions, such as significant swirl.

Results obtained during this project were presented and discussed in AMAG technical meetings. Some of the results have been presented in a number of conferences and published in conference proceedings [103-106].

Future Work

Further investigations based on the results obtained in this work, may fall into four categories.

1. Using the developed model in order to conduct detailed analysis of the effect of various factors on cross correlation flow measurement (sensitivity analysis). These factors include turbulent flow characteristics and flow meter design. Results of this analysis can be used for the following:

   As a basis for uncertainty analysis under various specific flow measurement conditions.

   For providing traceability of field measurements to laboratory calibration, by designing laboratory test conditions representative of the field conditions.

   For optimization of cross correlation flow meter deign and measurement procedures.

2. Further validation of the model using large eddy simulation.

3. Further development and validation of the model, for flow conditions involving intensive swirl, and local, non-angular averaged, correlations.

4. Exploring applications of the theoretical analysis to other phenomena involving space-time development of turbulent structures, such as transport of a tracer substance, or temperature disturbance, along a pipe.

References

References are listed below, in order of appearence in the text.

1. ZhaoYi Science and Technology Develop Ltd, A Brief History of Flow Measurements and Prospect, retrieved from http://www.zydc.com/en/showkfzx.asp?lm=469&ID=28 , 2010-05-02

2. Burkhardt, P., Alaska Pipeline Crude Oil Flow Rate Little Changed, retrieved from http://www.bloomberg.com/news/2011-01-18/alaska-pipeline-increases-crude-oil-flow-rate-as-stockpiles-drop-by-half.html, 2011-01-18

3. Novog, D.R., Yin, S.T., Chang, J.S., Recent Advances in High Heat Flux Smooth and Swirl Flow Boiling of Water, Fusion Science and Technology / Volume 52 / Number 4 / Pages 880-884, November 2007

4. Morreale, A.C., Novog, D.R., Determination of Operator Action Times During a Loss-of-Feedwater Event Using Extreme Value Statistics, Nuclear Science and Engineering / Volume 164 / Number 2 / Pages 151-161, February 2010

5. Miller, R., Flow Measurement Engineering Handbook [Hardcover] McGraw-Hill Professional; 3 edition (Mar 1 1996)

6. Rogers C. Baker, Flow Measurement Handbook, Industrial Design, Operating Principles, performance, and applications. Cambridge University Press, 2000.

7. Neumann, M., Shirai, K., Büttner, L., Czarske, J., A novel laser doppler array sensor for measurements of micro-scale velocity correlations in

turbulent flows, Flow Measurement and Instrumentation December 2012

8. Bengtson, H., Excel Spreadsheets for Orifice and Venturi Flow Meter Calculations, retrieved from http://www.engineeringexcelspreadsheets.com/2011/03/excel-spreadsheets-for-orifice-and-venturi-flow-meter-calculations/, March 2011

9. Merzkirch, W., Fluid Mechanics of Flow Metering, Springer – Verlag Berlin Heidelberg 2005

10. Brennan, J.A., McFaddin, S.E., Sindt, C.F., Kothari, K.M., The Influence of Swirling Flow on Orifice and Turbine Flowmeter Performance, Journal of Flow Measurement and Instrumentation, Volume 1, October, 1989.

11. Yeh, T.T., Mattingly, G.E., Ultrasonic Technology: Prospects For Improving Flow Measurement And Standards, 4th International Symposium on Fluid Flow Measurement (Denver, CO: NAFFMC 1999)

12. Mattingly, G.E., Yeh, T.T., NIST Industry-Government Consortium Research Program on Flowmeter Installation Effects: Summary Report with Emphasis on Research Period July-December, 1987, NIST 88-3898, Nov., 1988

13. Mattingly, G.E., Yeh, T.T., Flowmeter Installation Effects Due to Several Elbow Configurations., Proceedings of the 2nd International Symposium on Fluid Flow Measurement, pp. 271-283

14. Baker, R.C., Gautrey, D.P., Mahadeva, D.V., Sennitt S.D., Thorne, A.J., Case study of the electrical hardware and software for a flowmeter calibration facility, Flow Measurement and Instrumentation. March 2013

15. Rans, R., Sawcvhuk, B., Weiss, M., Flow Conditioning and Effects on Accuracy for Fluid Flow Measurement. 7th South East Asia Hydrocarbon Flow Measurement Workshop, 5th – 7th March 2008

16. Instrumart, Magnetic Flow Meters, retrieved from http://www.instrumart.com/pages/223/magnetic-flow-meters, May 2013

17. Lynnworth, L.C., 1979. Ultrasonic Flowmeters, Physical Acoustics–Principles and Methods, W.P. Mason and R.N. Thurston (Eds.), Academic Press 14:407-525.

18. Beck, M.S., Plaskowski, A., Cross Correlation Flowmeters, Their Design and Application Taylor & Francis; 1 edition (January 1, 1987)

19. Lynnworth, L.C., 1989. Ultrasonic Measurements for Process Control–Theory, Techniques, Applications, Academic Press.

20. Yeh, T.T., Espina, P.I., Special Ultrasonic Flowmeters for in-situ diagnosis of swirl and cross flow. Proceedings of the ASME FEDSM'01, 20012 ASME Fluid Engineering Division Summary Meeting, New Orleans, Luisiana, May 29-June 1, 2001

21. Mori, M., Tezuka, K., Tezuka, H., Furuichi, N., Kikura, H., and Takeda, Y., Industrial Application Experience of New Type Flow Metering System Based on Ultrasonic-Doppler Flow Velocity Profile Measurement. Third International Symposium on Ultrasonic Doppler Methods for Fluid Mechanics and Fluid Engineering EPFL, Lausanne, Switzerland, September 9-11, 2002

22. Wang, C., Meng, T., Hu, H., Zhang, L., Accuracy of the ultrasonic flow meter used in the hydro Stat turbine intake penstock of the Three Gorges Power Station, 15th International Flow Measurement Conference 2010 (FLOMEKO 2010) 13-15 October 2010, Taipei, Taiwan

23. Wang, Y., Temperature Compensation of Ultrasonic Flow Measurement Based on the Neural Network, Artificial Intelligence and Computational Intelligence, 2009. AICI '09. International Conference, 7-8 Nov. 2009, Volume: 3

24. Zheng, D., Zhang, P., Zhang, T., Zhao, D., A method based on a novel flow pattern model for the flow adaptability study of ultrasonic flowmeter. Flow Measurement and Instrumentation, March 2013

25. Witte, J., " Predicting Ultrasonic Meter Error in Dirty Service Conditions." Ceesi Ultrasonic flow meter workshop Colorado Springs, 2010

26. Drenthen, J.G., Kurth, M., den Hollander, H., van Klooster, J., & Vermeulen, M., Krohne. Reducing installation effects on ultrasonic flow meters, 7th International Fluid Flow Symposium, Anchorage 2009

27. Drenthen, J.G., Vermeulen, M., Kurth, M., & Hilko den Hollander Krohne Oil & Gas, Krohne: Ultrasonic flow meter diagnostics and the impact of fouling. AGA (American Gas Association) 2011 Operations Conference

28. Asher, R.C., Ultrasonic Sensors for Chemical Process Plant, Institute of Physics Publishing, London, 1997.

29. Lynnworth, L.C., and Mágori, V., 1999. Industrial Process Control Sensors and Systems, E. P. Papadakis (Guest Ed.), Ultrasonic Instruments and Devices: Reference for Modern Instrumentation, Techniques, and Technology, 23 in the series Physical Acoustics, Academic Press:275-470.

30. Liu, Y., et al. 1998. Buffer Waveguides for Flow Measurement in Hot Fluids, Ultrasonics, 36 (1-5):305-315.

31. Jen, C.K., et al. 1997. Clad Buffer Rods for In-situ Process Monitoring, Proc 1997 IEEE Ultrasonics Symp:801-806.

32. Foster. R., Ultrasonic Flow Measurement at Nuclear Power Plants, Flow Control Network, June 2001.

33. Flemons. R.S., Anew Non-intrusive Flowmeter., Proceedings, Symposium on Flow in Open Channels and Closed Conduits. Washington, DC: US Government. Printing Office (1977) pp 319-333

34. Sherin, J.R., Zobin, D., Feedwater Flow Measurement Using Ultrasonic Cross-Correlation Flow Meter. Nuclear Plant performance Seminar, Miami, Florida, February 24-25, 1992

35. Gurevich, Y., Lopez, A., Flemons, R., Zobin, D., Theory and application of non-invasive ultrasonic cross-correlation Flow Meter in harsh Environment. The 9th International Conference on Flow Measurement, FLOMEKO'98., Lund, Sweden, 1998.

36. Gajewski, J.B., Accuracy of Cross Correlation Velocity Measurements in Two-Phase Gas–Solid Flows, Flow Measurement and Instrumentation January 2013

37. Nor Ayob, N.M., Fazalul Rahiman, M.H., Zakaria, Z., Yaacob, S., and Abdul Rahim, R., Dual-Plane Ultrasonic Tomography Simulation Using Cross-Correlation Technique for Velocity Measurement in Two-Phase Liquid/Gas Flow, International Journal of electrical and electronic systems research, Vol.4, Jume 2011

38. Volker, H., Which Physical Quantity of Turbulent Structures Is Measured in Cross Correlation Flowmeters? XVII IMEKO World Congress Metrology in the 3rd Millennium, June 22-27, 2003, Dubrovnik, Croatia

39. Worch, "A clamp-on ultrasonic cross correlation flowmeter for one-phase flow", Meas. Sci. Technol., No. 9, 622-630, 1998

40. Gurevich, Y., Lopez, A., Askari, V., Safavi-Ardibili, V., Zobin, D., Performance Evaluation and Field Application of Clamp-On Ultrasonic Cross-Correlation Flow Meter, CROSSFLOW TM, The 5th International Symposium on Fluid Flow Measurement, Washington, DC, May 2002.

41. French, C, Peyvan, D., Gurevich, Y., In-Situ Calibrations for Feedwater Flow Measurement, Tenth International ASME Conference on Nuclear Engineering, Arlington, Virginia, USA , April 14-18, 2002

42. Gurevich, Y., Lopez, A., AMAG, Zobin, D., Performance Evaluation and Application of Clamp-On Ultrasonic Cross-Correlation Flow Meter

CROSSFLOW, Flow Measurement 2001 – International Conference, National Engineering Laboratory, East Kilbride, Glasgow, May 2001

43. Worch, A., A Clamp-on Ultrasonic Cross Correlation Flow Meter for One Phase Flows. Meas. Sci. Technol. 9 (1998) 622-630. Printed in UK

44. Agranat, V., Gurevich, Y., Lopez, A.M., Modeling of Turbulent Fluid Flows in Bent Pipes for Non-invasive Flow Measurement Application. Conference on CFD-97, Canada.

45. Lysak, P. D., Jenkins, D. M., Capone, D. E., and Brown, W. L., Analytical Model of an Ultrasonic Cross-Correlation Flow Meter, Part I: Stochastic Modeling of Turbulence, The Journal of Flow Measurement and Instrumentation 19(1): 1-7 (2008).

46. Lysak, P.D., Jenkins, D.M., Capone, D.E., Brown, W.L., Analytical model of an ultrasonic cross-correlation flow meter, part 2, Flow Measurement and instrumentation 19, 2008, pp. 41-46

47. Coppens, D., Gurevich, Y., Ton, V., and Zobin, D., Investigation Into Sensitivity Of Darlington Boiler 2 Feedwater Flow Calibration Factor To Boiler Level Control Valve Configuration 30th Annual Conference of the Canadian Nuclear Society, 2009 May 31 - June 3, TELUS Convention Centre, Calgary, Alberta

48. Peters, R., Blischke, F., and Meyr, H., Transit Time Estimation in Turbulent Flows, IEEE Transactions on Acoustics, Speech, and Signal Processing. Vol. 36, No 1, January 1988

49. Hans, V., Poppen, V., Flow Measurement with Cross-Correlated Ultrasonic Signals, Proceedings of FLOMEKO 96, pp 729-732, Beijing, China, 1996

50. Lau, P., Calculation of flow rate from differential pressure according to standards, Flow measurements in Nuclear Power Plants, Technical Workshop, Japan, May 20-23, 2008

51. Kolmogorov, A. N. 1941 The local structure of turbulence in incompressible viscous fluid for very large Reynolds numbers. Dokl. Akad. Nauk. SSSR 30, 299–303.

52. Davidson, P.A., Turbulence, an Introduction for Scientists and Engineers, Oxford Press, 2004.

53. Frisch, U. 1995 Turbulence. Cambridge University Press, Cambridge, UK

54. Bennett, A., Lagrangian Fluid Dynamics. Series: Cambridge Monographs on Mechanics, 2006

55. Lighthill, J. The fourth annual fairley lecture: The propagation of sound through moving fluids. Journal of Sound and Vibration, 24 (4) pp. 471- 492, 1972

56. Lumley, J. L. 1965 Interpretation of time spectra measured in high-intensity shear flows. Phys.Fluids 8, 1056–62.

57. Taylor, G. I. 1938 The spectrum of turbulence. Proc. R. Soc. Lond. A 164, 476–90.

58. Pope, S.B., Ten Questions Concerning the Large-Eddy Simulation of Turbulent Flows, Workshop on: LES & SGS Modeling For Turbulent Mixing and Reactive Flows, Caltech December 8-9, 2003

59. Goldstein, S., Modern Developments in Fluid Dynamics, Dover, 1965

60. Monin, A.S., Yaglom, A.M., Statistical Fluid Mechanics dover publication , inc., mineola, new York, 2007

61. Pope, S.B., Turbulent Flows, Cambridge University Press, 2005

62. Hwang, K.S., Cui, G.X., Zhang, Z.S., Feng, B.C., Quantitative visualization of the near-wall structures in a turbulent pipe flow by image correlation velocimetry. Experiments in Fluids, Volume 32, Number 4, April 2004, Pages 447-452

63. Naguib, A.M., Wark, C.E., An Investigation of Wall-Layer Dynamics Using a Combined Temporal Filtering and Correlation Technique. Journal of Fluid Dynamics, Vol. 243, pp. 541-560, 1992.

64. Laundr, B.E., Spalding, D.B., Mathematical Models of Turbulence. London: Academic Press, 1972

65. Landau, L.D., Lifshitz, E.M., Fluid Mechanics, Volume 6 of Course of Theoretical Physics, Translated from Russian, Pergamon Press, London-Paris-Frankfurt, 1959, Addison-Wesley Publishing Company, Inc., Reading, Massachusetts.

66. Holm, D.D., and Titi, E.S., Computational Models of Turbulence: The LANS–a Model and the Role of Global Analysis, SIAM News, Volume 38, Number 7, September 2005.

67. Barenblatt, G.I., Transfer of a Passive Additive in a Turbulent Boundary Layer at Very Large Reynolds Numbers, Proceedings of US National Academy of Science, 100, No 4, pp. 1481-1483, 2003.

68. Hanus, D., Anderle, P., Using of the Low Turbulence Wind Tunnel For Investigation of Three-Dimensional Unsteady Flow in Curved Tubes. ICAS 2002 Congress (International Council of the Aeronautical Sciences) 8-13 September, 2002, Toronto, Canada.

69. Barenblatt, G.I. Scaling. Cambridge University Press, Cambridge, xvi+171 pp

70. Anderson, D.A., Tannehill, J.C., Pletcher, R.H., Computational Fluid Mechanics and Heat Transfer, Hemisphere Publishing Corporation, Washington, New York, London, 1984.

71. Grinstein, F.F., Margolin, L.G., Rider, W.J., Implicit Large Eddy Simulation Computing Turbulent Fluid Dynamics, F., Los Alamos National Laboratory, Cambridge University Press 2008

72. John, V., Saarbrücken, On Large Eddy Simulation and Variational Multiscale Methods in the Numerical Simulation Of Turbulent Incompressible Flows, Application of Mathematics, No 4, 321-353, 51(2006)

73. Yang, Z., Abdalla, I.E., (2008) On coherent structures in a separated/reattached flow, WSEAS Transactions on Fluid Mechanics, 3, (2), pp 143-153

74. Abdalla, I., and Yang, Z., (2005) Effects of free-stream turbulence on large-scale coherent structures of separated boundary layer transition. Int Journal for Numerical Methods in Fluids, 49, pp. 331-348.

75. Abdalla, I., and Yang, Z., (2004) Numerical study of the instability mechanism in transitional separating-reattaching flow. International Journal of Heat and Fluid Flow, 25 (4), pp. 593-605.

76. Abdalla, I.E., and Yang, Z., Numerical Study of a Separated–Reattached Flow on a Blunt Plate AIAA JOURNAL Vol. 43, No. 12, December 2005

77. Abdalla, I.E., Cook, M.J., Rees, S.J., Yang, Z., Large-eddy simulation of buoyancy-driven natural ventilation in an enclosure with a point heat source, International Journal of Computational Fluid Dynamics, 21:5, 231 – 245

78. McLaren, K., Tullis, S., Ziada, S., CFD simulations of dynamic thrust and radial forces on a vertical axis wind turbine blade, 15th Ann. Conference of the CFD Society of Canada

79. Shahbazian, N., Tullis, S., Direct Numerical Simulation of Dilatation, Flame Strain and Curvature in Turbulent Premixed Flames, Proceedings of Combustion Institute – Canadian Section Spring Technical Meeting University of Toronto, Ontario May 12-14, 2008

80. Moser, R., Kim, J., and Mansour, N.N., Direct numerical simulation of turbulent channel flow up to Re = 590, Phys. Fluids 11, 943 (1999)

81. Sierra-Espinosa, F.Z., Bates, C.J., O'Doherty, T., Turbulent Flow in 900 pipe junction Part 1: Decay of turbulence fluctuation upstream the flow bifurcation, Computer & Fluids 29 (2), (2000) 197-213.

82. Sierra-Espinosa, F.Z., Bates, C.J., O'Doherty, T., Turbulent Flow in 900 pipe junction Part 2: Reverse flow at the branch exit. Computer & Fluids 29, (2000), 215-233.

83. Nicolleau, F.C.G.A., Nowakowski, A.F., and Michelitsch, T.M., Synthetic turbulence prediction in non-Kolmogorov turbulence 13th European Turbulence Conference (ETC13) IOP Publishing Journal of Physics: Conference Series 318 (2011) 042009

84. Tabor, G.R., Baba-Ahmadi, M.H., Inlet conditions for large eddy simulation: A review Computers & Fluids 39 (2010) 553–567

85. Kolhe, P.S., Agrawal, A.K., Investigation of the Cross-beam Correlation Algorithm to Reconstruct Local Field Statistics from Line-of-sight Measurements in Turbulent Flows, Flow Turbulence Combustion (2010) 84:617–638

86. Yamada, N., Lindberg, G., Tracer Measurement Technique and its Application to on-site Feed Water Calibration and Performance Analysis of Nuclear Power Plants, AIST/SP Workshop on Flow Measurements in Nuclear Power Plants, May 2008, Tokyo, Japan

87. Zhou, Q., Li, C.-M., Lu, Z.-M., and Liu, Y.-L., Experimental investigation of longitudinal space–time correlations of the velocity field in turbulent Rayleigh–Bénard convection, Journal of Fluid Mechanics / Volume 683 / September 2011, pp 94-111

88. He, X.-Z., He, G.-W. & Tong, P. 2010 Small-scale turbulent fluctuations beyond Taylor's frozen-flow hypothesis. Phys. Rev. E 81, 065303(R).

89. Jachens, A., Schumachder, J., Eckhardt, B., Knobloch, K. & Fernholz, H. H. 2006, Asymmetry of temporal cross-correlations in turbulent shear flows. J. Fluid Mech. 547, 55–64.

90. Pinton, J.-F. & Labbe, R. Correction of the Taylor hypothesis in swirling flows. J. Phys.II (France) 4, 1461–68. 1994

91. Favier, B., Godeferd, F.S., and Cambon, C., On space and time correlations of isotropic and rotating turbulence , Laboratoire de Mécanique des Fluides et d'Acoustique, UMR 5509, École Centrale de Lyon, CNRS, UCBL, INSA, Université de Lyon, F-69134 Ecully © 2010 American Institute of Physics

92. He, G.-W., and Zhang, J.-B., Elliptic model for space-time correlations in turbulent shear flows, PHYSICAL REVIEW E 73, 055303 May 2006

93. Zhao, X., and He, G.-W., Space-time correlations of fluctuating velocities in turbulent shear flows, PHYSICAL REVIEW E 79, 046316 2009

94. Burghelea, T., Segre, E., Steinberg, V., Validity of the Taylor hypothesis in a random spatially smooth flow. Phys. Fluids, 17, p. 103101, 2005.

95. Phillips, W.R.C., Eulerian space–time correlations in turbulent shear flows Phys. Fluids 12, 2056 (2000)

96. Kim, J., and Hussain, F., Propagation velocity of perturbations in turbulent channel flow, Phys. Fluids A 5, 695 (1993)

97. Phillips, W.R.C., The wall region of a turbulent boundary layer, Phys. Fluids 30, 2354 (1987)

98. Phillips, W.R.C., and Ratnanather, J.T., The outer region of a turbulent boundary layer, Phys. Fluids 2, 427 (1990)

99. Purtell, L.P., Klebanoff, P.S., and Buckley, F.T., Turbulent boundary layer at low Reynolds number, Phys. Fluids 24, 802 (1981)

100. Sedov, L.I., A Course in Continuum Mechanics, Pergmon Press, 1972

101. Laufer, J., The Structure Of Turbulence In Fully Developed Pipe Flow, NACA, Technical Note 2954, Washington, June 1953

102. Schlichting, H., Boundary Layer Theory, McGraw Hill, New York, 1979, 7th edn.

103. Gurevich, A., Abdalla, I., and Lopez, A., Theoretical Basis of Non-Intrusive Ultrasonic Cross Correlation Flow Measurement Technology, Proceedings of the 14th International Topical Meeting on Nuclear Reactor Thermalhydraulics, 2011

104. Gurevich, A., Development of a Mathematical Model of the Non Intrusive Ultrasonic Cross Correlation Flow Meter, Proceedings of the 35th Annual CNS-CNA Student Conference, 2011

105. Gurevich, A., and Lopez, A., Application and Theoretical Basis of Ultrasonic Cross Correlation Flow Measurement Technology, Canadian Nuclear Society Seminar at McMaster University, Institute for Energy Studies, 2010

106. Gurevich, A., Selvaratnarajah, S., and Abdalla, I., Theoretical and Experimental Analysis of Ultrasonic Cross Correlation Flow Measurement Technology, Proceedings of the 34th Annual CNS-CNA Student Conference, 2010